



**UNIVERSIDAD DE INVESTIGACIÓN DE
TECNOLOGÍA EXPERIMENTAL YACHAY**

Escuela de Ciencias Físicas y Nanotecnología

**TÍTULO: Computational studies of novel UIO-66-based MOF,
stability, electronic structure and defects**

Trabajo de integración curricular presentado como requisito para la
obtención
del título de Física

Autor:

Nicole Paulette Guerrero Cabrera

Tutor:

PhD. Henry Pinto

Urcuquí, octubre 2023

AUTORÍA

Yo **Guerrero Cabrera Nicole Paulette**, con cédula de identidad 0707067039, declaro que las ideas, juicios, valoraciones, interpretaciones, consultas bibliográficas, definiciones y conceptualizaciones expuestas en el presente trabajo; así como los procedimientos y herramientas utilizadas en la investigación, son de absoluta responsabilidad de el/la autor (a) del trabajo de integración curricular. Así mismo, me acojo a los reglamentos internos de la Universidad de Investigación de Tecnología Experimental Yachay.

Urququí, octubre 2023

Nicole Paulette Guerrero Cabrera
CI. 0707067039

AUTORIZACIÓN DE PUBLICACIÓN

Yo **Guerrero Cabrera Nicole Paulette**, con cédula de identidad 0707067039, cedo a la Universidad de Investigación de Tecnología Experimental Yachay, los derechos de publicación de la presente obra, sin que deba haber reconocimiento económico por este concepto. Declaro además que el texto del presente trabajo de titulación no podrá ser cedido a ninguna empresa editorial para su publicación u otros fines, sin contar previamente con la autorización escrita de la Universidad.

Asimismo, autorizo a la Universidad que realice la digitalización y publicación de este trabajo de integración curricular en el repositorio virtual, de conformidad con lo dispuesto en el Art. 144 de la Ley Orgánica de Educación Superior.

Urququí, octubre 2023

Nicole Paulette Guerrero Cabrera
CI. 0707067039

Dedication

To my dad, who always believed in me and my abilities.

Acknowledgements

I want to thank my family, especially my beloved mother, Miriam, for her unwavering support, sacrifice, and boundless love. To my sisters, Maytee, Michelle, and Helen, who have been there for me and never let me give up, providing strength and constant encouragement. I am grateful my friends, Milene, Kevin, Angie and Jordan, for their companionship, advice, and shared moments during our studies, friendship adds color to life.

I extend my appreciation to Henry, who introduced me to this world by letting me become a Compnano member, mentored me throughout this work, and became a friend along the way. I am equally thankful to all the professors who have been part of this journey and to my university, Yachay Tech, for providing me with the academic preparation I need for the future.

In closing, I want to convey my appreciation to the Task Supercomputer center in Gdansk for granting access to their supercomputer facilities.

Resumen

En busca de soluciones a los urgentes desafíos medioambientales, especialmente aquellos relacionados con contaminantes nocivos y gases de efecto invernadero, se han explorado diversos materiales por su potencial en aplicaciones fotocatalíticas. En este ámbito, los Marcos Metal-Orgánicos (MOFs) han captado considerable atención en la última década debido a su porosidad inherente y sus estructuras adaptables. UiO-66 ha surgido como un candidato sobresaliente gracias a su síntesis, estabilidad y propiedades en numerosas aplicaciones.

Esta investigación se centra en la exploración computacional del MOF UiO-66, investigando la influencia de los metales Ce y Ti en el nodo y la introducción de defectos en el enlace orgánico. El objetivo es mejorar su eficacia en la división del agua y la reducción del CO₂. Para lograrlo, realizamos cálculos de teoría de densidad *ab initio* utilizando varios funcionales, incluyendo PBESol, r²SCAN, r²SCAN+rVV10 y HSE06. Nuestros hallazgos revelan que la estructura electrónica derivada de r²SCAN+rVV10/HSE06 se ajusta estrechamente a los datos experimentales informados para el MOF Ce-UiO-66. También analizamos propiedades como el volumen, el módulo de compresibilidad y la banda de energías prohibidas, lo que indica el tamaño, la flexibilidad mecánica y las diferencias de energía entre las bandas de valencia y conducción. La combinación de los elementos Ce y Ti dentro de un nodo da como resultado tres estructuras distintas, cada una con una simetría única pero propiedades similares, lo que se refleja en su densidad de estados parciales (PDOS) con una banda prohibida y una función de trabajo reducidas, que disminuyen aún más después de introducir defectos. Al alinear los niveles de energía con respecto al potencial del vacío, hemos identificado a Ce-UiO-66-NH₂ como un prometedor fotocatalizador para la división del agua, principalmente debido a su pequeña brecha de banda, que requiere menos energía para la transferencia de carga. Investigaciones futuras se centrarán en la funcionalización de los enlaces orgánicos con yodo y bromo, así como en la exploración de variaciones en las proporciones de metales dentro del nodo para descubrir nuevas oportunidades para mejorar las propiedades fotocatalíticas del MOF UiO-66.

Palabras claves: fotocatalisis, teoría del funcional de densidad, vasp, funcionalizacion del ligando, función de trabajo.

Abstract

In pursuit of solutions to pressing environmental challenges, particularly those related to harmful pollutants and greenhouses, various materials have been explored for their potential in photocatalytic applications. Within this realm, Metal-Organic Frameworks (MOFs) have captured considerable attention over the last decade due to their inherent porosity and adaptable structures. UiO-66 has emerged as an outstanding candidate due to its synthesis, stability, and properties in numerous applications.

This research is centered on the computational exploration of UiO-MOF-66, investigating the influence of Ce and Ti metals within the node and the introduction of defects in the organic linker. The goal is enhancing its efficacy in water splitting and reducing CO₂. To achieve this, we conducted *ab initio* density functional theory calculations employing various functionals, including PBESol, r²SCAN, r²SCAN+rVV10 and HSE06. Our findings reveal that the electronic structure derived from r²SCAN+rVV10/HSE06 closely aligns with reported experimental data for Ce-UiO-66 MOF. We also analyzed properties such as volume, compressibility modulus, and band gap, indicating the size, mechanical flexibility, and energy differences between the valence and conduction bands. The combination of Ce and Ti elements within a node results in three distinct structures, each with unique symmetry but similar properties, which shows in their PDOS a reduced bandgap and work function, which further decreases after introducing defects. By aligning energy levels with respect to the vacuum potential, we have identified Ce-UiO-66-NH₂ as a promising photocatalyst for water splitting, primarily due to its small bandgap, which requires less energy for charge transfer. Future research will focus on functionalizing the organic linkers with iodine and bromine and investigating variations in the metal proportions within the node to uncover new opportunities for enhancing the photocatalytic properties of the UiO-66 MOF.

Keywords: photocatalysis, density functional theory, vasp, linker functionalization, work function.

Contents

List of Figures	xvi
List of Tables	xx
List of Papers	xxii
1 Introduction	1
1.1 Problem Statement	2
1.2 General and Specific Objectives	3
2 Theoretical Background	5
2.1 The Schrödinger Equation	5
2.1.1 Born-Oppenheimer Approximation	7
2.2 Density Functional Theory	7
2.2.1 Hohenberg-Kohn Theorem	8
2.2.2 Kohn-Sham Theory	8
2.2.3 Self-consistent Calculations	10
2.2.4 Functionals	10
2.3 Vienna <i>ab initio</i> Simulation Package	13
2.3.1 Periodicity, Plane Waves and k-points	13
2.3.2 Cut-off Energy	14
2.3.3 Pseudopotentials	15
2.4 Density of States	15
2.5 Photocatalysis in MOFs	17
2.5.1 Ionization potential	17
3 Methodology	19
3.1 Building the Structures	19
3.1.1 Introducing Defects	21

3.2	Computational Parameters	22
3.2.1	Cutoff Energy (E_{cut})	22
3.2.2	K-points Selection	22
3.2.3	Birch-Murnaghan Equation of States	22
3.3	VASP Implementation	25
3.4	Determining the Vacuum Potential	27
4	Results & Discussion	29
4.1	Functionals	29
4.2	Node Modifications	30
4.2.1	Ce-UiO-66	30
4.2.2	Ti-UiO-66	32
4.2.3	Ti ₃ Ce ₃ -UiO-66	37
4.3	Defects	39
4.3.1	Electrostatic and vacuum potential	43
4.4	Photocatalysis in Metal-Organic Frameworks	44
5	Conclusions & Outlook	51
A	Initial Inputs	53
B	Detailed Orbital-resolved Partial Density of States	57
C	Detailed Partial Density of States	67
	Bibliography	73

List of Figures

2.1	Adapted schematic flowchart, based on Giustino ¹ , that describes the process for achieving self-consistent solutions. This process begins with the calculation of the nuclear potential, followed by an initial guess for the electron density based on isolated atoms arranged in the material's positions, which allows us to determine V_H and V_{xc} , and consequently, V_{tot} . The numerical solution provides new wavefunctions ϕ_i for estimating the electron density. This iterative process continues until the new density estimated $n_n(r)$ matches the initial one $n_i(r)$ at a desired tolerance.	11
2.2	Electronic density of states with respect to the Fermi energy (E_f) of our calculated Ce-UiO-66 metal-organic framework presented in Section 4 with a clear differentiation of valence and conduction band and the presence of a band gap that separates both bands for this particular case.	16
3.1	Building Metal-Organic Frameworks a) MOF's node constructed with cerium metal ions b) 1,4-benzene-dicarboxylate (BDC) linker c) Ce-UiO-66 resulting structure.	20
3.2	Collections of the nodes or Secondary Building Units obtained with a) Titanium metal and mixed metals ions differentiated by their symmetry b) Ti_3Ce_3 (Sym1) c) Ti_3Ce_3 (Sym8) d) Ti_3Ce_3 (Sym160).	20
3.3	Functionalizing the linker with an amine group: a) X denotes the amine's position in forming the 2-aminobenzene-1,4-dicarboxylate ligand. b) Depicts the primitive cell of the topological defect at single linker functionalization (Ce-UiO-66-NH ₂), while c) corresponds to the unit cell of Sym8 after linker functionalization, resulting in the Sym8-UiO-66-(NH ₂)	21
3.4	Cutoff energy of Ce-UiO-66 MOF	23
3.5	a) Selection of the plane wave cutoff energy b) Considering a range of 1 meV/atom, the convergence starts with $E_{cut} = 950$ eV for the Ti-system.	24
3.6	For K-points selection, the convergence in point separation length of Ce-UiO-66 is achieved within an energy range of 1 meV/atom, and this convergence begins at $k = 1 \times 1 \times 1$	26
3.7	The Birch-Murnaghan equation of state (represented by the solid blue line) is derived from fits to data obtained with r2SCAN+rVV10 functional (represented as red dots) for the metal-organic framework (MOF) of titanium. This analysis provides values for volume $V = 2054.99 \text{ \AA}^3$ and bulk modulus $B_0 = 0.36 \text{ GPa}$	26
3.8	A periodic representation of the Ce-UiO-66 structure with its electrostatic potential used to determine the vacuum potential	27

4.1	Computed Partial density of states corresponding to the Ce-UiO-66 system with the functionals: a)PBEsol, b)r2SCAN, c)r ² SCAN+rVV10, and d)r ² SCAN+rVV10/HSE06, with an energy difference between valence and conduction band of 1.60 eV, 1.73 eV, 1.77 eV, and 2.78 eV, respectively.	31
4.2	The unit cell of Ce-UiO-66 after relaxation using r ² SCAN+rVV10.	33
4.3	Partial Density of States (PDOS) calculated using the r ² SCAN+rVV10/HSE06 functional for the Ce-UiO-66 structure. The highest occupied states predominantly originate from the atoms in the linker. In contrast, the lowest unoccupied states are primarily associated with the metal ions, resulting in a calculated bandgap of $E_g = 2.78$ eV.	33
4.4	a) A 2D slice of the electrostatic potential of Ce-UiO-66 in the (1 0 -1) plane where the pore with the highest electrostatic potential value was located a quarter of the lattice vector, indicated with a white circle. b) A periodic representation of the structure along with its corresponding electrostatic potential.	34
4.5	Partial Density of States (PDOS) for a) Ce-UiO-66 and b) Ti-UiO-66 configurations calculated using r ² SCAN+rVV10/HSE06 functionals. The band gap (E_g) and band edge positions are aligned with respect to the vacuum level and are detailed in Table 4.2. In this graph, it is evident that altering the metal node results in changes in the band structure. Notably, in the case of Ti compared to Ce, the conduction band is shifted by approximately 1 meV, with this shift primarily attributed to the Ti <i>d</i> orbital contribution.	35
4.6	The unit cell of Ti-UiO-66 after relaxation using r ² SCAN+rVV10.	36
4.7	Partial Density of States (PDOS) calculated using the r ² SCAN+rVV10/HSE06 functional for the Ti-UiO-66 structure. The highest occupied states from the valence band predominantly originate from the atoms in the linker, whereas the lowest unoccupied states in the conduction band are primarily associated with the metal ions, resulting in a calculated bandgap of $E_g = 3.73$ eV	36
4.8	a) A 2D slice of the electrostatic potential of Ti-UiO-66 in the (1 0 -1) plane where the pore with the highest electrostatic potential value was located a quarter of the lattice vector, indicated with a white circle. b) A periodic representation of the structure along with its corresponding electrostatic potential.	38
4.9	The unit cell of Ti ₃ Ce ₃ -UiO-66, with a mixed-metal node, was subjected to relaxation using the r ² SCAN+rVV10 functional. Three distinct configurations were obtained, each characterized by a different symmetry: a) Sym1 b) Sym160 c) Sym8	40
4.10	Partial Density of States (PDOS) was computed using the r ² SCAN+rVV10/HSE06 functional for three distinct structural variants of Ti ₃ Ce ₃ -UiO-66: a) Sym160, b) Sym8 and c) Sym1. In the PDOS plots, the most substantial contributions to the valence band originate from C, O, and H atoms. In contrast, the conduction band is predominantly composed of contributions from the metal ions. The Fermi level was aligned to 0 eV, and the bandgap values were determined to be $E_g = 2.79$ eV, $E_g = 2.79$ eV, and $E_g = 2.61$ eV for Sym160, Sym8, and Sym1, respectively.	41

4.11	Partial Density of States (PDOS) for a) Sym160, b) Sym8, and c) Sym1 configurations were calculated using r^2 SCAN+rVV10/HSE06 functionals. In all cases, the primary contributions in the valence band originate from the s , p , and d orbitals of H, C, and O in the linker, while in the conduction band, contributions come from the f and d orbitals of Ce and Ti. Band gap (E_g) and band edge positions are referenced to the vacuum level and detailed in Table 4.3.	42
4.12	Unit cells of a) Ce-UiO-66-X, b) Sym160-X, c) Sym8-X, and d) Sym1-X structures with amine functionalization after relaxation using the r^2 SCAN+rVV10 functional (X in their names refers to the amine group NH_2).	45
4.13	(PDOS) computed using the r^2 SCAN+rVV10/HSE06 functional for a) Ce-UiO-66-X, b) Sym160-X, c) Sym8-X and c) Sym1-X. The valence band is shifted compared to the structures without defects due to nitrogen; the atoms with the greatest contribution correspond to C, O, and H, while in the conduction band, there is a greater contribution from metal ions. The Fermi level was aligned to 0 eV, and the bandgap values are listed in Table 4.4 (X in their names refers to the amine group NH_2).	47
4.14	PDOS for a) Ce-UiO-66-X b) Sym160-X, b) Sym1-X, and c) Sym8-X configurations calculated using r^2 SCAN+rVV10/HSE06 functionals, where X in their names refers to an amine group NH_2 . In all cases, the highest occupied crystal orbital corresponds to the d orbital of N, while the lowest unoccupied orbital corresponds to the f orbital of cerium. The band gap (E_g) (detailed in Table 4.4) and band edge positions are aligned with respect to the vacuum level.	48
4.15	a) Absolute band edge positions for all computed structures and experimental (Zr/Ti/Ce)UiO-66 reported by Melillo et al. ² . The X in the names of MOFs refers to an amine group NH_2 . Upon initial inspection, it is evident that both computed and experimental structures facilitate H_2O/O_2 reactions. However, only the computed Ti MOF are suitable for H^+ / H_2 reactions.	49
4.16	a) Absolute positions of the band edges for all computed structures and an experimental (Zr/Ti/Ce)UiO-66 reported structure by Melillo et al. ² are presented. The X in the names of MOFs refers to an amine and dashed lines represent energy levels corresponding to redox potentials for various CO_2 reduction reactions. b) A zoomed-in view of the energy range relevant to CO_2 reduction reactions where is shown that (Zr/Ti/Ce)UiO-66 experimental structure that will allow CO_2/CH_4 reaction while the computed Ti-structure allowed different CO_2 reactions.	50
B.1	Detailed orbital resolved PDOS for Ce-UiO-66 structure.	58
B.2	Detailed orbital resolved PDOS for Ti-UiO-66 structure.	59
B.3	Detailed orbital resolved PDOS for Ti_3Ce_3 (Sym1)-UiO-66	60
B.4	Detailed orbital resolved PDOS for Ti_3Ce_3 (Sym160)-UiO-66	61
B.5	Detailed orbital resolved PDOS for Ti_3Ce_3 (Sym8)-UiO-66	62
B.6	Detailed orbital resolved PDOS for Ce-UiO-66- NH_2 structure.	63
B.7	Detailed orbital resolved PDOS for Ti_3Ce_3 (Sym1)-UiO-66- NH_2	64
B.8	Detailed orbital resolved PDOS for Ti_3Ce_3 (Sym8)-UiO-66- NH_2	65
B.9	Detailed orbital resolved PDOS for Ti_3Ce_3 (Sym160)-UiO-66- NH_2	66

C.1	Detailed PDOS for Ce-UiO-66	67
C.2	Detailed PDOS for Ti-UiO-66	68
C.3	Detailed PDOS for $\text{Ti}_3\text{Ce}_3(\text{Sym}160)\text{-UiO-66}$	68
C.4	Detailed PDOS for $\text{Ti}_3\text{Ce}_3(\text{Sym}8)\text{-UiO-66}$	69
C.5	Detailed PDOS for $\text{Ti}_3\text{Ce}_3(\text{Sym}1)\text{-UiO-66}$	69
C.6	Detailed PDOS for Ce-UiO-66-NH ₂	70
C.7	Detailed PDOS for $\text{Ti}_3\text{Ce}_3(\text{Sym}160)\text{-UiO-66-NH}_2$	70
C.8	Detailed PDOS for $\text{Ti}_3\text{Ce}_3(\text{Sym}8)\text{-UiO-66-NH}_2$	71
C.9	Detailed PDOS for $\text{Ti}_3\text{Ce}_3(\text{Sym}1)\text{-UiO-66-NH}_2$	71

List of Tables

2.1	Jacob’s ladder of density Functional approximation, adapted from Perdew and Schmidt ³ . Each rung outlines the computational requirements and resources for each functional.	10
4.1	Crystallographic and electronic structure data computed for Ce-UiO-66 with PBESol, r ² SCAN, r ² SCAN+rVV10 and r ² SCAN+rVV10/HSE06 functionals and <i>Expt</i> experimental values reported by Lammert et al. ⁴ . Here <i>a</i> , <i>b</i> and <i>c</i> are the lattice parameters, α , β and γ the angles, V_{opt} is the optimal volume, B_0 the bulk modulus, E_{cut} is the cutoff energy required for calculations and E_g represents the bandgap. In the case of r ² SCAN+rVV10, the value of E_g between brackets is the computed electronic structure using HSE06 with the optimal structure yielded by r ² SCAN+rVV10.	30
4.2	Crystallographic data were computed using the r ² SCAN+rVV10 functional for the Ti- and Ce-UiO-66 structures. In these calculations, <i>a</i> , <i>b</i> , and <i>c</i> represent the lattice parameters, while α , β , and γ denote the lattice angles. The optimal volume is denoted as V_{opt} , B_0 represents the bulk modulus, E_{tot} the total energy and N_{at} the total number of atoms. Additionally, E_{cut} signifies the cutoff energy required for the calculations. Electronic properties, such as the bandgap E_g and work function Φ , were determined using the r ² SCAN+rVV10/HSE06 method.	37
4.3	Crystallographic data were computed using the r ² SCAN+rVV10 functional for the Ti ₃ Ce ₃ -UiO-66 structures. In these calculations, <i>a</i> , <i>b</i> , and <i>c</i> represent the lattice parameters, while α , β , and γ denote the lattice angles. The optimal volume is denoted as V_{opt} , B_0 represents the bulk modulus, the relative energy ΔE_{tot} with respect to the stable configuration (Sym8) and N_{at} the total number of atoms. Electronic properties, such as the bandgap E_g and work function Φ , were determined using the r ² SCAN+rVV10/HSE06 functional.	43

4.4	Crystallographic data were computed using the r^2 SCAN+rVV10 functional for the Ti_3Ce_3 -UiO-66- X structures, where X denotes an amine group (NH_2). In these calculations, a , b , and c represent the lattice parameters, while α , β , and γ denote the lattice angles, E_{cut} the total energy and N_{at} the number of atoms. Electronic properties, such as the bandgap E_g and work function Φ , were determined using the r^2 SCAN+rVV10/HSE06 functional.	44
.....		
4.5	Computed and reported free energy change per electron (ΔG) in electronvolts (eV) for selected reactions by Wu et al. ⁵ . Calculations were conducted under standard conditions of pH=7 and room temperature (298.15K).	46
.....		

Chapter 1

Introduction

Human development has been a continuous process marked by significant changes throughout history, motivated by the primary objective of satisfying essential needs. One of these transformations focused on the mechanization of production, which changed the economy and produced substantial technological advances. However, industrialization has brought with it the mismanagement of its waste, seriously impacting the air, water, and soil. A clear example is the presence of various dyes, fluoride anions, and heavy metals pollutants from textile, cosmetic, pharmaceutical, and paper industries, which have been discovered in water sources⁶. These pollutants alter and affect ecosystems, biodiversity, human well-being, and the quality of life in general.

In response, scientists have directed their efforts to find and propose solutions through a combination of computational and experimental studies of materials and their properties. The notable advances in materials science allow us to suggest a material supporting specific chemical reactions using solar energy as fuel, commonly known as photocatalysis. Furthermore, its selectivity can be achieved through confined spaces and surfaces. This has sparked increasing interest in porous materials, which provide reaction confinement and facilitate mass transfer from the outer to the inner regions of a solid particle⁷.

Porosity was a term defined and proved while studying inorganic zeolites. Over time, the growing need to integrate transition metal ions and organics compounds into their structure led to the introduction of Metal Organic Framework (MOF)⁸. MOFs are seen as networks formed by a single metal ion or a polynuclear metal cluster commonly known as Secondary Building Units (SBU) combined with an organic linker to build a crystalline structure⁹. They become popular mainly for features like porosity and high surface, but some of their properties are small density, tunable pore functionality, structural flexibility, and tunable functional groups¹⁰. Thus making those materials promising candidates for several applications, including not only gas storage but also small-molecule separations, liquid phase separation, heterogeneous catalysis, drug delivery, sensing, proton conductivity, magnetism and other applications^{11 12}.

Metal Organic Frameworks have been widely studied for catalysis due to Lewis acid or coordinatively unsaturated sites that can be generated around the metal center or by defects. More recently, their photocatalytic activity resulting from the intimate interaction between the organic linker and metal node has attracted attention for applications in

hydrogen generation and CO₂ reduction¹³. Efforts in their development would bring with it, in addition to pollutant removal, the generation of environmentally friendly clean fuels, carbon-containing fuel production, and the recycling of carbon dioxide from the environment.

Cerium is a desirable choice for our research due to its earth abundance, remarkable redox properties, and stable +IV oxidation state attributed to its *f* orbitals. This stability ensures that chemical reactions can occur within the resulting pores rather than just on their surface, thus enhancing the number of active sites within the material¹⁴. Cerium oxide is well-known for its application in the decomposition of NO_x and the oxidation of CO, owing to oxygen's mobility and storage capacity. The node within the Ce-UiO-66 structure can even be regarded as the smallest possible CeO₂ unit, with each metal atom exposed to the material's pores¹⁵. Similarly, TiO₂ has been extensively investigated and documented for its ability to enhance gas transport and material separation properties. In particular, the presence of a titanium atom within the structure leads to a reduction in pore size, which, when combined with the advantageous size-to-charge relationship exhibited by Ti⁴⁺ ions in polarized CO₂ molecules, results in a notable improvement in the adsorption capacity of the material¹⁶.

Computational analysis, a theoretical approach, presents one of the two general avenues for predicting material properties, the other being experimental exploration. The first is the most efficient in terms of cost and time, as well as being a complement to experimental investigations. In materials science, Density Functional Theory (DFT) offers a numerical approach to solving equations that describe the interactions between electrons and atomic nuclei. While this method may not achieve absolute precision due to the unknown nature of the functional describing exact density and energy, electronic structure calculations provide valuable quantitative insights into a system's electronic properties that may not be obtained through experimentation⁹.

1.1 Problem Statement

The growing global demand for sustainable energy production and the urgent need to combat environmental challenges, such as air and water pollution, have intensified research efforts in photocatalysis. Although conventional semiconductors have been promising photocatalysts, their application is limited by efficiency, stability, and/or selectivity¹³. Organometallic structures have gained significant attention due to their distinctive properties and intriguing metal-ligand interaction. Among these, UiO-66, initially synthesized at the University of Oslo, stands out. Comprising a zirconium cluster Zr₆O₄(OH)₄ connected to 1,4-benzene-dicarboxylate (BDC) linkers, it has garnered extensive research interest for its scalable laboratory synthesis, stability, and catalytic properties. Moreover, it is reported that modifying the metal within the node with elements, such as cerium, has shown excellent adsorption capacity and potential to effectively remove toxic contaminants¹⁷. As these materials' properties result from their node and ligand composition, exploring viable and stable configuration for specific applications has become a matter of great interest in the scientific community. Consequently, this study aims to identify configurations with photocatalytic potential through a computational electronic structure analysis.

1.2 General and Specific Objectives

The purpose of this study is to perform Density Functional Theory (DFT) calculations to explore the changes in the properties of a new system derived from Zr-UiO-66 that starts from the metallic modification of the $M_6O_4(OH)_4$ node with $M = Ce, Ti$. The functionalization of the 1,4-benzene-dicarboxylate (BDC) linker and the implementation of defects seek to enhance the search for a material capable of enhancing chemical reactions with solar energy. In pursuit of this objective, the following specific goals have been outlined:

- To describe the theoretical basis behind the density functional theory required for the development of this work.
- To compare various functionals and the importance of their choice to ensure accuracy in the results in contrast to the experimentally available data.
- To analyze the electronic structure of stable configurations.
- To align the energy with respect to the vacuum energy to find configurations that can be applied to specific reactions.
- To study changes resulting from functionalization of ligand and defects.
- To conclude with selecting a promising candidate for photocatalytic applications in light of the results obtained.

Chapter 2

Theoretical Background

This chapter delves into the theories on which our research is based. We begin with the many-body Schrödinger equation and explore how the approaches to solving form the basis of Density Functional Theory (DFT), along with the computational tools commonly used for modeling material properties.

2.1 The Schrödinger Equation

A material is a system composed of particles that define its properties, requiring an adequate and precise description. The modeling of materials is based on the development and use of mathematical models to describe and predict their properties and potential applications¹⁸. Quantum Mechanics is the most powerful model for this purpose, as it describes the behavior of matter and energy at atomic and subatomic levels by representing quantum states through evolving wavefunctions over time in an equation called Schrödinger Equation. Considering only stationary electronic states, this equation becomes a time-independent Schrödinger Equation:

$$(\hat{K} + \hat{V})\psi = E\psi, \quad (2.1)$$

where $\hat{K} + \hat{V} = \hat{H}$ is the Hamiltonian, $\hat{K} = \frac{(-i\hbar\nabla)^2}{2m_e}$ is the kinetic energy with \hbar being the reduced plank constant, m_e the electron mass and $\nabla = u_x \frac{\partial}{\partial x} + u_y \frac{\partial}{\partial y} + u_z \frac{\partial}{\partial z}$. \hat{V} is the potential energy and E is the energy eigenvalue described by the wavefunction ψ depending on the position r . The sum of the kinetic and potential energy gives the so-called Hamiltonian H of the system. This equation is valid for a single particle, yet a material is formed by many electrons(N) and nuclei(M) with coordinates r_1, r_2, \dots, r_N and R_1, R_2, \dots, R_M , respectively. Then, the wavefunction will depend on the position of each particle involved in the system:

$$\Psi = \Psi(r_1, r_2, \dots, r_N; R_1, R_2, \dots, R_M) \quad (2.2)$$

Therefore, eqn 2.1 will be rewritten as:

$$(K + V)\Psi = E_{tot}\Psi \quad (2.3)$$

Now with eigenvalue E_{tot} as the total energy of the system and the kinetic energy considering the N electrons and M nuclei:

$$K = - \sum_{i=1}^N \frac{\hbar^2}{2m_e} \nabla_i^2 - \sum_{I=1}^M \frac{\hbar^2}{2M_I} \nabla_I^2, \quad (2.4)$$

with $M_I, I = 1, 2, \dots$ as the masses of the I -nuclei and ∇^2 as the Laplace operator acting on the coordinate of each particle. Similarly, we have the potential energy present due to the charged particles involved in the system described by three possible Coulomb interactions:

- Repulsion between pair of electrons:

$$V_{e-e} = \frac{1}{2} \sum_{i \neq j} \frac{e^2}{4\pi\epsilon_0} \frac{1}{|r_i - r_j|} \quad (2.5)$$

- Repulsion between pair of nuclei:

$$V_{n-n} = \frac{1}{2} \sum_{I \neq J} \frac{e^2}{4\pi\epsilon_0} \frac{Z_I Z_J}{|R_I - R_J|} \quad (2.6)$$

- Attraction between electron and nuclei:

$$V_{e-n} = - \sum_{i,J} \frac{e^2}{4\pi\epsilon_0} \frac{Z_I}{|r_i - R_I|} \quad (2.7)$$

Where e is the charge of electron, ϵ_0 the permittivity of vacuum and Z_I denotes atomic numbers. All together replaced into eqn 2.3 ends with the many-body Schrödinger equation.

$$\left[- \sum_i^N \frac{\hbar^2}{2m_e} \nabla_i^2 - \sum_I^M \frac{\hbar^2}{2M_I} \nabla_I^2 + \frac{1}{2} \sum_{i \neq j} \frac{e^2}{4\pi\epsilon_0} \frac{1}{|r_i - r_j|} + \frac{1}{2} \sum_{I \neq J} \frac{e^2}{4\pi\epsilon_0} \frac{Z_I Z_J}{|R_I - R_J|} - \sum_{i,J} \frac{e^2}{4\pi\epsilon_0} \frac{Z_I}{|r_i - R_I|} \right] \Psi = E_{tot} \Psi, \quad (2.8)$$

with i, j and I, J being the sum indexes running from 1 to N and 1 to M respectively. This equation can be simplify by using atomic units¹⁸: $\hbar = 1.054572 \times 10^{-34} \text{ J} \cdot \text{s}$, $m_e = 9.109383 \times 10^{-31} \text{ Kg}$, $m_p = 1.672622 \times 10^{-27} \text{ kg}$, $e = 1.602176 \times 10^{-19} \text{ C}$, $\epsilon_0 = 8.854188 \times 10^{-12} \text{ F/m}$. In addition, considering the angular momentum in the ground state of hydrogen in Bohr model, we can write $\hbar = m_e v a_0$, where a_0 is the Bohr radius, and incorporating Hartrees, $E_{Ha} = \frac{e^2}{4\pi\epsilon_0 a_0} = m_e v^2$ we have:

$$\left[- \sum_i^N \frac{1}{2} E_{Ha} a_0^2 \nabla_i^2 - \sum_I^M \frac{1}{2} \frac{E_{Ha} a_0^2}{M_I/m_e} \nabla_I^2 + \frac{1}{2} \sum_{i \neq j} \frac{a_0 E_{Ha}}{|r_i - r_j|} + \frac{1}{2} \sum_{I \neq J} a_0 E_{Ha} \frac{Z_I Z_J}{|R_I - R_J|} - \sum_{i,J} a_0 E_{Ha} \frac{Z_I}{|r_i - R_I|} \right] \Psi = E_{tot} \Psi \quad (2.9)$$

Dividing this equation by E_{Ha} , using $e = 1$ and leaving it to Hartree atomic units, we obtain:

$$\left[-\sum_i^N \frac{1}{2} \nabla_i^2 - \sum_I^M \frac{\nabla_I^2}{2M_I} + \frac{1}{2} \sum_{i \neq j} \frac{1}{|r_i - r_j|} + \frac{1}{2} \sum_{I \neq J} \frac{Z_I Z_J}{|R_I - R_J|} - \sum_{i,J} \frac{Z_I}{|r_i - R_J|} \right] \Psi = E_{tot} \Psi \quad (2.10)$$

2.1.1 Born-Oppenheimer Approximation

Obtaining a direct solution to equation 2.10 is only feasible for hydrogen, making it challenging for other systems. Consequently, approximations are commonly employed. An important approach involves assuming nearly stationary nuclei while electrons are in motion, a reasonable assumption given their considerable mass difference. This approximation effectively divides the equation into two separate equations: one for electrons and another for the nuclei. As result, the total wavefunction Ψ is expressed as the product of the electron-only Ψ_R and nuclear-only χ wavefunction both dependent in the nuclear coordinates R_1, R_2, \dots, R_M . This separation of electron and nuclear dynamics is known as Born-Oppenheimer Approximation (BO) or adiabatic approximation¹⁸:

$$\Psi(\mathbf{r}_1, \dots, \mathbf{r}_N, \mathbf{R}_1, \dots, \mathbf{R}_M) = \Psi_R(\mathbf{r}_1, \dots, \mathbf{r}_N) \chi(\mathbf{R}_1, \dots, \mathbf{R}_M) \quad (2.11)$$

As the nuclei are immobile, the kinetic energy can be neglected, and the Coulomb potential becomes constant storage in the right-hand side $E = E_{tot} - \frac{1}{2} \sum_{i \neq j} \frac{Z_i Z_j}{|R_i - R_j|}$ and we have:

$$\left[-\sum_i^N \frac{1}{2} \nabla_i^2 + \sum_i V_n(\mathbf{r}_i) + \frac{1}{2} \sum_{i \neq j} \frac{1}{|r_i - r_j|} \right] \Psi_R = E_R \Psi_R \quad (2.12)$$

Here $V_n(r) = -\sum_I \frac{Z_I}{|r - R_I|}$. The terms inside brackets are the many-electron Hamiltonian. So now, replacing equation 2.11 and 2.12 into 2.10:

$$\left[-\sum_i^N \frac{1}{2} \nabla_i^2 + \frac{1}{2} \sum_{I \neq J} \frac{Z_I Z_J}{|R_I - R_J|} + E(R_1, \dots, R_M) \right] \chi = E_{tot} \chi, \quad (2.13)$$

where $E(\mathbf{R}_1, \dots, \mathbf{R}_M)$, the total electronic energy serves as an effective potential governing the behavior of the nuclei.

2.2 Density Functional Theory

Computational materials modeling relies on theoretical and computational techniques based in DFT, an *ab initio*, a quantum mechanics-based method for approximating material properties. Interactions between quantum particles in a system are described by the many-body Schrödinger equation 2.8, which, when solved, provides insight into a material's equilibrium properties. However, solving this equation is exceptionally challenging due to its exponentially growing complexity with system size¹⁸.

Practical approaches to the Schrödinger equation based on the theorems established by Hohenberg-Kohn have led to the development of the Kohn-Sham equations. These equations treat electrons as independent particles, simplifying the process without sacrificing precision. Consequently, the results are accurate and closely match the

experimental measurements with a small error percentage. This ability to directly compare theoretical predictions with experimental data represents a significant advantage of DFT in materials research.

2.2.1 Hohenberg-Kohn Theorem

Starting from their name, DFT focuses on the electronic density $n(r)$ of a molecule, solid, or quantum system. This electronic density describes how the electrons are distributed around the nuclei of a material and can be seen as the probability of finding an electron in a specific position. There are fundamental mathematics theorems behind DFT. One of them is the Hohenberg-Kohn (HK) theorem with the statement that the total energy E of a many-electron system is a function of the electron density $F[n]$ supported by three premises^{18,19}.

$$E = F[n] \quad (2.14)$$

1. Electron density in the system's ground state allows to determine only the external potential of the nuclei.
2. The many-electron wavefunction is simply determined by the external potential V_n .
3. The system's total energy is a function of the wavefunction.

Overall, it tells us that a one-to-one mapping exists between ground state wave function and ground state electron density²⁰. Therefore, the total energy of a system with interacting electrons can be mathematically described as their sum, including the external potential due to the interaction with the nuclei and surroundings.

$$E = \langle \Psi | \hat{H} | \Psi \rangle = \langle \Psi | \hat{T} + \hat{W} | \Psi \rangle + \int d\mathbf{r} V_n(\mathbf{r}) n(\mathbf{r}) \quad (2.15)$$

Being \hat{T} the kinetic and \hat{W} the Coulomb energy and 2.15 corresponding to the universal functional of the density for all electrons in the system¹.

Hohenberg and Kohn Variational Principle

A second theorem derived from Hohenberg and Kohn enables us to find a solution with the lowest energy, corresponding to the ground state, which represents the most stable configuration and fundamental behavior of the system. This theorem states that the electronic density that minimizes the functional energy is in fact, the authentic electronic density capable of providing a comprehensible solution to the Schrödinger equation²⁰. The function that minimizes the total energy, $E = F[n]$ is the ground state density, n_0 ¹⁹ known as Variational principle described:

$$\left. \frac{\delta F[n]}{\delta n} \right|_{n_0} = 0 \quad (2.16)$$

2.2.2 Kohn-Sham Theory

Although we understand that the total energy in the ground state is a functional of the electron density, the precise form of this functional remains unknown. In 1965, Kohn and Sham²¹ presented an approximation by recognizing

that one of the two terms in the equation 2.15 lacks explicit density dependence. As a result, their attention turned to describing the kinetic and Coulomb energy by considering independent electrons and adding an extra term. Given that $E = F[n]$, we have:

$$F[n] = \int d\mathbf{r} V_n n(\mathbf{r}) - \sum_i \int d\mathbf{r} \phi_i^*(\mathbf{r}) \frac{\nabla^2}{2} \phi_i(\mathbf{r}) + \frac{1}{2} \iint d\mathbf{r} d\mathbf{r}' \frac{n(\mathbf{r})n(\mathbf{r}')}{|\mathbf{r} - \mathbf{r}'|} + E_{xc}[n] \quad (2.17)$$

So, the first term corresponds to the external potential, followed by kinetic and Hartree energy. Until here, they all give the system's total energy in the independent electron approximation. The last term is called the exchange and correlation energy and clusters everything unknown.

Reducing the functional to $E_{xc}[n]$ allows us to focus on estimating the total energy of the fundamental state. The challenge now lies in accurately determining the electronic density. For that, we will employ Hohenberg-Kohn's variational principle of energy (eq 2.16), which states that the energy of the fundamental state corresponds to the function minimizing the total energy. Then, by deriving the functional, setting its derivative to zero, and ensuring orthonormality, we can obtain pertinent equations for the wave function $\phi_i(r)$ that enables us to characterize the density. This leads us to the following equation:

$$\left[-\frac{1}{2} \nabla^2 + V_n(\mathbf{r}) + V_H(\mathbf{r}) + V_{xc}(\mathbf{r}) \right] \phi_i(\mathbf{r}) = \varepsilon_i \phi_i(\mathbf{r}), \quad (2.18)$$

with $-\frac{\nabla^2}{2}$, V_n , V_H denoting kinetic energy, external nuclear potential coming from the interaction between an electron and a collection of atomic nuclei, the Hartree potential that describes the Coulombic repulsion between electrons, the overall electron density, and the *self-interaction contribution* which includes the Coulomb interaction of electrons with themselves that results in destabilized localized orbitals²⁰:

$$V_H(\mathbf{r}) = e^2 \int \frac{n(\mathbf{r}')}{|\mathbf{r} - \mathbf{r}'|} d^3 \mathbf{r}'. \quad (2.19)$$

and finally, the V_{xc} exchange and correlation potential accounts for both corrective and unphysical self-interaction contributions within the single-electron equation²⁰:

$$V_{xc}(\mathbf{r}) = \left. \frac{\delta E_{xc}[n]}{\delta n} \right|_{n(\mathbf{r})} \quad (2.20)$$

This unphysical interaction can be canceled if the exact functional were known. However, in its absence, approximations lead to a self-interaction error that does not completely cancel the self-interaction energy, resulting in destabilized localized orbitals, an issue than can be remedied by employing hybrid functionals with partial exact exchange to partially correct the self-interaction²⁰. The equations derived from eq 2.18 are known as the Kohn-Sham equations, forming the basis of density functional theory and serving as a potent tool for material property calculations. This directs attention towards approximating the functional E_{xc} to accurately approach the ground state energy and density, as shown below.

2.2.3 Self-consistent Calculations

The Kohn-Sham (KS) equations are used to calculate the total energy and density of electrons in their ground state. Achieving self-consistency in these equations requires that the solutions for the electronic states, ϕ_i , coincide throughout the iterative process. To do this, we initially calculate the nuclear potential by specifying the nuclear coordinates, then guess the electron density based on isolated atomic positions to determine an approximation for V_H and V_{xc} to solve for V_{tot} , which will give new wavefunctions used to better estimate electron density. The iterative process continues until it converges to a desired tolerance with respect to the initial assumption, which means self-consistency. In Fig.2.1 is presented an adapted schematic flow chart from Giustino¹ describing the process for self consistent solutions which begins with the calculations of the nuclear potential, a guessing of an initial electron density based on isolated atoms arranged in materials position to determine V_H and V_{xc} and therefore V_{tot} . In that way the numerical solution will give new wavefunction to estimate the density. An iterative process that ends when under a desired toleranced the new stimated density matches with the initial one.

2.2.4 Functionals

Following the establishment of the Kohn-Sham equations, extensive efforts were directed toward finding an exchange-correlation functional that best approximates the ground state energy and, therefore, the density of a many-body system. These efforts have led to the development of several approaches, which Perdew³ organized into a hierarchy known as Jacob's Ladder, where functionals are categorized based on their requirements and computational resources, as demonstrated in Table 2.1.

Table 2.1: Jacob's ladder of density Functional approximation, adapted from Perdew and Schmidt³. Each rung outlines the computational requirements and resources for each functional.

Chemical Accuracy	ingredients
Beyond DFT	
Hybrid	$n(r)$, $\nabla n(r)$, exact exchange
mGGA	$n(r)$, $\nabla n(r)$, $\nabla^2 n(r)$
GGA	$n(r)$, $\nabla n(r)$
LDA	$n(r)$
Hartree World (Earth)	

The initial step of this ladder involves the local density approximation (LDA). LDA was built assuming a uniform distribution of a homogeneous electron gas within the material, where nuclear potentials remain constant, and Coulomb repulsion among electrons is considered²². Then, the local exchange-correlation potential is described as the exchange potential for a spatially uniform electron gas with the same density as the local electron density²⁰. In the next level, the generalized gradient approximation (GGA) is found, which accounts for information about the local electron density and its gradient when computing energy values, resulting in more accurate descriptions²².

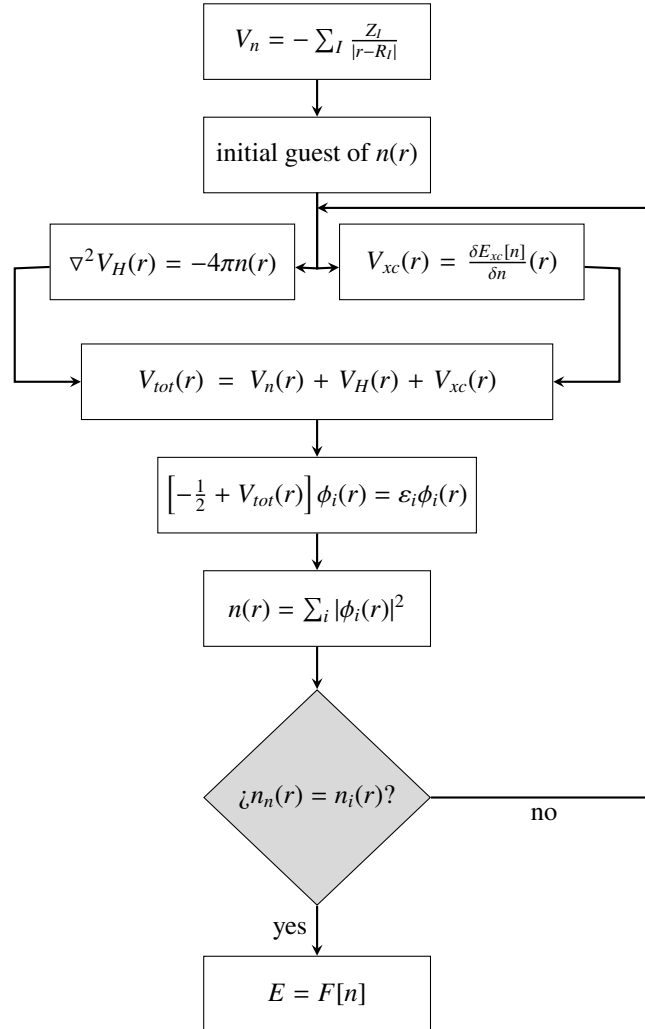


Figure 2.1: Adapted schematic flowchart, based on Giustino¹, that describes the process for achieving self-consistent solutions. This process begins with the calculation of the nuclear potential, followed by an initial guess for the electron density based on isolated atoms arranged in the material's positions, which allows us to determine V_H and V_{xc} , and consequently, V_{tot} . The numerical solution provides new wavefunctions ϕ_i for estimating the electron density. This iterative process continues until the new density estimated $n_n(r)$ matches the initial one $n_i(r)$ at a desired tolerance.

Some functionals that can be found in this category Perdew-Burke-Ernzerhof (PBE) and Perdew-Burke-Ernzerhof for solids (PBESol)²³.

Following that, the meta-Generalized Gradient Approximation (mGGA) functionals introduce the orbital kinetic energy density as an extra local property upon which E_{xc} depends. And then, the hybrid functionals incorporate a percentage of the exact Hartree-Fock exchange⁹. These hybrid functionals may also include a screened potential, as in the case of HSE06. In general, incorporating progressively more information about the real behavior of electrons provides more accurate results but has a higher computational cost. It is essential to emphasize that no functional can precisely calculate the ground state energy of a system, as they do not provide an exact solution to the Kohn-Sham equations.

PBESol

One of the most commonly used approximations to calculate the exchange-correlation energy is the PBESol²⁰. A GGA that, as seen before, relies on the density and its gradient at each point in space. However, PBE tends to underestimate equilibrium constants and associated properties such as bulk modulus, photon frequencies, etc. Perdew et al.²³ proposed a function correction for solids by introducing a modified function that recovers the gradient expansion for exchange over a wide range of density gradients to address this limitation. This modification leads to a significantly improved lattice constant when compared to PBE²⁴ as well as excellent surface exchange energies.

From Strongly Constrained and Appropriately Normed (SCAN) to Restored, Regularized Strongly Constrained and Appropriately Normed (r²SCAN)

The development of functionals getting a balance between computational efficiency and accuracy in property prediction has been a continuous effort. This is particularly evident in the evolution of mGGA functionals, starting with the introduction of the SCAN functionals. SCAN is the first mGGA that successfully satisfied all known constraints achievable by a semi-local²⁵. However, the practical application of SCAN has uncovered numerical instability issues, particularly concerning the isorbital indicator α , when compared to the more stable exchange-correlation functional of GGA²⁵.

In response, Bartók and Yates²⁵ proposed a regularized version of the original SCAN functional known as Regularized Strongly Constrained and Appropriately Normed (rSCAN). This modification not only preserves accuracy but also enhances stability by addressing issues with the SCAN isorbital parameter used to connect various approximations of the exchange-correlation energy based on the local environment. Furthermore, they describe a modification that eliminates the unphysical divergence of the exchange-correlation potential from some free atoms while preserving the isorbital indicator's proximity to the original expression in most regions²⁶. While rSCAN is an improvement over previous functionals, it has limitations. It uses a soft polynomial within the chemically relevant range, which introduces unwanted terms in the density gradient expansion that do not align with the exact expansion that SCAN recovers²⁷. The r²SCAN mGGA functional was developed to address these deficiencies. This new iteration fine-tunes the regularizations introduced in rSCAN to accomplish almost all the exact constraints satisfied by SCAN²⁸.

More recently, functionals approaches seek to incorporate instantaneous dipole moments that contribute to Van der Waals (vdW) or London dispersion interactions owing to quantum interactions. Despite being relatively weak forces and long-range nature, these interactions have a significant influence, especially in surface and interfacial reactions, such as catalytic and corrosion processes on the surface of materials^{27,29}. An illustration of this is the VV10 functional, developed by Vydrov and Voorhis³⁰, a non-local van der Waals functional that speeds up the computational process by only requiring the electron density and its first derivative as input parameters.

Heyd-Scuseria-Ernzerhof (HSE06)

While density functional theory predominantly relies on semilocal approximations such as PBE for exchange-correlation energy, these methods frequently fall short in accurately predicting band gaps and electron delocalization in materials containing *d*- and *f*- elements³¹. Hybrid functionals, which incorporate Hartree-Fock (HF) exchange, partially mitigate these problems and improve computational accuracy compared to the generalized gradient approximation. However, they come with higher computational demands, mainly for periodic systems³².

A highly efficient alternative can be found in the hybrid functionals proposed by HSE06³¹. These functionals include HF, PBE, and PBE short- and long-range exchange-correlation energy components that speed up the decay of HF exchange interactions by replacing its coulomb potential with a screened one³¹. This substitution significantly reduces computational costs, especially for extended systems. The analysis focuses on the Coulomb potential for both short- and long-range components, enhancing the accuracy and versatility of these functionals³².

This study used the PBESol, r^2 SCAN, r^2 SCAN+rVV10 and HSE06 functionals. The initial three were employed to identify that r^2 SCAN+rVV10 provides a relaxed structure with electronic properties closest to experimental results. Then, the HSE06 functional was employed to enhance the accuracy of the density further.

2.3 Vienna *ab initio* Simulation Package

Vienna *ab initio* Simulation Package (VASP) is a software designed for precise *ab initio* density functional simulations. It uses plane waves and iterative techniques developed by Georg Kresse et al. to match the accuracy of advanced all-electronic codes³³. VASP employs a projector-augmented wave (PAW) method to model electron-ion interactions, ensuring stability and accuracy when solving Kohn-Sham equations. This approach optimizes computational efficiency for systems of different sizes. Hafner mentions that one of the advantages of the PAW method is its capability to account for the complex nodal characteristics of valence orbitals while preserving orthogonality between valence and core wavefunctions.

2.3.1 Periodicity, Plane Waves and k-points

Approximating materials to perfect crystals is essential to characterize their properties, so a clear definition of the concept is crucial³⁴. A crystal refers to an endless repetition of individual atoms or groups of atoms throughout space. The smallest entity capable of generating a solid through translations is called primitive unit cell, it is defined by the lattice vectors \mathbf{a}_1 , \mathbf{a}_2 and \mathbf{a}_3 in the real space with volume $V_{cell} = |\mathbf{a}_1 \cdot \mathbf{a}_2 \times \mathbf{a}_3|$ and is mathematically written:

$$\mathbf{R} = n_1 \mathbf{a}_1 + n_2 \mathbf{a}_2 + n_3 \mathbf{a}_3, \text{ with } n_i, i = 1, 2, 3 \text{ integers} \quad (2.21)$$

This vector describes the direct lattice. Now, as we look for the properties of the material, we must introduce the reciprocal space that is defined by the reciprocal vectors:

$$\mathbf{b}_1 = 2\pi \frac{\mathbf{a}_2 \times \mathbf{a}_3}{\mathbf{a}_1 \cdot (\mathbf{a}_2 \times \mathbf{a}_3)}, \mathbf{b}_2 = 2\pi \frac{\mathbf{a}_3 \times \mathbf{a}_1}{\mathbf{a}_2 \cdot (\mathbf{a}_3 \times \mathbf{a}_1)}, \mathbf{b}_3 = 2\pi \frac{\mathbf{a}_1 \times \mathbf{a}_2}{\mathbf{a}_3 \cdot (\mathbf{a}_1 \times \mathbf{a}_2)} \quad (2.22)$$

that satisfy the condition $\mathbf{a}_i \cdot \mathbf{b}_j = 2\pi \delta_{ij}$, and represents the reciprocal lattice defined by:

$$\mathbf{G} = m_1 \mathbf{b}_1 + m_2 \mathbf{b}_2 + m_3 \mathbf{b}_3, \text{ with } m_i, i = 1, 2, 3 \text{ integers} \quad (2.23)$$

One way to solve the Kohn-Sham equations is to use the periodic nature of the Fourier series to represent wavefunctions. This representation can be expressed as a combination of a plane wave and a periodic function, a concept formally known as Bloch's theorem:

$$\phi_{\mathbf{k}}(\mathbf{r}) = e^{i(\mathbf{k} \cdot \mathbf{r})} u_{\mathbf{k}}(\mathbf{r}) \quad (2.24)$$

Here $u_{\mathbf{k}}(\mathbf{r}) = u_{\mathbf{k}}(\mathbf{r} + \mathbf{R})$ corresponds to the periodic function while $e^{i(\mathbf{k} \cdot \mathbf{r})}$ represent a plane wave, a wave with a constant value across any plane perpendicular to a fixed position. The \mathbf{r} and \mathbf{k} denote the real space and the reciprocal or \mathbf{k} -space, respectively. This theorem enables the independent search for solutions to the Schrödinger equation for each \mathbf{k} -value.

Earlier, we introduced the notion of a primitive cell in real space, and its analog in reciprocal space is known as the Brillouin Zone (BZ). The Brillouin zone is significant in band theory, particularly important at Γ point, where $\mathbf{k} = 0$. The volume in the BZ is defined as $V_{BZ} = \frac{(2\pi)^3}{V_{cell}}$.

2.3.2 Cut-off Energy

Another mathematical description of Bloch's theorem can be provided by expressing the periodic function as a summation of plane waves over all vectors defined by \mathbf{G} , which is justifiable due to its periodic nature.

$$u_{\mathbf{k}} = \sum_{\mathbf{G}} C_{\mathbf{G}} e^{i[\mathbf{G} \cdot \mathbf{r}]}, \phi_{\mathbf{k}}(\mathbf{r}) = \sum_{\mathbf{G}} C_{\mathbf{k}+\mathbf{G}} e^{i(\mathbf{k}+\mathbf{G}) \cdot \mathbf{r}} \quad (2.25)$$

Although this approach introduces complexity in the calculations since the evaluation of a single point in \mathbf{k} -space means the sum over an infinite number of possible values of \mathbf{G} , the interpretation of the solutions to these functions allows the kinetic energy to be quantitatively described³⁵:

$$E = \frac{\hbar^2}{2m} |\mathbf{k} + \mathbf{G}|^2 \quad (2.26)$$

For solutions with physical meaning, the sum is truncated to a value known as cutoff energy (E_{cut}), reducing eq 2.25 into:

$$E_{cut} = \frac{\hbar^2}{2m} G_{cut}^2, \phi_{\mathbf{k}}(\mathbf{r}) = \sum_{|\mathbf{G}+\mathbf{k}| < G_{cut}} C_{\mathbf{k}+\mathbf{G}} e^{i(\mathbf{k}+\mathbf{G}) \cdot \mathbf{r}} \quad (2.27)$$

This cutoff energy is used to determine the range of plane waves that will be included in the calculation, with only those plane waves having kinetic energies below the cutoff energy being considered, while the others are neglected. This parameter is of paramount importance as it helps maintain a balance between computational cost and an accurate representation of the electronic structure.

2.3.3 Pseudopotentials

Within an atom, both core and valence electrons coexist. Valence electrons are of particular significance because they exhibit greater sensitivity to changes in chemical bonding environments compared to core electrons, which are tightly bound to the nucleus. Consequently, only valence electrons actively participate in chemical bonding, while core electrons remain inert. When discussing systems composed of multiple heavy atoms, it becomes essential to employ the frozen core approximation¹⁸.

According to Sholl and Steckel in their book *Density Functional Theory: A Practical Introduction*²⁰, a pseudopotential is an effective potential that substitutes the electron density from core electrons with a regularized electronic charge density, designed to replicate the crucial physical and mathematical characteristics of actual ionic nuclei. Its utilization allows us to allocate computational resources exclusively to valence electrons while conserving core electrons in their isolated atomic states, simplifying calculations. An essential characteristic of pseudopotentials is their transferability. This implies that once a pseudopotential is constructed for an isolated atom, it can be seamlessly applied in diverse chemical environments without additional adjustments. The selection of a pseudopotential is influenced by the minimum energy limit required for calculations. Pseudopotentials demanding high energy cutoffs are commonly referred to as "hard", while those with lower cutoffs are termed "soft"²⁰. Among these, ultrasoft pseudopotential (USPP) are prevalent due to their low energy cutoff values, although their construction involves specifying several empirical parameters for each atom.

2.4 Density of States

In studying a material's electronic structure, the electronic density of states (DOS) is of most significant importance as it comprehensively describes the material's electronic properties. The DOS refers explicitly to the density of electronic states per unit of energy and per unit of volume when we talk about periodic systems, mathematically written as³⁶:

$$\rho(\mathbf{E}) d\mathbf{E} = d\mathbf{E} \frac{V}{(2\pi)^3} \int d^3\mathbf{k} \delta(\mathbf{E}(\mathbf{k}) - \mathbf{E}), \quad (2.28)$$

with δ function as consequence of the derivative of the energy $d\mathbf{E} \rightarrow 0$.

In graphical representations of DOS, energy is typically measured in relation to the Fermi energy (E_f), which represents the highest occupied electronic state at absolute zero temperature ($T = 0\text{K}$). To calculate it, one integrates the electronic density derived from prior density functional theory (DFT) calculations across the k-space. This information is then interpreted by identifying regions corresponding to the valence and conduction bands. The valence band comprises all occupied electronic states, while the conduction band encompasses all unoccupied states

(As shown in Fig.2.2). The presence or absence of a separation between these two bands defines what is commonly referred to as the bandgap, and it contains no electronic states. Whether a material possesses a bandgap is a defining factor in classifying it as a semiconductor, metal, or insulator. Furthermore, the properties of this bandgap often dictate the practical applications of semiconductors in various technological fields.

PDOS (Projected Density of States) Gives the projection of particular orbital of particular atom on the density of states. So, if you sum over all the projections, you will have the total density of state, or simple, the DOS

For a more precise understanding of localized states within a material, it is possible to decompose the electronic density into components associated with specific orbitals. This decomposition is known as the Partial Density of States (PDOS), defined as the number of electronic states with energies weighted by the fraction of the total electron density corresponding to the volume surrounding a nucleus²⁰.

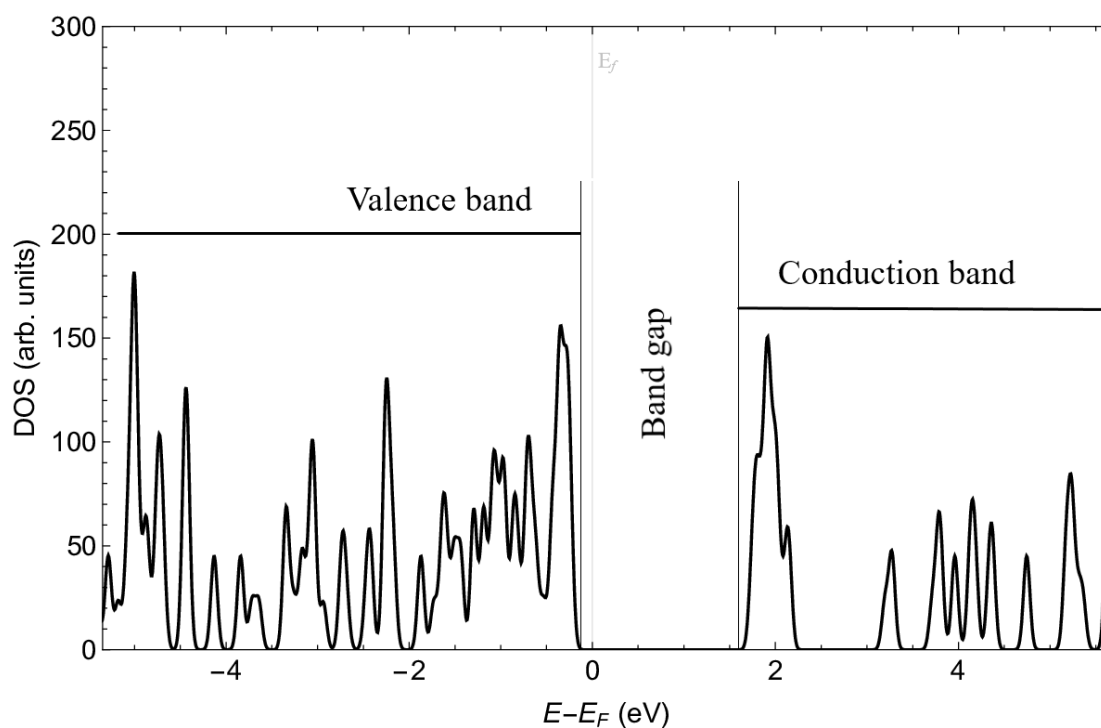


Figure 2.2: Electronic density of states with respect to the Fermi energy (E_f) of our calculated Ce-UiO-66 metal-organic framework presented in Section 4 with a clear differentiation of valence and conduction band and the presence of a band gap that separates both bands for this particular case.

2.5 Photocatalysis in MOFs

Photocatalysts, which facilitate chemical reactions upon absorbing light, can be solid semiconductors that must meet specific criteria: efficient visible and/or UV light absorption, chemical stability, cost-effective and non-toxic³⁷. The process involves exciting electrons from the valence band to the conduction band, leaving holes in VB, and forming electron-hole pairs¹³. These charge carriers migrate to the surface and participate in reactions with absorbed substrates.

When light interacts with MOFs, it can generate charge separation states. MOFs exhibit four distinct frontier orbital orientations, including ligand-ligand, ligand-metal, metal-ligand, and metal-metal excitations where the nature of the band edge relies on MOFs composition⁹. Transitions between ligands and metals are of particular interest, as they spatially separate electrons and holes, leading to prolonged exciton lifetimes thus prevents rapid recombination⁹, a crucial factor for the photocatalytic activity of a material. To assess the efficiency of this charge transfer, it is considered E_{LMCT} , which measures the energy change during electron transfer from the excited bonding orbital to the lowest unoccupied metal orbital⁵. An efficient photocatalytic MOF exhibits a lower energy level in the metal orbital than the donor level (lowest unoccupied linker orbital), resulting in a negative E_{LMCT} ⁵. This negative value indicates the potential for long-lived charge-separated states, with the hole in the linker and the electron on the metal ion³⁸.

Successful photocatalysis within metal-organic frameworks relies on extended carrier lifetimes, appropriate redox potential for substrate reactions, efficient light absorption, rapid charge separation, and effective migration to catalytic active sites for substrate interactions¹³.

2.5.1 Ionization potential

Butler et al.³⁹ have discovered an expression for understanding and explaining materials' electrochemical, photocatalytic, and photovoltaic properties. This expression involves integrating the electrostatic potential, with Φ representing the spherical average of the potential, r as the radius, and V as the volume. It calculates the spherical average of the electrostatic potential at the pore center:

$$\Phi_{av}(r) = \int_V \Phi(r') d^3r' \quad (2.29)$$

This approach enables us to compare electronic energy variations by aligning them with the vacuum level, a process made possible after identifying the plateau potential. The plateau potential defines the region within the unit cell where the potential consistently remains stable⁹. We can establish the positions of the edges of the valence (VB) and conduction (CB) bands with respect to the vacuum level, thus facilitating comparisons with reaction potentials, such as those governing water oxidation and hydrogen reduction. Therefore, for the desired electron transfer processes to occur after irradiation, the edges of the conduction band must be situated above the reduction potential. In contrast, the edges of the valence band remain below that of the desired reaction⁹.

Chapter 3

Methodology

This chapter provides a comprehensive overview of the methodologies and tools employed throughout this study to analyze electronic structure. It covers the construction of metal-organic frameworks and the establishment of optimal computational parameters for framework relaxation calculations. Additionally, it explains the management of input and output files for VASP simulations, electrostatic potentials to determine vacuum potentials, and analytical programs, including VESTA, Mathematica, and Python, to extract and interpret essential data.

3.1 Building the Structures

The construction of organometallic structures was performed computationally using Material Studio, with our primary objective being the discovery of efficient photocatalytic materials. As a result, the main structure for most calculations was based on the $M_6O_4(OH)_4$ node, consisting of six cerium (Ce) metal ions and twelve 1,4-benzenedicarboxylate (BDC) ligands, which gives rise to a unit cell formed by 114 atoms. This combination forms the Ce-UiO-66 metal-organic framework (MOF), as illustrated in Fig.3.1.

After obtaining the cerium-based structure, subsequent modifications became more straightforward. In this study, we build eight distinct structures: two of them were derived from altering the metal in the node ($M = Ti, Ce$), three resulted from combinations of the previous metals ($M = Ti_3Ce_3$), and the remaining three emerged through the linker functionalization. The metal change within the node was done simply by selecting the atom and choosing the desired metal. Introducing metallic mixtures was more complex since identifying the possible arrangements depended on the resulting symmetry; a different symmetry indicated a new configuration. In Fig.3.2, the obtained SBUs during the node modification are shown.

As mentioned above, the generated cells initially contained at least one hundred atoms. As modifications were introduced, particularly in cases involving topological defects, this count increased to over four hundred atoms. To handle these calculations computationally, we harnessed the processing power of a supercomputer at the University of Gdansk in Poland.

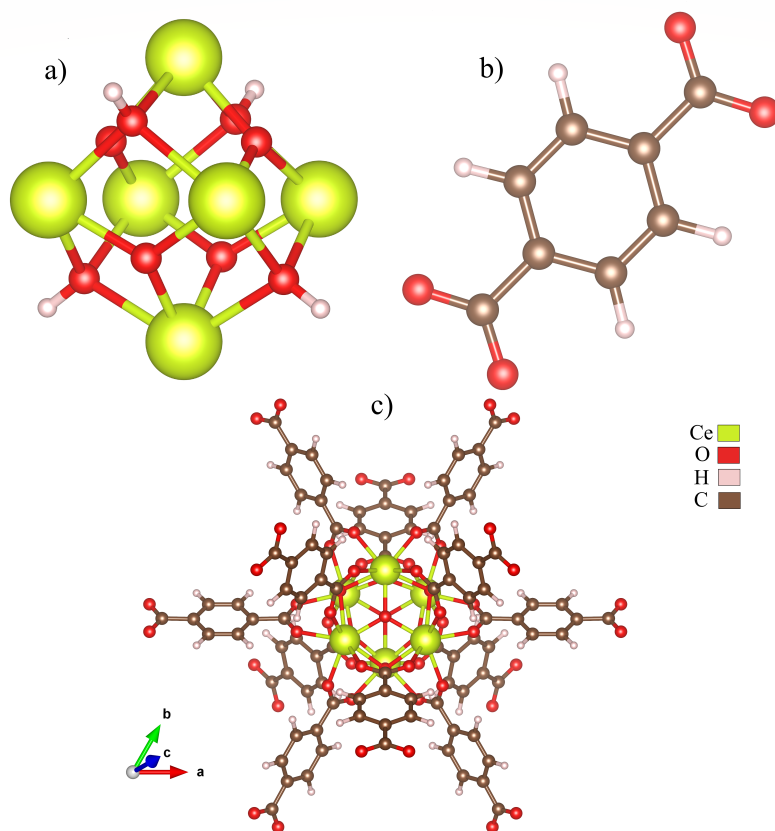


Figure 3.1: Building Metal-Organic Frameworks a) MOF's node constructed with cerium metal ions b) 1,4-benzenedicarboxylate (BDC) linker c) Ce-UiO-66 resulting structure.

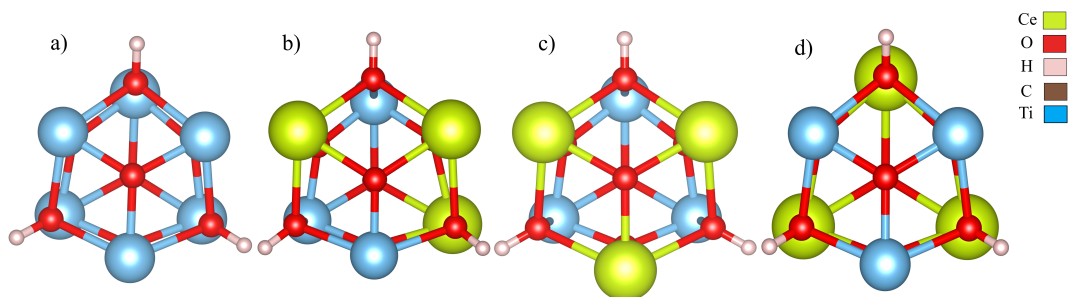


Figure 3.2: Collections of the nodes or Secondary Building Units obtained with a) Titanium metal and mixed metals ions differentiated by their symmetry b) Ti_3Ce_3 (Sym1) c) Ti_3Ce_3 (Sym8) d) Ti_3Ce_3 (Sym160).

3.1.1 Introducing Defects

Any defect in the MOF must be handled with care since any alteration in the node or the ligand affects the porosity, catalytic activity, absorption capacity, and structure, enhancing some properties but decreasing stability¹⁰. The bandgap, defined as the difference in energy between the valence and conduction bands, plays a crucial role in photocatalysts. It represents the minimum energy required for an absorbed photon to generate an electron-hole charge carrier pair, which can then be directed to active sites, driving redox reactions⁴⁰. Since much of the solar energy falls within the visible region, it is essential that the proposed materials have photoactivity within this spectrum. A very effective method for this involves functionalizing the linker with specific substituents, such as amino groups and amides, capable of absorbing visible light and increasing the number of occupied states near the valence band⁴¹.

Generally, the catalytic activity in MOFs originates mainly from unsaturated metal centers, although it may depend on catalytic species within the pores. However, the functionalization of the ligands also modifies the catalytic performance. Thus, we analyze the distribution of energy bands with amine functionalization of only one linker shown in Fig.3.3.

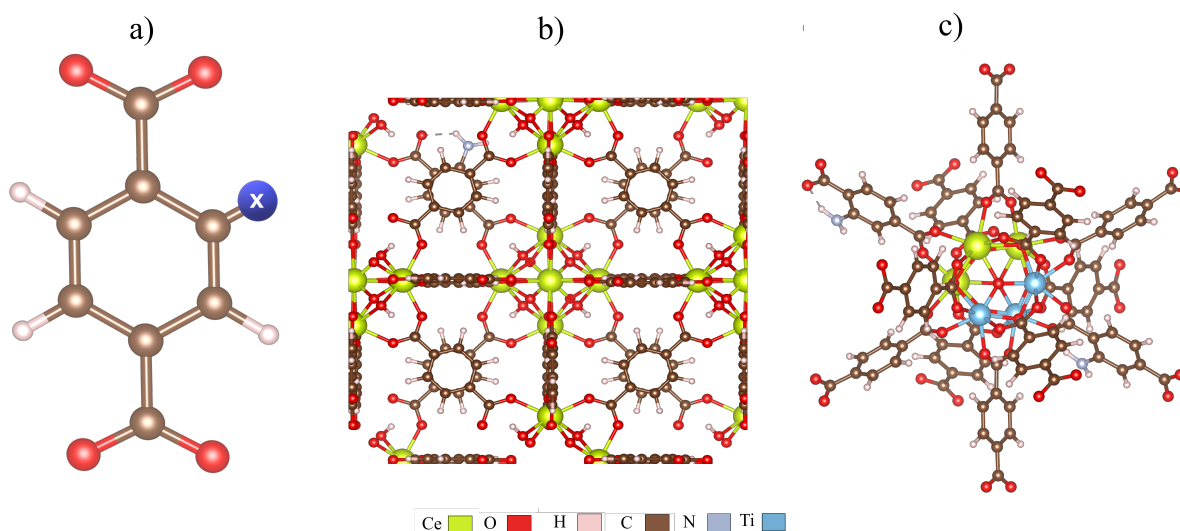


Figure 3.3: Functionalizing the linker with an amine group: a) X denotes the amine's position in forming the 2-aminobenzene-1,4-dicarboxylate ligand. b) Depicts the primitive cell of the topological defect at single linker functionalization (Ce-UiO-66-NH₂), while c) corresponds to the unit cell of Sym8 after linker functionalization, resulting in the Sym8-UiO-66-(NH₂)

3.2 Computational Parameters

In preparation for running VASP scripts, we initiated the process by determining essential parameters, including cutoff values and k-point selections. Following this, we obtained an optimal volume to determine the optimal configuration for electronic density and vacuum potential data.

3.2.1 Cutoff Energy (E_{cut})

In our previous discussion, we emphasized the significance of the cutoff energy (E_{cut}) in VASP calculations. Now, let us delve into the process of selecting this parameter for different structures.

E_{cut} is chosen with reference to the highest kinetic energy in the system, typically that of a free electron⁴²:

$$E_{cut} \geq \frac{1}{2}|\mathbf{k} + \mathbf{G}|^2 \quad (3.1)$$

It sets an upper limit for including plane waves in the calculation, ensuring accuracy. In systems with multiple atoms, a specific cutoff energy is assigned for each element, and the highest assigned value within the cell becomes the overall cutoff energy²⁰. We established the cutoff individually for each system, taking into account a convergence criterion of 1 meV. The E_{cut} employed for calculations of Ce-UiO-66 (See Fig.3.4), and Ti-UiO-66 MOF (See Fig.3.5 for convergence sampling) corresponds to 1050 and 950 eV, respectively. When both metals were mixed in a single node, we used the higher value of 1050 eV for all subsequent calculations.

3.2.2 K-points Selection

For sampling k-points, the Monkhorst-Pack method was used, which generates a grid of points spaced uniformly along the irreducible Brillouin zone. Thus, having a large cell, a single point, is enough to describe the properties in this zone. The center point is known as Γ -point ($\mathbf{k}=0$). It is important because the real and reciprocal coordinates coincide so that the wave functions are real, and no consideration is necessary for complex numbers. Using high symmetry around this point further increases computational efficiency, reducing calculation time, with the choice being advantageous for large-scale computations.

We selected the grid based on the total energy per atom with the set of k-points, using a gamma-centered Monkhorst-Pack grid. It is important to note that the values of the analyzed k-mesh fall within the convergence range of 1 meV. Therefore, a $1 \times 1 \times 1$ grid is sufficient for the calculations with a separation of $\delta k = 0.07 \text{ \AA}^{-1}$.

3.2.3 Birch-Murnaghan Equation of States

It is time to describe how we determine the values for relaxing the structures. We will begin with the equation of states, a mathematical expression used in condensed matter physics. It establishes a relationship between the system's volume V and the pressure P applied to it⁴³. A general form of this relation is the third-order Birch-Murnaghan equation of states, mathematically described as⁴⁴:

$$P(V) = \frac{3}{2}B_0 \left[\left(\frac{V_0}{V} \right)^{\frac{7}{3}} - \left(\frac{V_0}{V} \right)^{\frac{5}{3}} \right] \left[1 + \frac{3}{4}(B'_0 - 4) \left\{ \left(\frac{V_0}{V} \right)^{\frac{2}{3}} - 1 \right\} \right] \quad (3.2)$$

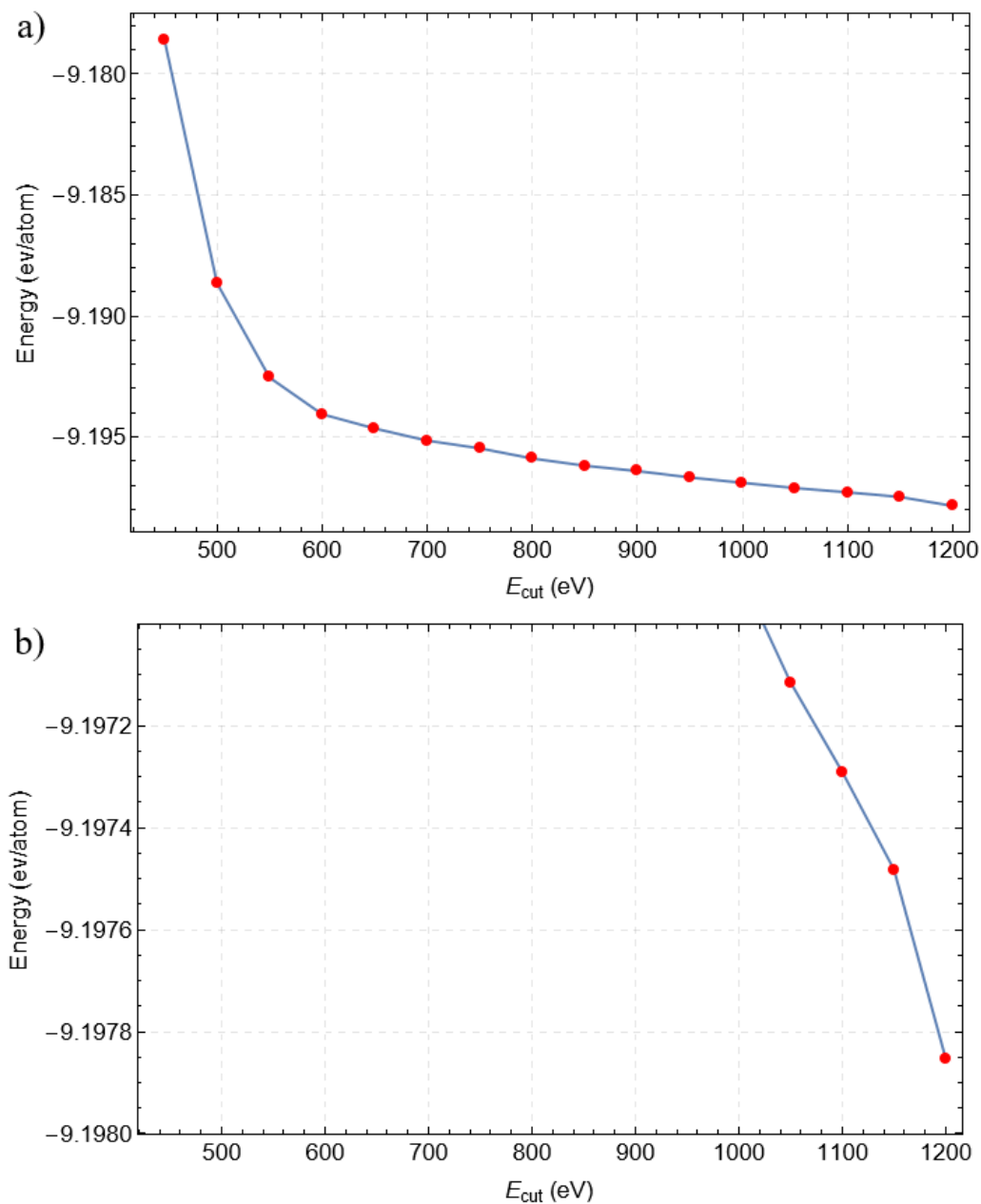


Figure 3.4: a) Selection of the plane wave cutoff energy b) Considering a range of 1 meV/atom, the convergence starts with $E_{cut} = 1050$ eV for the Ce-system.

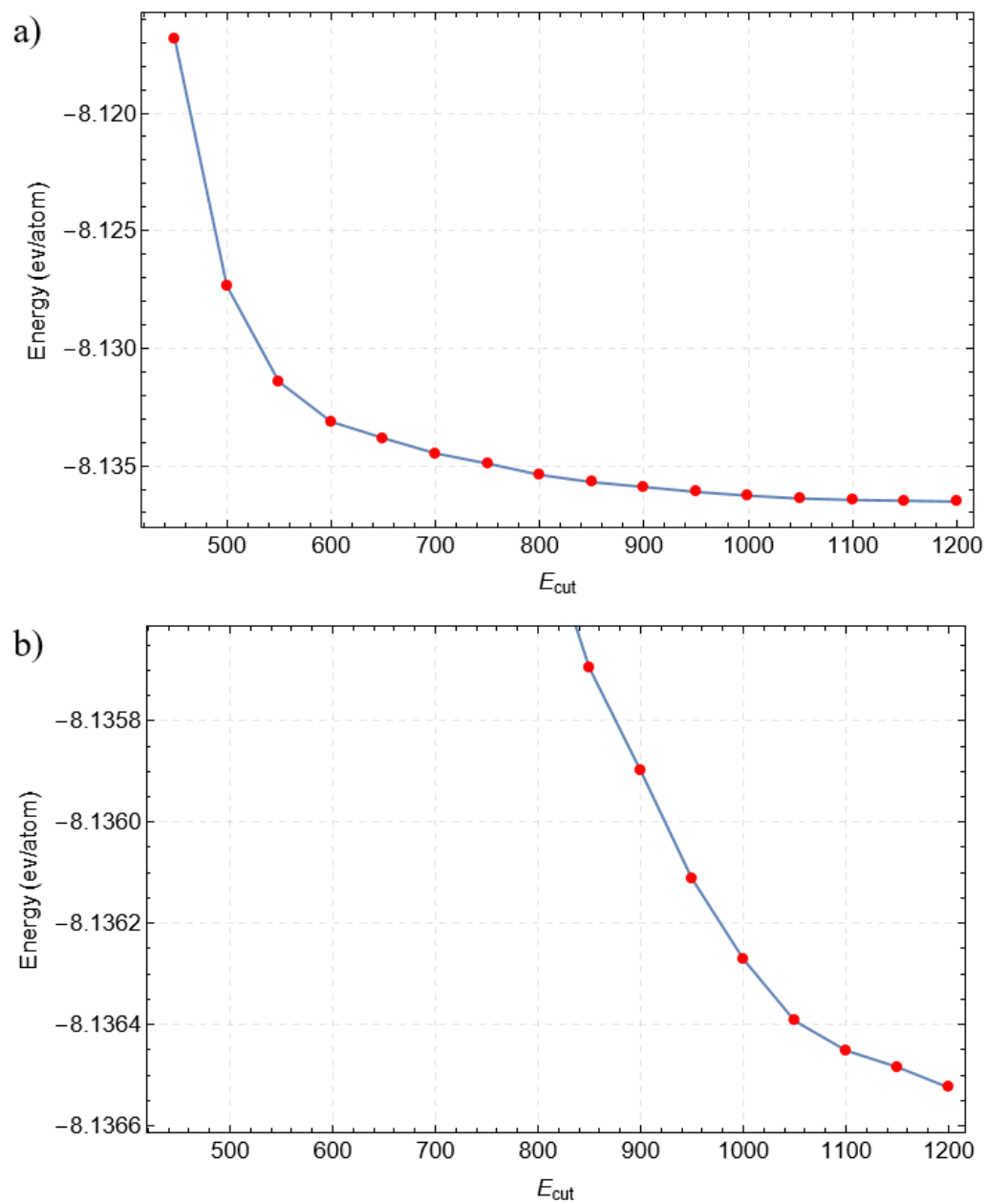


Figure 3.5: a) Selection of the plane wave cutoff energy b) Considering a range of 1 meV/atom, the convergence starts with $E_{cut} = 950$ eV for the Ti-system.

An expression for the pressure as a function of the volume where V_0 , B_0 and B'_0 corresponds to the equilibrium unit cell volume, the bulk modulus, and its first derivative with respect to the pressure, respectively or numerically expressed⁴⁵:

$$B_0 = -V_0 \frac{\partial P}{\partial V}, \quad B'_0 = \frac{\partial B_0}{\partial P} \quad (3.3)$$

Then, the theoretical ground state energy as a function of the unit cell volume $E(V)$ can be easily evaluated using *ab initio* electronic techniques and fitting the data to Murnaghan equation⁴³:

$$E(V) = E_0 + \frac{9V_0 B_0}{16} \left\{ \left[\left(\frac{V_0}{V} \right)^{\frac{2}{3}} - 1 \right]^3 B'_0 + \left[\left(\frac{V_0}{V} \right)^{\frac{2}{3}} - 1 \right]^2 \left[6 - 4 \left(\frac{V_0}{V} \right)^{\frac{2}{3}} \right] \right\} \quad (3.4)$$

Thus, we have values for the properties of the structures studied in this work, especially B_0 , a measure of the material's resistance under pressure and the volume that optimizes the energy for electronic density calculations. It is important to mention that during relaxation, we allowed changes in volume, cell, and internal structure. The equation of state also serves as an indicator of the accuracy of the chosen calculation parameters, such as k-points and cutoff energy, based on the smoothness of the curve. Any dispersion of points would indicate that the parameter base are not be solid.

3.3 VASP Implementation

Initial inputs are required to perform calculations in VASP: INCAR, KPOINTS, POSCAR, POTCAR (See Appendix. A for detailed description). We start with the INCAR file, in which parameters such as cutoff energy and the functional used to obtain the electronic structure are specified⁴⁶. We used Generalized Gradient Approximation: PBEsol, meta-GGA: r²SCAN and r²SCAN+rVV10 and hybrid functionals: HSE06.

We followed with KPOINTS, which contains the k-points that describe the Brillouin Zone⁴⁷. For all the calculations throughout this project, the Monkhorst-Pack method was used. The POSCAR file contains the cell lattice vectors, atomic species, and ionic positions⁴⁸. Finally, the POTCAR has the pseudopotentials describing atomic interactions for each species⁴⁹. To generate this file considering a system with more than one species like our case, they must be arranged following the order described in POSCAR.

An executable is used that invokes the initial inputs and performs the calculation. As a result, various files are generated, including:

- OUTCAR contains information on initial conditions, forces on atoms, local charges, magnetic moments, and more⁵⁰.
- CONTCAR, with a format similar to POSCAR but written after each complete ion step⁵¹.
- WAVECAR stores wave function coefficients in binary format⁵².
- DOSCAR details the full and partial density of states⁵³.

Files like WAVECAR are essential for generating the density of states, whereas CONTCAR and DOSCAR enable us to analyze the obtained density using Mathematica.

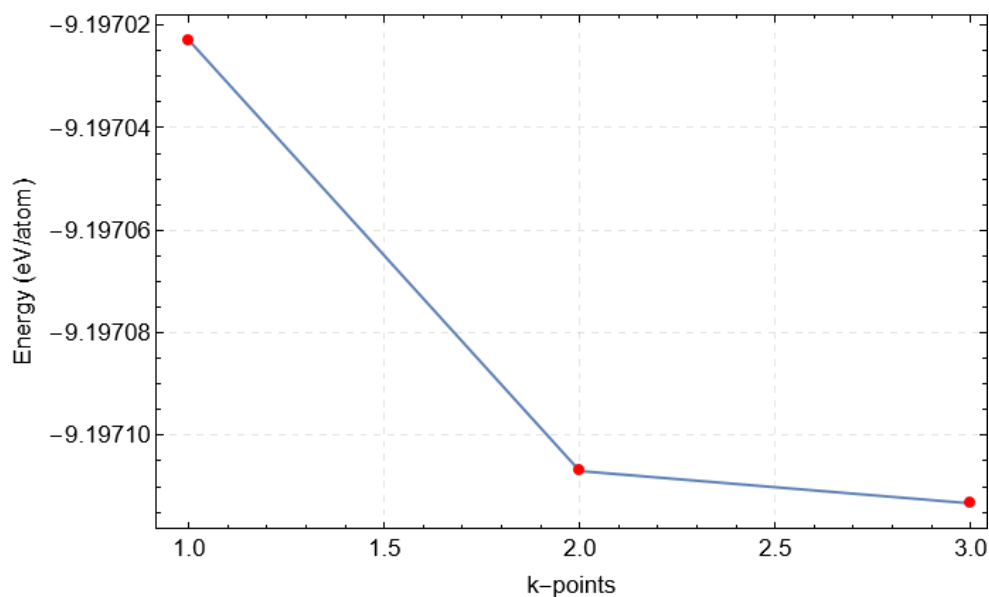


Figure 3.6: For K-points selection, the convergence in point separation length of Ce-UiO-66 is achieved within an energy range of 1 meV/atom, and this convergence begins at $k = 1 \times 1 \times 1$

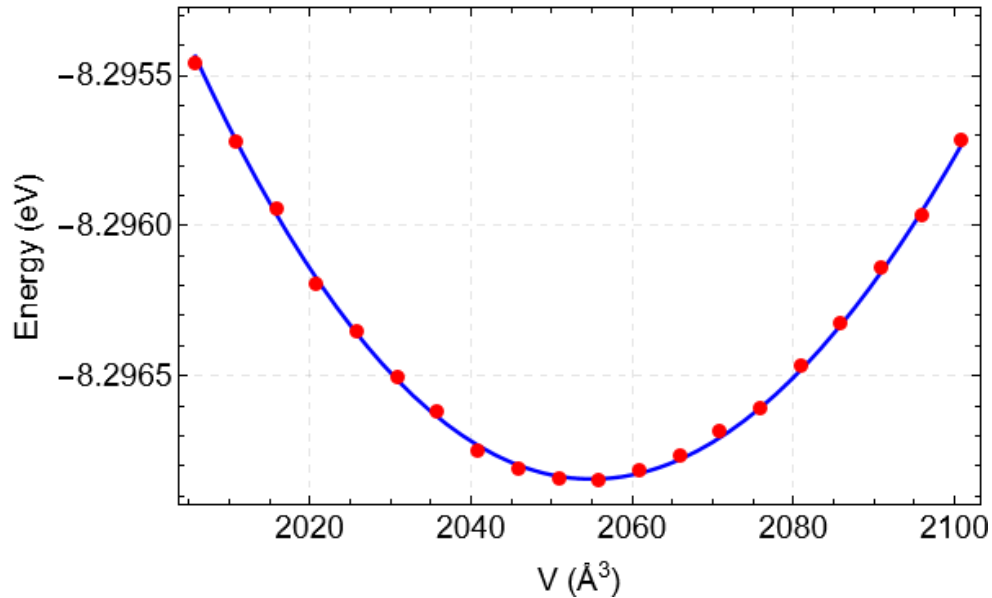


Figure 3.7: The Birch-Murnaghan equation of state (represented by the solid blue line) is derived from fits to data obtained with rSCAN+rVV10 functional (represented as red dots) for the metal-organic framework (MOF) of titanium. This analysis provides values for volume $V = 2054.99 \text{ \AA}^3$ and bulk modulus $B_0 = 0.36 \text{ GPa}$

3.4 Determining the Vacuum Potential

A major challenge in investigating porous structures for photocatalytic and photovoltaic applications was the need for a reference scale for electronic energy levels. Butler et.al³⁹. proposed a solution by accessing the potential of the vacuum in the center of the pore, which establishes values for the binding of electrons in the material. Likewise, he showed that the electrostatic potential at this same point can be used as a reference to locate electronic energy levels on a scale.

Our research achieved this after optimizing the atomic structure, relaxing the atomic positions, and evaluating the electron density, electrostatic potential, and bandgap obtained with the hybrid exchange functional method (HSE06). A relevant part of our analysis was identifying the **plane** where the pore was located, whose distribution stabilizes as it approaches the center and has the highest electrostatic potential value. To do this, the LOCPOT file was examined in VESTA, followed by using the library SphericalAverage in python, which calculates the spherical average of the electrostatic potential at the center point of the pore. In our study, we analyzed several planes, with the (1 0 -1) plane yielding the highest electrostatic potential value.

Thus, we found spherical radii with dimensions ranging from 1 to 20 Å, an electrostatic potential of 4.06 eV with a variation of less than 1×10^{-5} V for the Ce-UiO-66 case. This potential value helped define the work function and align the energy levels within our system.

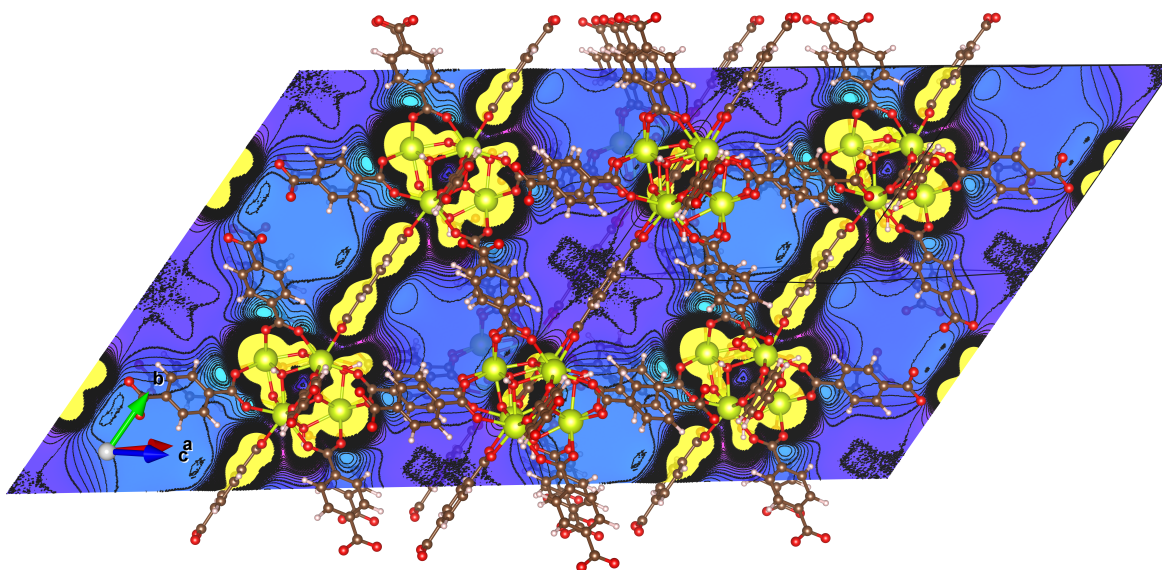


Figure 3.8: A periodic representation of the Ce-UiO-66 structure with its electrostatic potential used to determine the vacuum potential

Chapter 4

Results & Discussion

This section presents the results of our calculations performed using VASP. We provide the energy alignment of each structure with respect to the vacuum level, which serves as a key parameter for comparing the photocatalytic properties of these structures in the context of redox reactions.

4.1 PBESol, r²SCAN, r²SCAN+rVV10 and HSE06

We started this research by selecting the most suitable functional from among GGA (PBESol), MetaGGA (r²SCAN, r²SCAN+rVV10) and hybrid functionals (HSE06) to approximate the ground state energy and obtain an accurate description of the electronic configuration in the system.

We compared different functionals using the experimental bandgap calculated with the ultra violet visible (UV-Vis) spectra and Mott-Schottky (M-S) plot by Hu et al.⁵⁴ of $E_g = 2.71$ eV for the Ce-UiO-66 MOF. In our computational analysis, we obtained bandgap estimates of 1.60 eV for PBESol, 1.73 eV for r²SCAN, 1.77 eV for r²SCAN+rVV10 and 2.78 eV for r²SCAN+rVV10/HSE06. The hybrid functional yielded the closest value to the experimental result, with a small difference of only 0.07 eV. On the contrary, for r²SCAN+rVV10, r²SCAN and PBESol, the discrepancies increased to $\Delta E_g = 0.94$ eV, $\Delta E_g = 0.98$ eV and $\Delta E_g = 1.78$ eV, respectively. This observation aligns with existing literature, which suggests that GGA functionals tend to underestimate bandgaps, requiring the inclusion of exact exchange (Hartree-Fock)⁹. Overall, we observed lattice parameters ranging between 21.589-21.611 Å (Table 4.1 provides the crystallographic data obtained by the functionals used). It is worth noting that all the functionals overestimate the experimental value of the lattice parameter. However, among the three, PBE and r²SCAN+rVV10 yielded the lowest values, with a variation of $\Delta a = 0.106$ Å. Since the bandgap of r²SCAN+rVV10 is the closest to the experimental value compared to PBE, we have opted to use the r²SCAN+rVV10 functional for future electronic calculations, taking into consideration the nature of the bonding within our structure. Furthermore, our density of states analysis, as depicted in Fig.4.1, indicated minimal changes with GGA and meta GGA functionals. However, the hybrid functional showed a notable shift in the conduction band, averaging 1.08 eV higher than the other functionals and resulting in a E_g closest to the experimentally observed.

As a result, future electronic structure calculations will use r^2 SCAN+rVV10, which offers computational efficiency, and then refine the results using HSE06 due to its accurate estimation of band properties in these systems.

Table 4.1: Crystallographic and electronic structure data computed for Ce-UiO-66 with PBESol, r^2 SCAN, r^2 SCAN+rVV10 and r^2 SCAN+rVV10/HSE06 functionals and *Expt* experimental values reported by Lammert et al.⁴. Here a , b and c are the lattice parameters, α , β and γ the angles, V_{opt} is the optimal volume, B_0 the bulk modulus, E_{cut} is the cutoff energy required for calculations and E_g represents the bandgap. In the case of r^2 SCAN+rVV10, the value of E_g between brackets is the computed electronic structure using HSE06 with the optimal structure yielded by r^2 SCAN+rVV10.

Property	PBESol	r^2 SCAN	r^2 SCAN+rVV10	Expt.
$a = b = c$ (Å)	21.579	21.611	21.580	21.473 ⁴
$\alpha = \beta = \gamma$ (°)	60.00	60.00	60.00	60.00
V_{opt} (Å ³)	2509.61	2523.15	2512.27	2475.25 ⁴
B_0 (GPa)	0.29	0.28	0.30	
E_{cut} (eV)	950	950	1050	
E_g (eV)	1.60	1.73	1.77 [2.78]	2.71 ⁵⁴

4.2 Node Modifications

Our study focuses on modifying the nodes within the Zr-UiO-66 metal-organic framework to improve its photocatalytic properties. To begin, we replaced the original Zr metal nodes with Cerium (Ce) and Titanium (Ti) as our initial step.

4.2.1 Ce-UiO-66

Electronic density analysis

After achieving convergence of the initial parameters (k-points and E_{cut}) with a total energy within 1 meV per atom, we proceeded to compute the optimal relaxed structure using the r^2 SCAN+rVV10 functional. Fig.4.2 a) the unit cell presenting the arrangements of atoms in this optimal structure. A curve fitting analysis using the third-degree Birch-Murnaghan equation was computed to extract essential material properties, including volume and bulk modulus. The outcomes of this analysis are presented in Table 4.2, alongside the crystallographic data.

In pursuit of a more precise characterization of the electron density within the material, the HSE06 hybrid functional was employed to the r^2 SCAN+rVV10 previous calculations. The result yields a DOSCAR file used for plotting the Partial Density of States (PDOS). Fig. 4.3 illustrates the PDOS with the contribution of each atom to

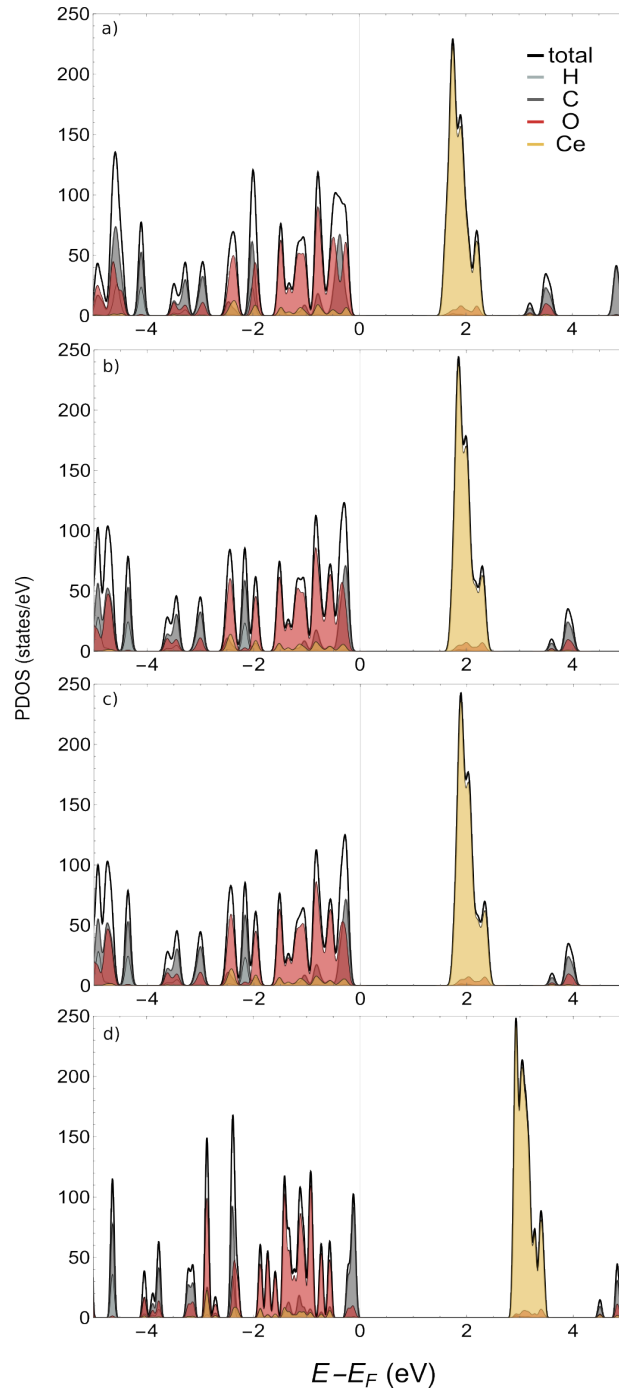


Figure 4.1: Computed Partial density of states corresponding to the Ce-UiO-66 system with the functionals: a)PBESol, b)r2SCAN, c)r²SCAN+rVV10, and d) r²SCAN+rVV10/HSE06, with an energy difference between valence and conduction band of 1.60 eV, 1.73 eV, 1.77 eV, and 2.78 eV, respectively.

the electronic bands. In this PDOS plot, it is evident that a bandgap exists separating the valence and conduction bands, with a measured value of $E_g = 2.78$ eV. Additionally, we can distinguish the predominant contributions within each band. The atoms constituting the linker (C, H, O) are notably predominant in the valence band, while in the conduction band, the major contributions are coming from the metal in the node (Ce in this case).

Electrostatic and vacuum potential

While the DOSCAR file is being generated, a LOCPOT file is also created containing the electrostatic potential values of the material. This LOCPOT file is then analyzed in VESTA to identify the maximum potential value at the center of one of three distinct pores within this structure. This specific pore records a reference value of 4.06 eV for electrostatic potential within the (1 0 -1) plane, precisely at a quarter of the distance from the lattice vector, as indicated in Fig.4.4 with a circle. Their corresponding vacuum potential or work function $\Phi = 7.60$ eV. Aligning the electron density data with the vacuum potential allowed us to precisely determine the bandgap value $E_g = 2.78$ eV.

By analyzing Fig.4.5 a) that shows the band alignment with respect to the vacuum potential, it becomes apparent that ligand-to-metal charge transfer (LMCT) phenomenon occurs similarly than in Zr-UiO-66 MOF⁵. From this result, it is evident that the valence band, representing the highest unoccupied states, begins with the *f* orbital metal's contribution and exhibits an energy level lower than that of the lowest unoccupied linker orbital (See Appendix B.1 for detailed orbital resolved partial density of states). Consequently, we observe a negative energy difference, which contributes to an extended lifetime of an excited state being desirable for photocatalysis⁵.

4.2.2 Ti-UiO-66

Electronic density analysis

In a similar way to the Ce-based MOF, we have determined initial parameters for the Ti-MOF. The optima relaxed Ti-MOF structure were obtained, which is illustrated in Fig.4.6. The corresponding density of states (DOS) is also depicted in Fig.4.7. Notably, when comparing Ce-MOF to Ti-MOF, we observe considerably smaller values, which can be attributed to differences in the number of electrons for each element and the interactions between them.

Regarding the density of states, replacing the metal of the node with titanium leads to a conduction band shift, resulting in a band gap of $E_g = 3.73$ eV, which is 0.95 eV wider than that of the cerium-based MOF. For photocatalytic materials operating within the visible spectrum, band gaps exceeding 3.0 eV are typically considered unsuitable. However, for reactions, such as water splitting, a narrower bandgap range of $1.23 < E_g < 3.26$ eV is desirable³⁷ that could be addressed by introducing defects.

Electrostatic and vacuum potential

The procedure for aligning the DOS with respect to the vacuum potential was the same as described before. The pore was located within the (1 0 -1) plane, a quarter away from the lattice vectors. In this region, the electrostatic potential measured 4.50 eV, with a work function of $\Phi = 7.50$ eV and a bandgap $E_g = 3.73$ eV. This pore is visually represented in Fig.4.8 with a circle and a summary of the properties of Ce- and Ti-MOF is presented in Table 4.2.

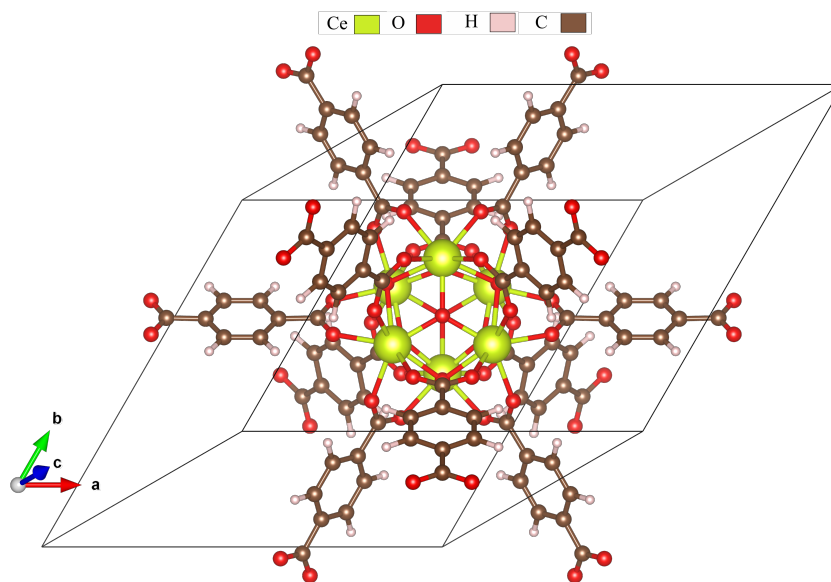


Figure 4.2: The unit cell of Ce-UiO-66 after relaxation using r^2 SCAN+rVV10.

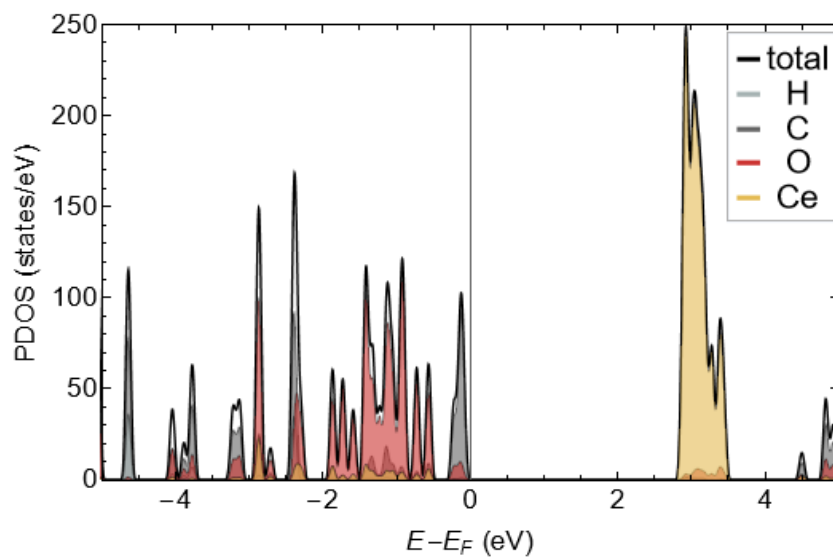


Figure 4.3: Partial Density of States (PDOS) calculated using the r^2 SCAN+rVV10/HSE06 functional for the Ce-UiO-66 structure. The highest occupied states predominantly originate from the atoms in the linker. In contrast, the lowest unoccupied states are primarily associated with the metal ions, resulting in a calculated bandgap of $E_g = 2.78$ eV.

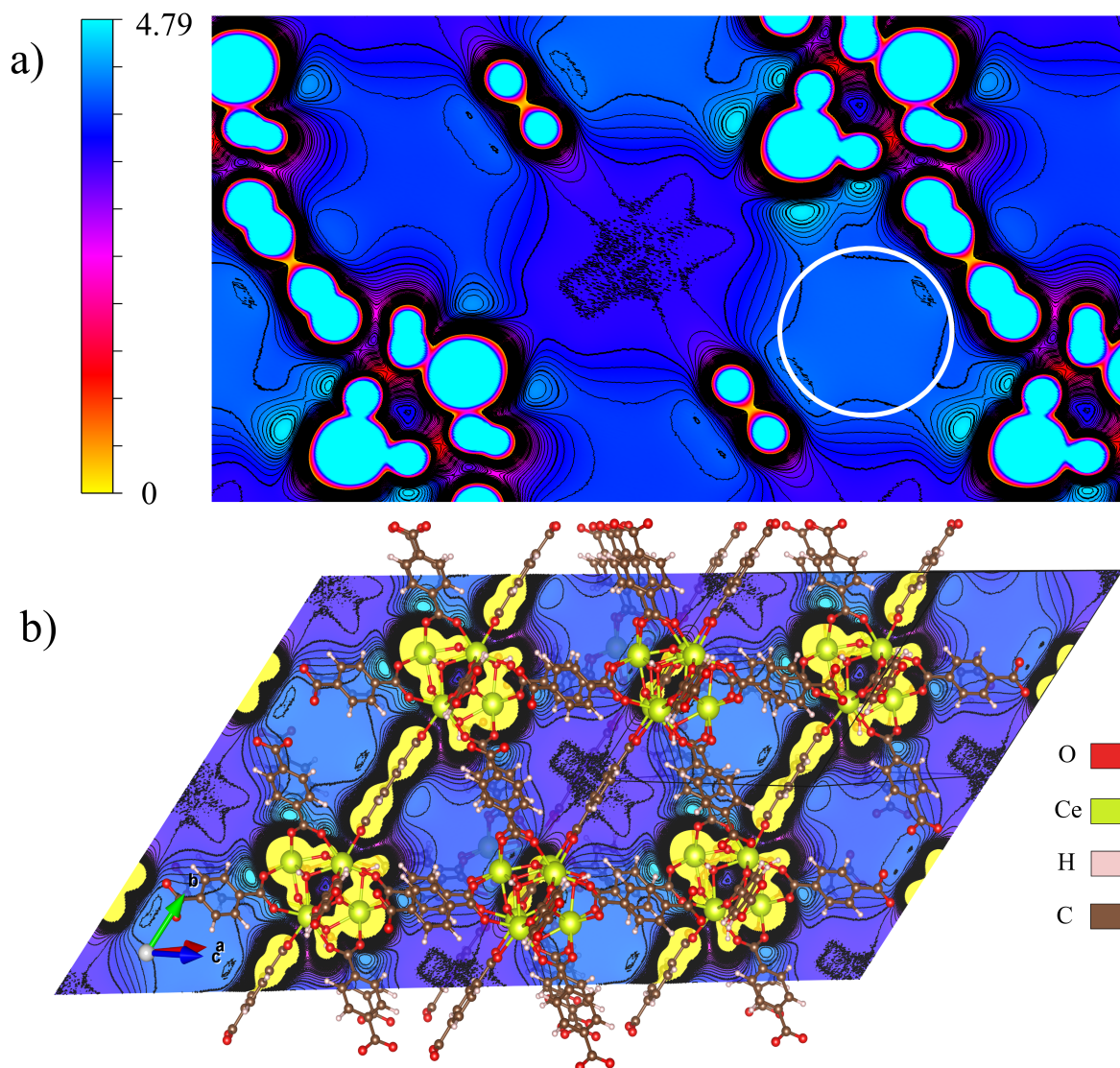


Figure 4.4: a) A 2D slice of the electrostatic potential of Ce-UiO-66 in the (1 0 -1) plane where the pore with the highest electrostatic potential value was located a quarter of the lattice vector, indicated with a white circle. b) A periodic representation of the structure along with its corresponding electrostatic potential.

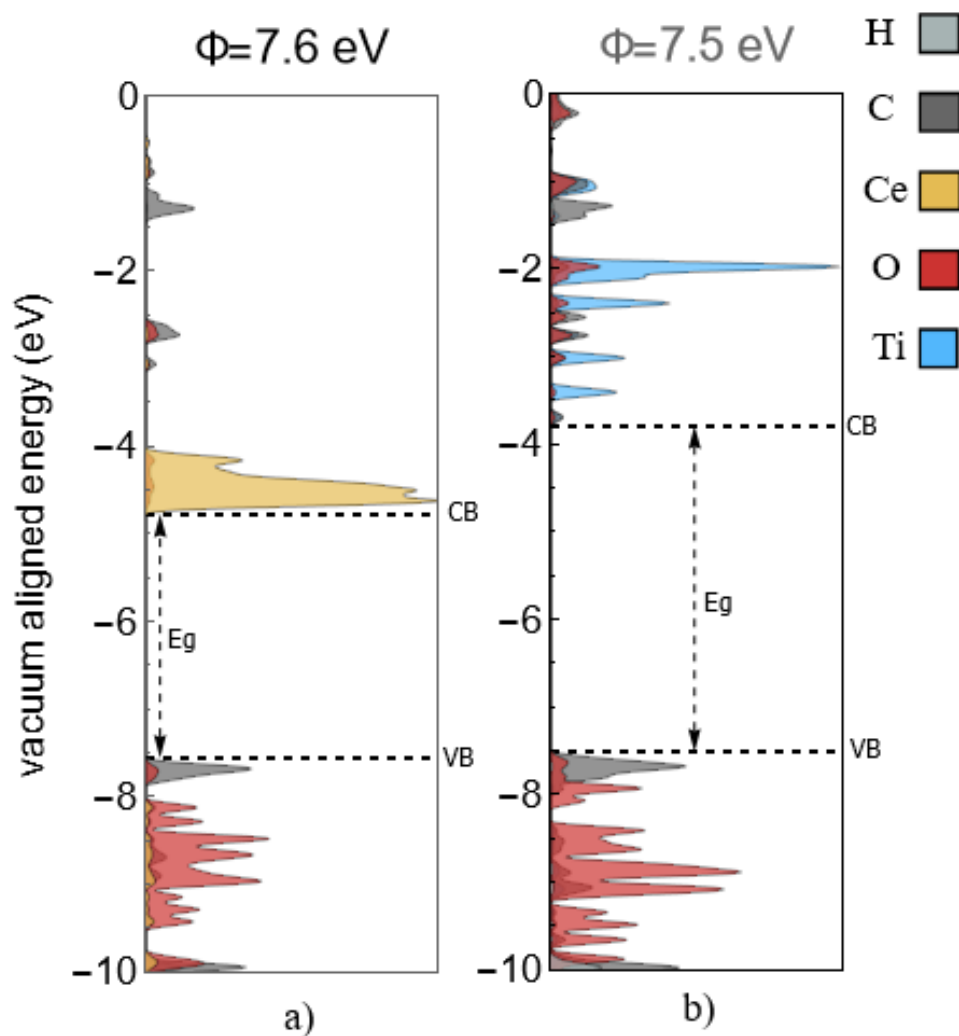


Figure 4.5: Partial Density of States (PDOS) for a) Ce-UiO-66 and b) Ti-UiO-66 configurations calculated using r^2 SCAN+rVV10/HSE06 functionals. The band gap (E_g) and band edge positions are aligned with respect to the vacuum level and are detailed in Table 4.2. In this graph, it is evident that altering the metal node results in changes in the band structure. Notably, in the case of Ti compared to Ce, the conduction band is shifted by approximately 1 meV, with this shift primarily attributed to the Ti d orbital contribution.

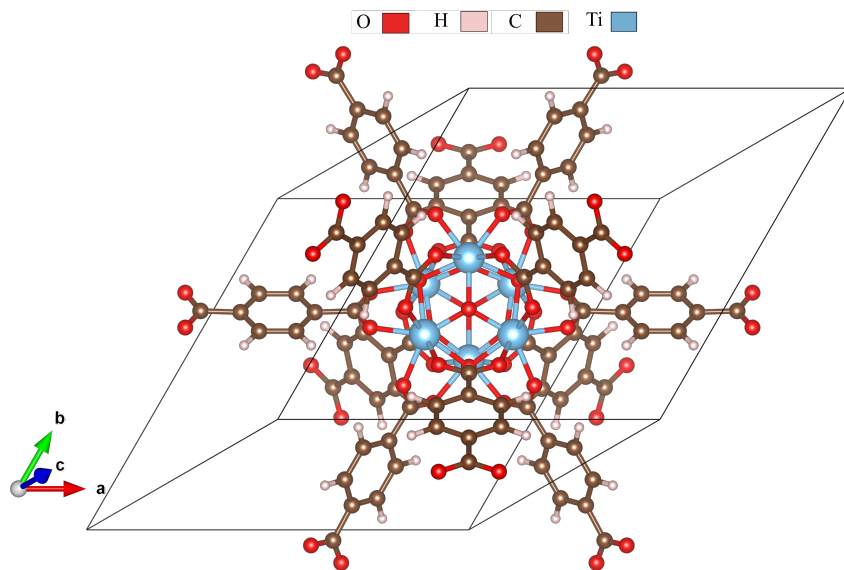


Figure 4.6: The unit cell of Ti-UiO-66 after relaxation using r^2 SCAN+rVV10.

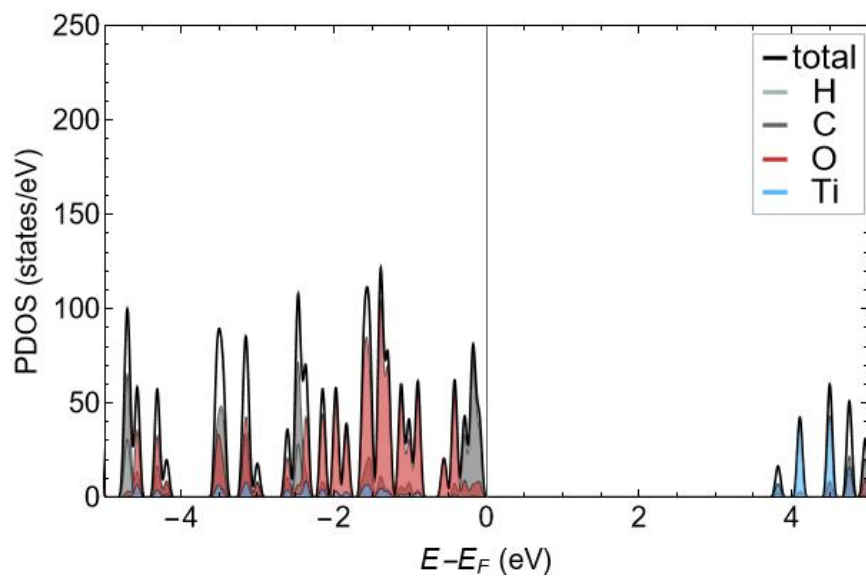


Figure 4.7: Partial Density of States (PDOS) calculated using the r^2 SCAN+rVV10/HSE06 functional for the Ti-UiO-66 structure. The highest occupied states from the valence band predominantly originate from the atoms in the linker, whereas the lowest unoccupied states in the conduction band are primarily associated with the metal ions, resulting in a calculated bandgap of $E_g = 3.73$ eV

Unlike Ce-MOF, Ti-UiO-66 does not exhibit ligand-metal charge transfer, as the highest occupied and lowest unoccupied states correspond to the p orbitals of carbon atoms in the ligand (refer to Fig.4.5 b). This suggests a ligand-to-ligand charge transfer (LLCT), indicating that the lifetime of the photoexcited state may not be as extended as in materials characterized by LMCT. Consequently, this limitation affects its photocatalytic properties.

To determine whether ligand-to-ligand charge transfer occurs within different ligands or within the same one, we closely examined the PDOS of all carbon atoms. Our observations revealed that electrons are delocalized within the linker. In the conduction band, the carbon contribution comes from the twelve carbons (C12) that are connected to the oxygens near the node, while in the valence band, the main contribution comes from the carbon atoms that are located below C12. As a result, it is not possible to determine whether this is an intra- or inter-ligand charge transfer.

Table 4.2: Crystallographic data were computed using the r^2 SCAN+rVV10 functional for the Ti- and Ce-UiO-66 structures. In these calculations, a , b , and c represent the lattice parameters, while α , β , and γ denote the lattice angles. The optimal volume is denoted as V_{opt} , B_0 represents the bulk modulus, E_{tot} the total energy and N_{at} the total number of atoms. Additionally, E_{cut} signifies the cutoff energy required for the calculations. Electronic properties, such as the bandgap E_g and work function Φ , were determined using the r^2 SCAN+rVV10/HSE06 method.

Property	Ce-UiO-66	Ti-UiO-66
Space Group	$216 : F-43m$	
$a = b = c$ (Å)	15.26	14.27
$\alpha = \beta = \gamma$ (°)	60.00	60.00
V_{opt} (Å ³)	2512.27	2054.99
B_0 (GPa)	0.30	0.36
E_g (eV)	2.78	3.73
Φ (eV)	7.60	7.50
E_{tot} (eV)	-1048.522	-945.842
N_{at}	114	114

4.2.3 Ti₃Ce₃-UiO-66

Electronic density analysis

In this new challenge of incorporating multiple metals into a node, the resulting structures consist of various atomic species, which are crucial in selecting the computational parameters. We prioritize the highest values within the unit cell, determined separately for each metal, to accurately represent the behavior in these new structures. This selected value aligns with that of Cerium with $E_{cut} = 1050$ eV applied to all subsequent calculations. Furthermore, the optimal volumes were determined being 2272.17 Å³ for Ti₃Ce₃-UiO-66 (Sym160), 2272.26 Å³ for Ti₃Ce₃-UiO-66

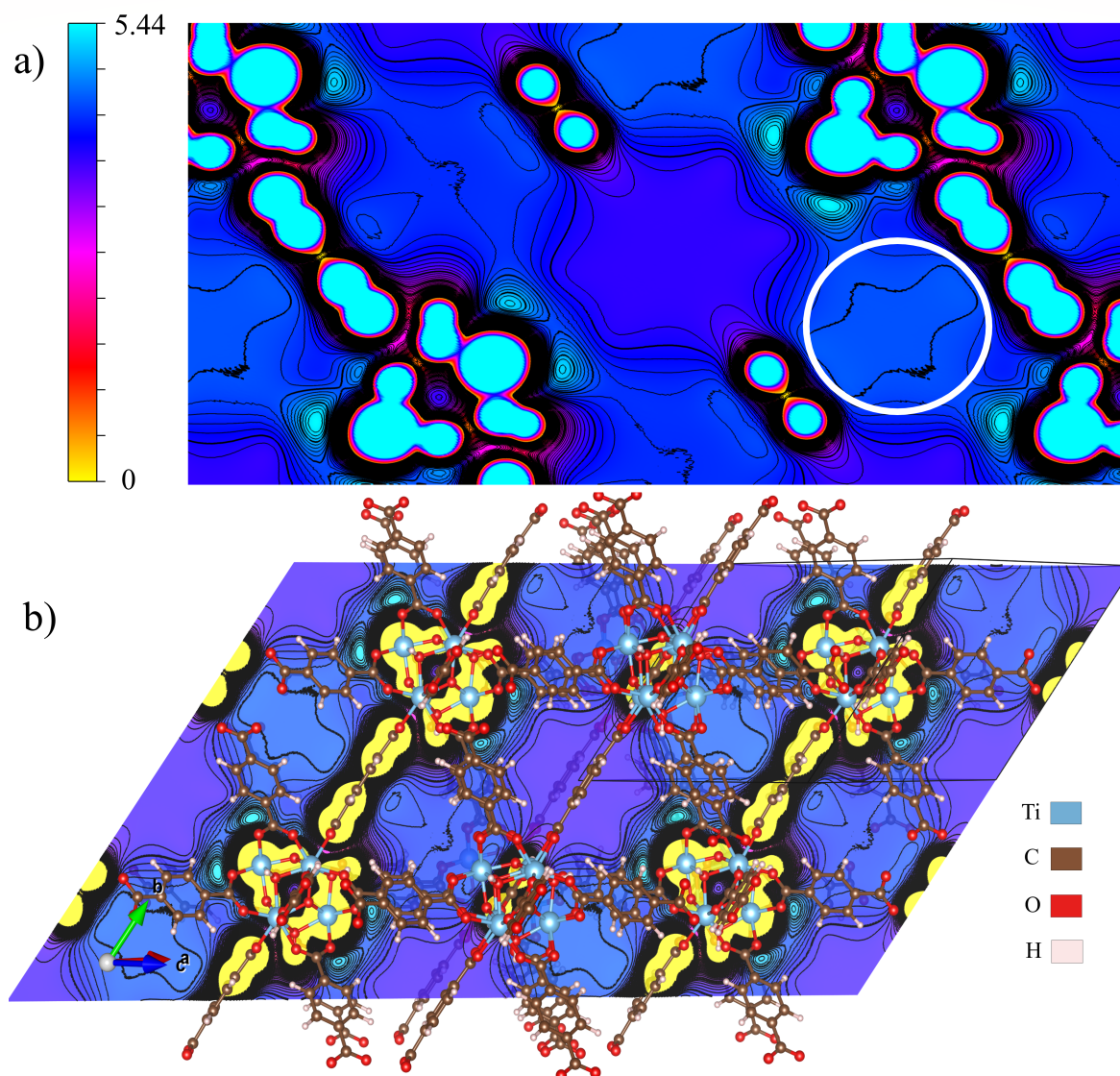


Figure 4.8: a) A 2D slice of the electrostatic potential of Ti-UiO-66 in the (1 0 -1) plane where the pore with the highest electrostatic potential value was located a quarter of the lattice vector, indicated with a white circle. b) A periodic representation of the structure along with its corresponding electrostatic potential.

(Sym8), and 2282.13 \AA^3 for $\text{Ti}_3\text{Ce}_3\text{-UiO-66}$ (Sym1) when seeking the optimal configuration. Fig.4.9 displays their corresponding unit cells.

The obtained optimal value represents an average of cerium and titanium MOFs in all cases. The values of the bulk modulus range from 0.28-0.31 GPa. These values indicate that the structures are more compressible, and their volumes may undergo alterations under pressure. This characteristic is largely attributed to the presence of pores within the structures.

In our exploration of changes in the electronic structure of a mixed node within an organometallic framework, an exhaustive examination of all possible configurations was conducted. Distinguishing one configuration from another relied on their respective symmetries, with each new symmetry indicating a unique structure. In total, three viable arrangements were identified, each associated with a specific space group number. These space group numbers were used to simplify their names and facilitate clear reference without confusion.

Now, concerning the density of states, as we can see in Fig.4.10, two out of three structures, Sym160 and Sym8, show a behavior in the conduction band similar to Ce-MOF, resulting in a bandgap of to $E_g = 2.79 \text{ eV}$. In contrast, Sym1 exhibits a bandgap of $E_g = 2.61 \text{ eV}$ that is 0.18 eV and 1.12 eV smaller than those obtained in the Ce and Ti MOFs, which is particularly interesting among the three symmetries. In terms of stability, it can be concluded that the most stable structure is Sym8, followed by Sym160, while Sym1 is the least stable with the highest value of the relative energy $\Delta E_{tot} = 1.102 \text{ eV}$.

Electrostatic and vacuum potential

In order to determine the center of the pore with the highest electrostatic potential, pores were examined in several planes. Among them, the (1 0 -1) plane, located a quarter of the distance from the lattice vectors within the plane, was where this particular pore was identified. This resulted in electrostatic potential values of 4.27 eV for Sym160 and Sym8 and 4.24 eV for Sym1, along with vacuum potential values of 7.50 eV, 7.50 eV, and 7.40 eV, respectively. These values closely resemble those found in the titanium structure but are lower than those observed in cerium structure.

When examining the energy alignment with respect to the vacuum potential, the ligand-to-metal charge transfer (LMCT) was observed in all the configurations: Sym1, Sym160 and Sym8. Upon closer examination of Fig.4.11, it can be said that in the valence band, the major contributions come from the linker, specifically the *s*, *p*, and *d* orbitals of H, C, and O, respectively. In the conduction band, we found contributions from *f* and *d* orbitals of Ce and Ti, respectively. This result suggests that this mixture of metals ensures transfer from linker to metal.

4.3 Defects

The defects applied in our system focused on the functionalization of the ligand with an amine group. Four systems were examined: Ce, Sym160, Sym1, and Sym8, excluding the titanium case because it does not present LMCT.

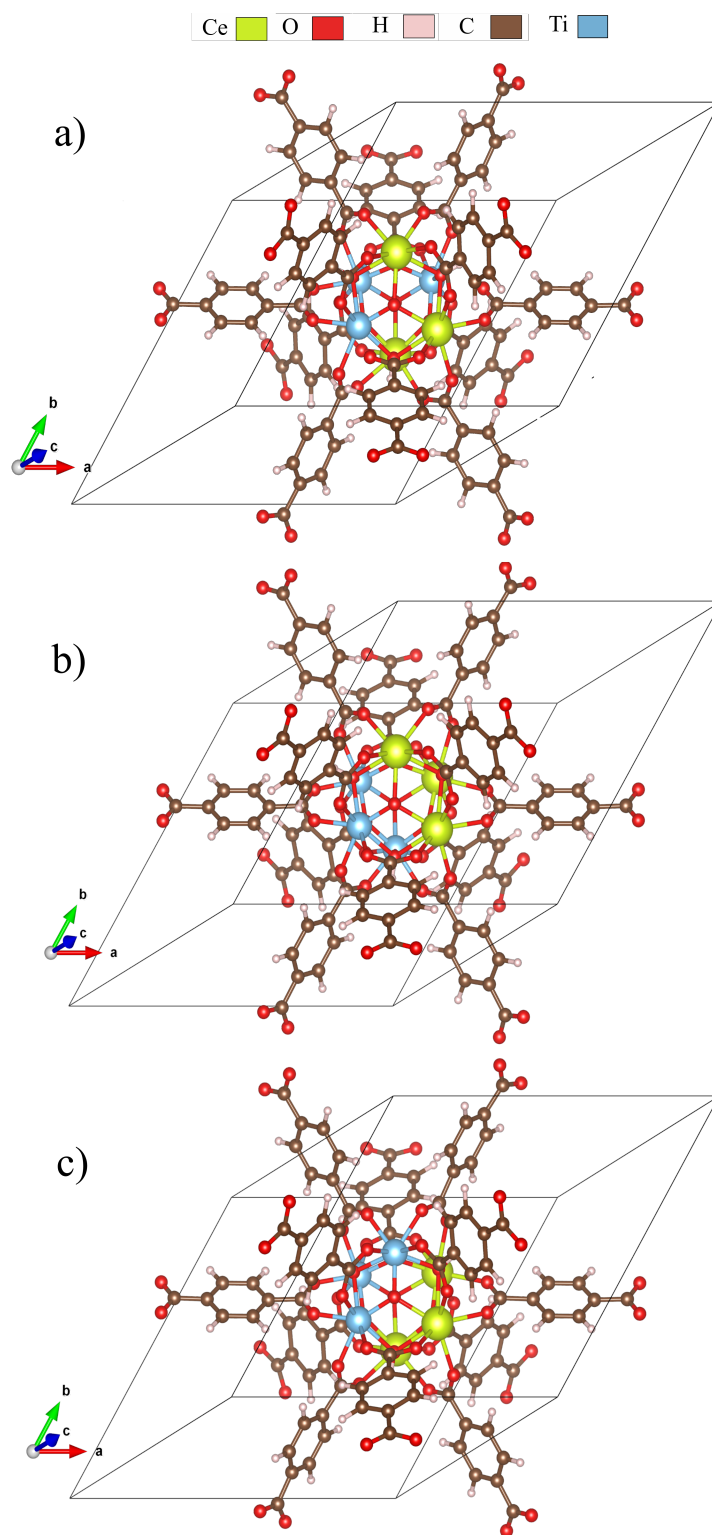


Figure 4.9: The unit cell of $\text{Ti}_3\text{Ce}_3\text{-UiO-66}$, with a mixed-metal node, was subjected to relaxation using the $r^2\text{SCAN+rVV10}$ functional. Three distinct configurations were obtained, each characterized by a different symmetry: a) Sym1 b) Sym160 c) Sym8

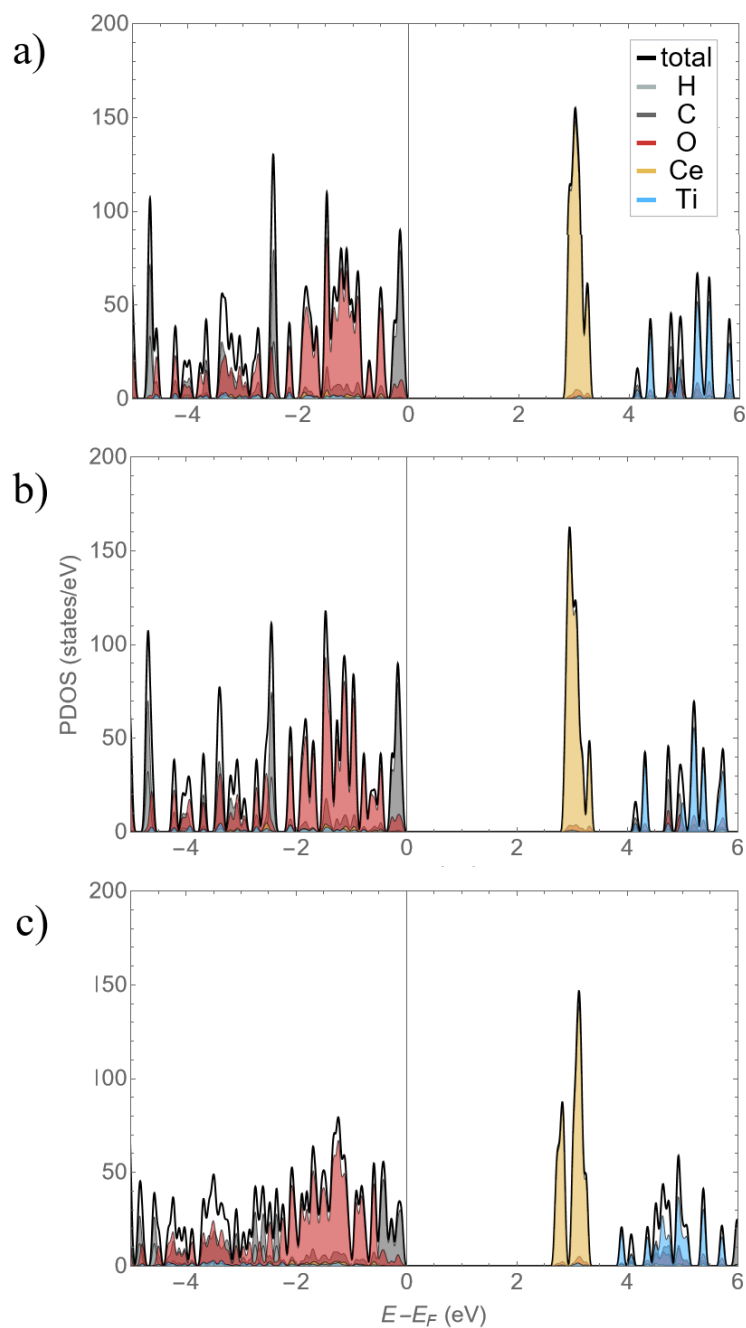


Figure 4.10: Partial Density of States (PDOS) was computed using the r^2 SCAN+rVV10/HSE06 functional for three distinct structural variants of $\text{Ti}_3\text{Ce}_3\text{-UiO-66}$: a) Sym160, b) Sym8 and c) Sym1. In the PDOS plots, the most substantial contributions to the valence band originate from C, O, and H atoms. In contrast, the conduction band is predominantly composed of contributions from the metal ions. The Fermi level was aligned to 0 eV, and the bandgap values were determined to be $E_g = 2.79$ eV, $E_g = 2.79$ eV, and $E_g = 2.61$ eV for Sym160, Sym8, and Sym1, respectively.

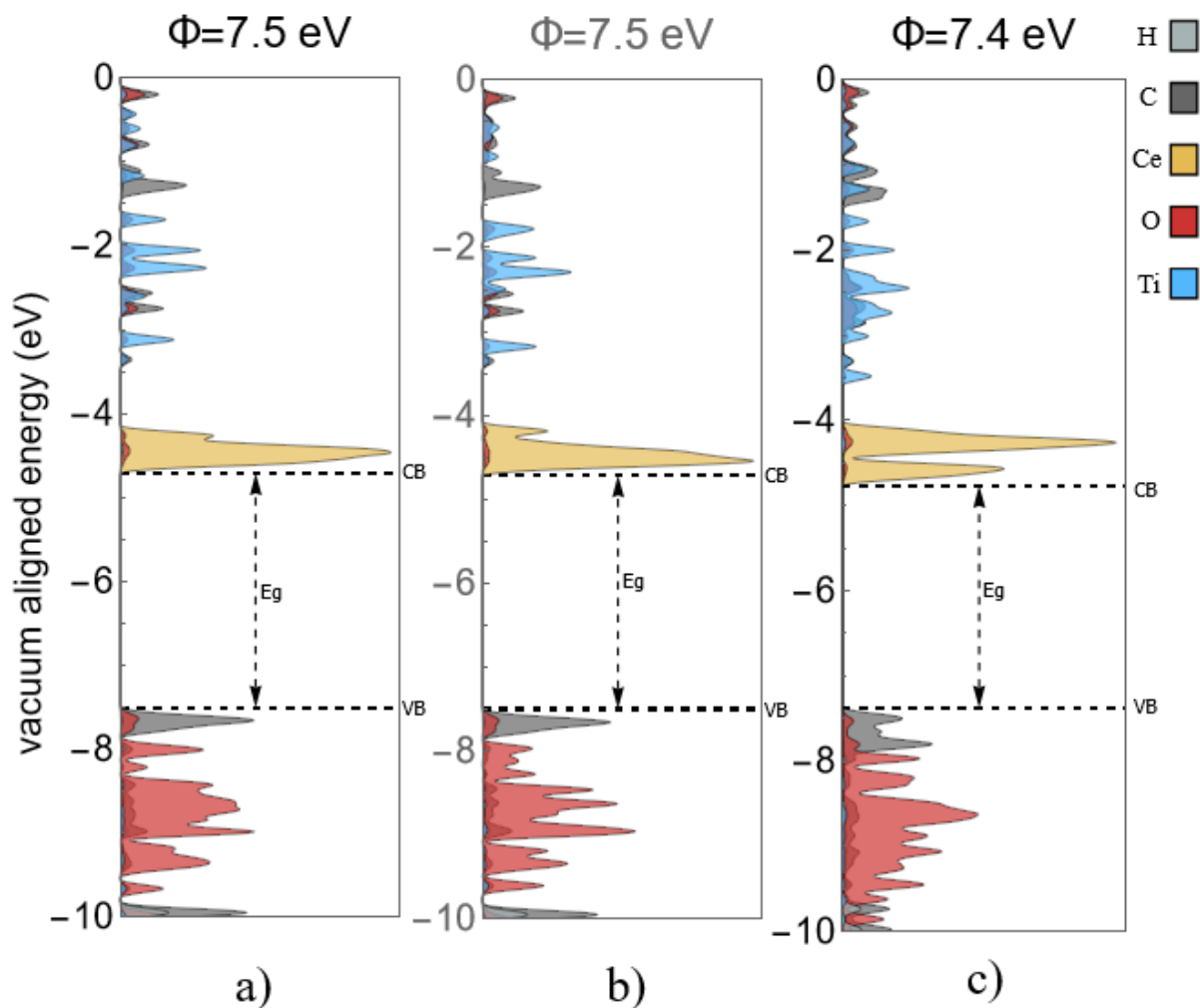


Figure 4.11: Partial Density of States (PDOS) for a) Sym160, b) Sym8, and c) Sym1 configurations were calculated using r^2 SCAN+rVV10/HSE06 functionals. In all cases, the primary contributions in the valence band originate from the *s*, *p*, and *d* orbitals of H, C, and O in the linker, while in the conduction band, contributions come from the *f* and *d* orbitals of Ce and Ti. Band gap (E_g) and band edge positions are referenced to the vacuum level and detailed in Table 4.3.

Table 4.3: Crystallographic data were computed using the r^2 SCAN+rVV10 functional for the $\text{Ti}_3\text{Ce}_3\text{-UiO-66}$ structures. In these calculations, a , b , and c represent the lattice parameters, while α , β , and γ denote the lattice angles. The optimal volume is denoted as V_{opt} , B_0 represents the bulk modulus, the relative energy ΔE_{tot} with respect to the stable configuration (Sym8) and N_{at} the total number of atoms. Electronic properties, such as the bandgap E_g and work function Φ , were determined using the r^2 SCAN+rVV10/HSE06 functional.

$\text{Ti}_3\text{Ce}_3\text{-UiO-66}$			
Property	Sym160	Sym8	Sym1
Space Group	<i>160:R3m</i>	<i>8:Cm</i>	<i>1:P1</i>
a (Å)	14.81	14.78	14.84
b (Å)	14.81	14.73	14.74
c (Å)	14.81	14.73	14.79
α (°)	59.49	59.91	60.30
β (°)	59.49	60.13	59.51
γ (°)	59.49	60.13	59.99
V_{opt} (Å ³)	2272.17	2272.26	2282.13
B_o (GPa)	0.31	0.31	0.28
E_g (eV)	2.79	2.79	2.61
Φ (eV)	7.50	7.50	7.40
ΔE_{tot} (eV)	0.039	0.0	1.102
N_{at}	114	114	114

4.3.1 Electrostatic and vacuum potential

While conducting computation on our functionalized linker within our system (M-UiO-66-X , where M is the metal and X is the amine group NH_2). We observed a consistent shift in the valence band across all cases, followed by a notable reduction in the bandgap; the values calculated were 1.34 eV, 1.36 eV, 1.38 eV, and 1.37 eV for Ce-UiO-66-X, Sym160-X, Sym8-X, and Sym1-X, respectively. A substantial reduction compared to Ce and Ti systems. This reduction can be attributed to the N- p orbital contribution (As detailed in the Appendix B.6, B.7, B.9, B.8). Other computation studies of Ce-UiO-66-X reported a bandgap of 1.17⁵ eV different from our value of 0.17 eV.

Similar to previous cases the pore with the highest electrostatic potential was found in the plane (1 0 -1) at a quarter of the way along the lattice vector. The resulting electrostatic potential values were 3.84 eV for Ce-UiO-66-X and Sym8-X, 4.34 eV for Sym160-X, and 4.33 eV for Sym1-X. These values correspond to an ionization potential of 5.90 eV for Ce-UiO-66-X, 5.60 eV for Sym8-X, and 6.10 eV for Sym160-X and Sym1-X. In terms of stability, due to its total energy, Sym160-X structure is the most stable followed by Sym8-X and Sym1-X.

With respect to ligand-to-metal charge transfer (LMCT) in Ce-UiO-66-X, Sym160-X, Sym1-X, and Sym8-X,

the highest occupied orbital in the valence band originates from the p orbital of the nitrogen within the ligand, while the major contribution to the lowest unoccupied orbital in the conduction band comes from the f orbital of the cerium atom.

Table 4.4: Crystallographic data were computed using the r^2 SCAN+rVV10 functional for the Ti_3Ce_3 -UiO-66-X structures, where X denotes an amine group (NH_2). In these calculations, a, b, and c represent the lattice parameters, while α , β , and γ denote the lattice angles, E_{cut} the total energy and N_{at} the number of atoms. Electronic properties, such as the bandgap E_g and work function Φ , were determined using the r^2 SCAN+rVV10/HSE06 functional.

Property	Ti_3Ce_3 -UiO-66- NH_2			
	Ce-UiO-66- NH_2	Sym160- NH_2	Sym8- NH_2	Sym1- NH_2
a (Å)	21.58	14.81	14.79	14.79
b (Å)	21.58	14.81	14.73	14.73
c (Å)	21.58	14.81	14.73	14.73
α (°)	90.00	59.49	59.91	59.91
β (°)	90.00	59.49	60.13	60.13
γ (°)	90.00	59.49	60.13	60.13
E_g (eV)	1.34	1.36	1.38	1.37
Φ (eV)	5.90	6.10	5.60	6.10
E_{tot} (eV)	-4207.213	-1009.576	-1009.574	-1009.574
N_{at}	458	116	116	116

4.4 Photocatalysis in Metal-Organic Frameworks

Our main goal was to find and propose structures possessing photocatalytic properties, primarily for water splitting and CO_2 reduction. It is crucial to determine the bandgap and the absolute band edge positions relative to the vacuum potential to assess the feasibility of photocatalytic reactions. To achieve this goal, it requires the free energy change per electron from a reduction reaction provided by Wu et al.⁵, and detailed in Table 4.5.

In the context of water-splitting reactions, the Highest Occupied Crystal Orbital (HOCO) must lie below the energy level of the Oxygen Evolution Reaction (OER), which is situated at -5.09 eV. Simultaneously, the Lowest Unoccupied Crystal Orbital (LUCO) must exceed the energy level of the Hydrogen Evolution Reaction (HER) at -3.87 eV. These considerations are made under standard conditions of $T = 298.15$ K and $pH = 7$. For CO_2 reduction, the LUCO should surpass the CO_2 reduction's energy level, which varies depending on the specific product formed.

Fig.4.15 presents the absolute band edge positions, with HOCO in red and LUCO in blue, for all systems, in addition to the redox potential for water splitting indicated by a dotted line. Our findings indicate that our computed structures enable H_2O/O_2 reactions, while only Ti-MOFs additionally allow H^+/H_2 reactions. We have

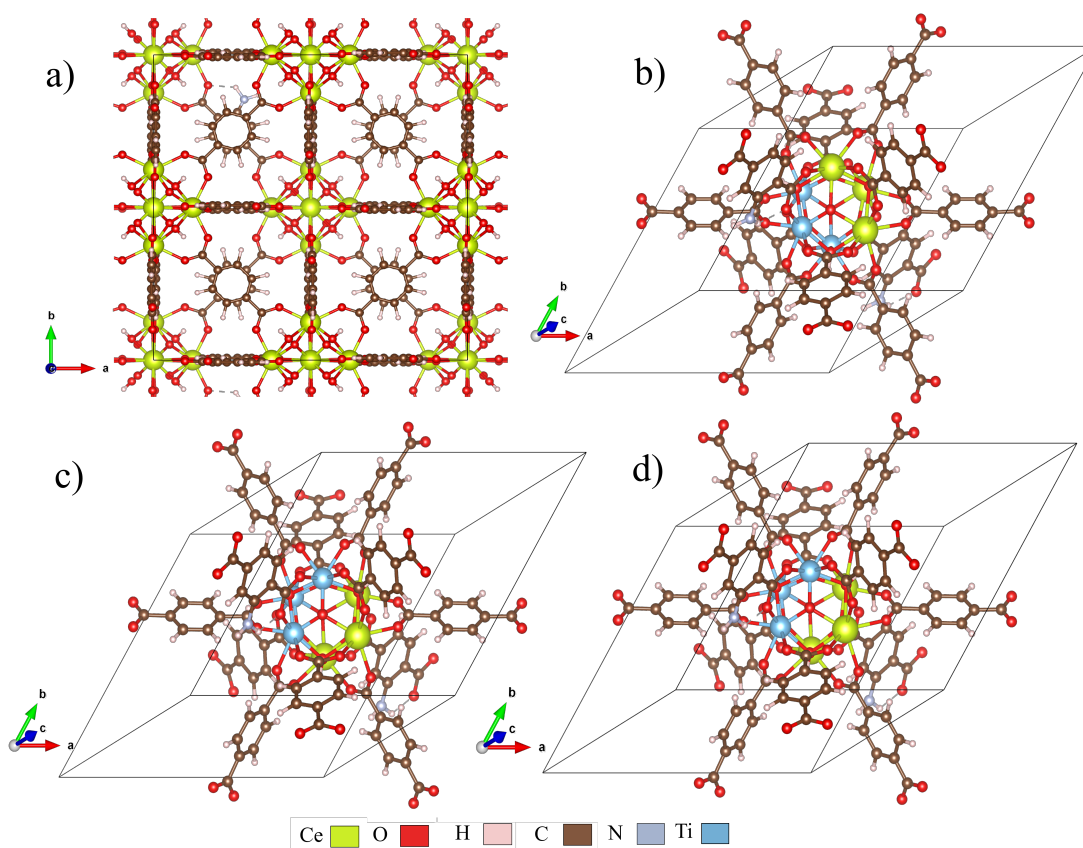


Figure 4.12: Unit cells of a) Ce-UiO-66-X, b) Sym160-X, c) Sym8-X, and d) Sym1-X structures with amine functionalization after relaxation using the r^2 SCAN+rVV10 functional (X in their names refers to the amine group NH_2).

also incorporated experimental data reported by Melillo et al.² on (Zr/Ti/Ce)UiO66 MOFs, where the valence band alignment with the vacuum, as determined by XPS, is -7.05 eV. The bandgap, determined via diffuse reflectance UV-Vis Spectra, is 3.05 eV, resulting in a conduction band alignment with the vacuum of -3.95 eV. Similar to most of the computed structures, this material permits only $\text{H}_2\text{O}/\text{O}_2$ reactions.

Fig.4.16 displays the redox potential of the CO_2 reduction reaction and its various products, indicated by dotted lines. A zoom is performed between -3.5 to -4.5 to better visualize the different CO_2 reactions. Our comparison of redox reactions using the band edge positions revealed that only the Ti-UiO-66 structure allows CO_2 reactions within a redox potential range of -3.80 to -4.03 eV, while the other eight computed structures do not. In the case of the experimental structure by Melillo et al., the only reaction allowed is CO_2/CH_4 . Interestingly, despite computational studies suggesting Ce-UiO-66 MOFs are suitable for photocatalysis, Melillo's said that mixed metal nodes in UiO-66,

particularly (Zr/Ti/Ce)UiO66, are more efficient².

Table 4.5: Computed and reported free energy change per electron (ΔG) in electronvolts (eV) for selected reactions by Wu et al.⁵. Calculations were conducted under standard conditions of pH=7 and room temperature (298.15K).

Reaction	ΔG (eV)
H ⁺ /H ₂	-3.87
H ₂ O/O ₂	-5.09
CO ₂ /CO	-3.76
CO ₂ /CH ₄	-4.03
CO ₂ /CH ₃ OH	-3.88
CO ₂ /HCHO	-3.80
CO ₂ /HCOOH	-3.62
CO ₂ /C ₂ CH ₄	-3.93
CO ₂ /C ₂ H ₅ OH	-3.95

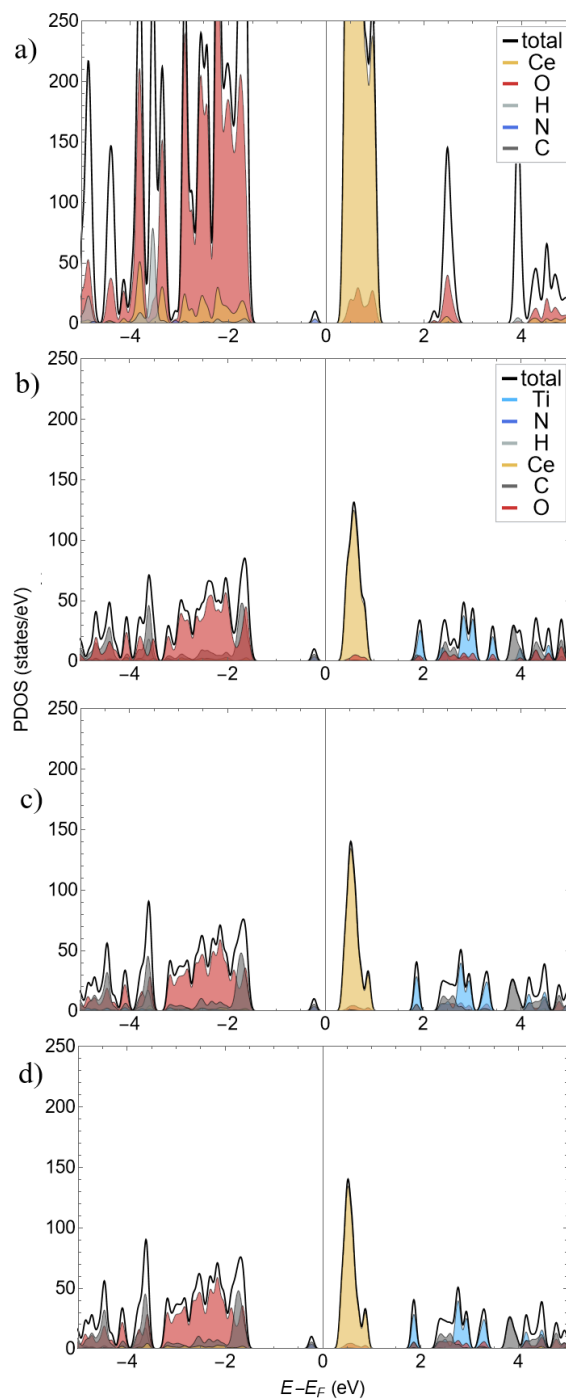


Figure 4.13: (PDOS) computed using the r^2 SCAN+rVV10/HSE06 functional for a) Ce-Uio-66-X, b) Sym160-X, c) Sym8-X and c) Sym1-X. The valence band is shifted compared to the structures without defects due to nitrogen; the atoms with the greatest contribution correspond to C, O, and H, while in the conduction band, there is a greater contribution from metal ions. The Fermi level was aligned to 0 eV, and the bandgap values are listed in Table 4.4 (X in their names refers to the amine group NH_2).

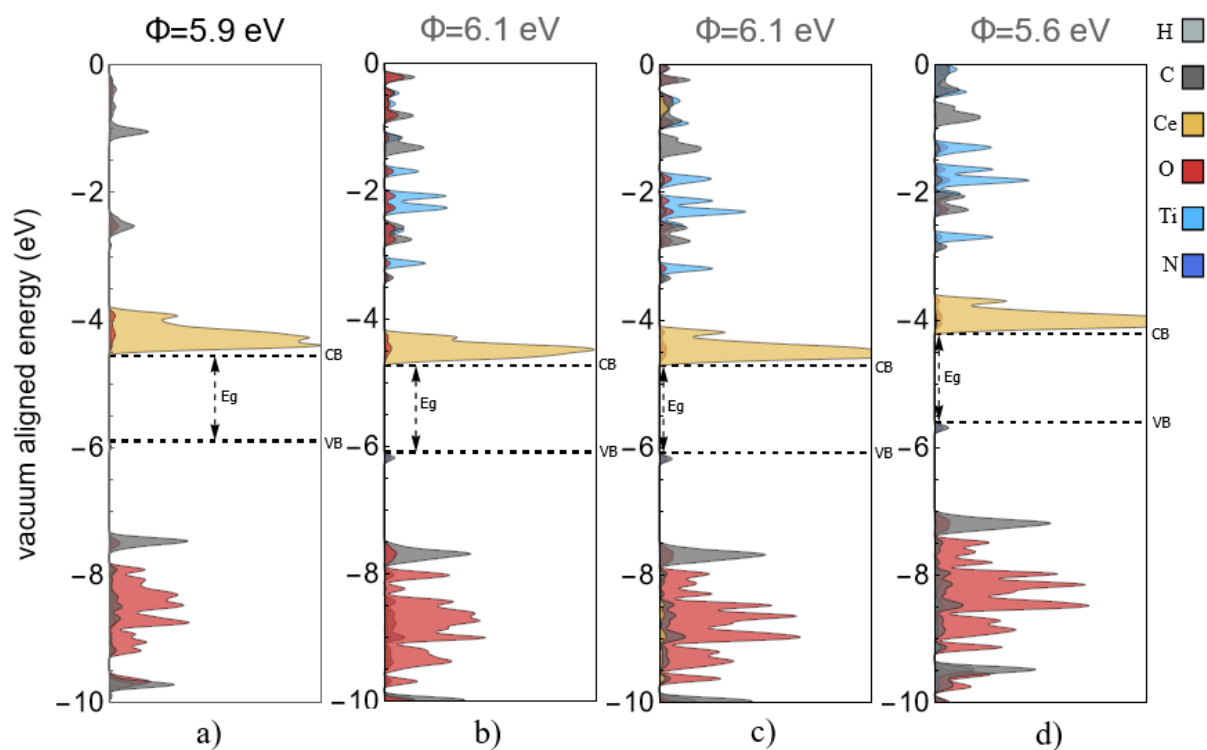


Figure 4.14: PDOS for a) Ce-UiO-66-X b) Sym160-X, b) Sym1-X, and c) Sym8-X configurations calculated using $r^2\text{SCAN}+r\text{VV10}/\text{HSE06}$ functionals, where X in their names refers to an amine group NH_2 . In all cases, the highest occupied crystal orbital corresponds to the d orbital of N, while the lowest unoccupied orbital corresponds to the f orbital of cerium. The band gap (E_g) and band edge positions are aligned with respect to the vacuum level.

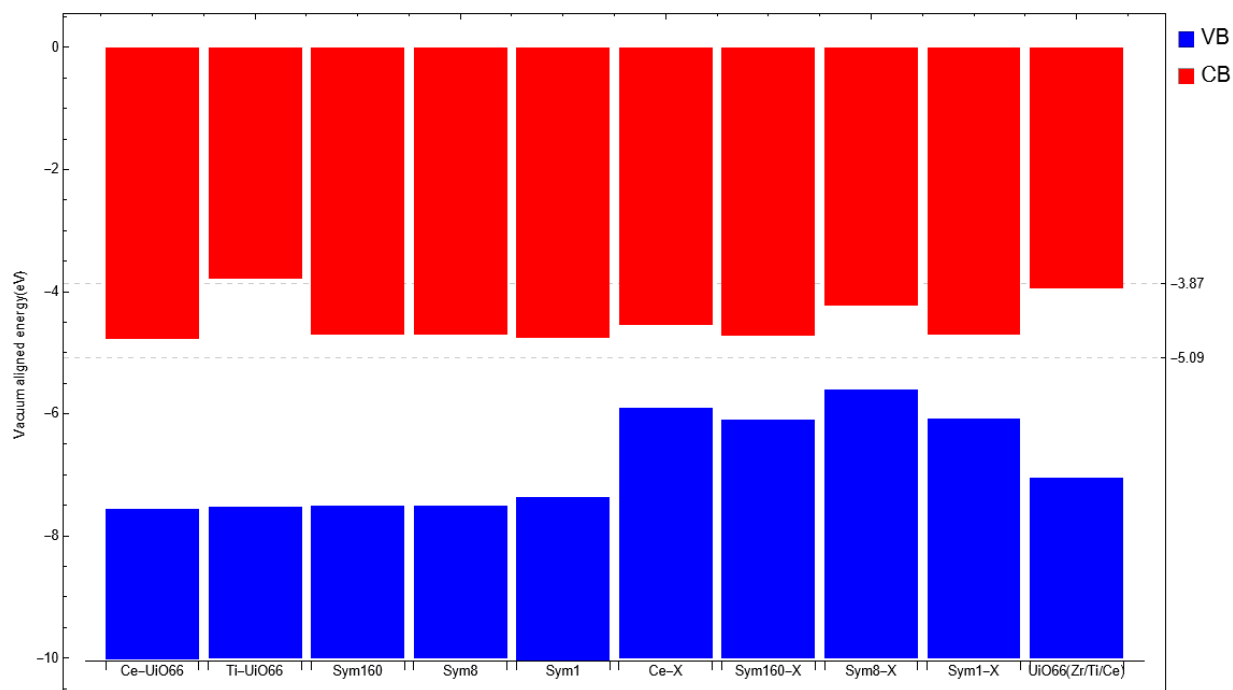


Figure 4.15: a) Absolute band edge positions for all computed structures and experimental (Zr/Ti/Ce)UiO-66 reported by Melillo et al.². The X in the names of MOFs refers to an amine group NH_2 . Upon initial inspection, it is evident that both computed and experimental structures facilitate H_2O/O_2 reactions. However, only the computed Ti MOF are suitable for H^+/H_2 reactions.

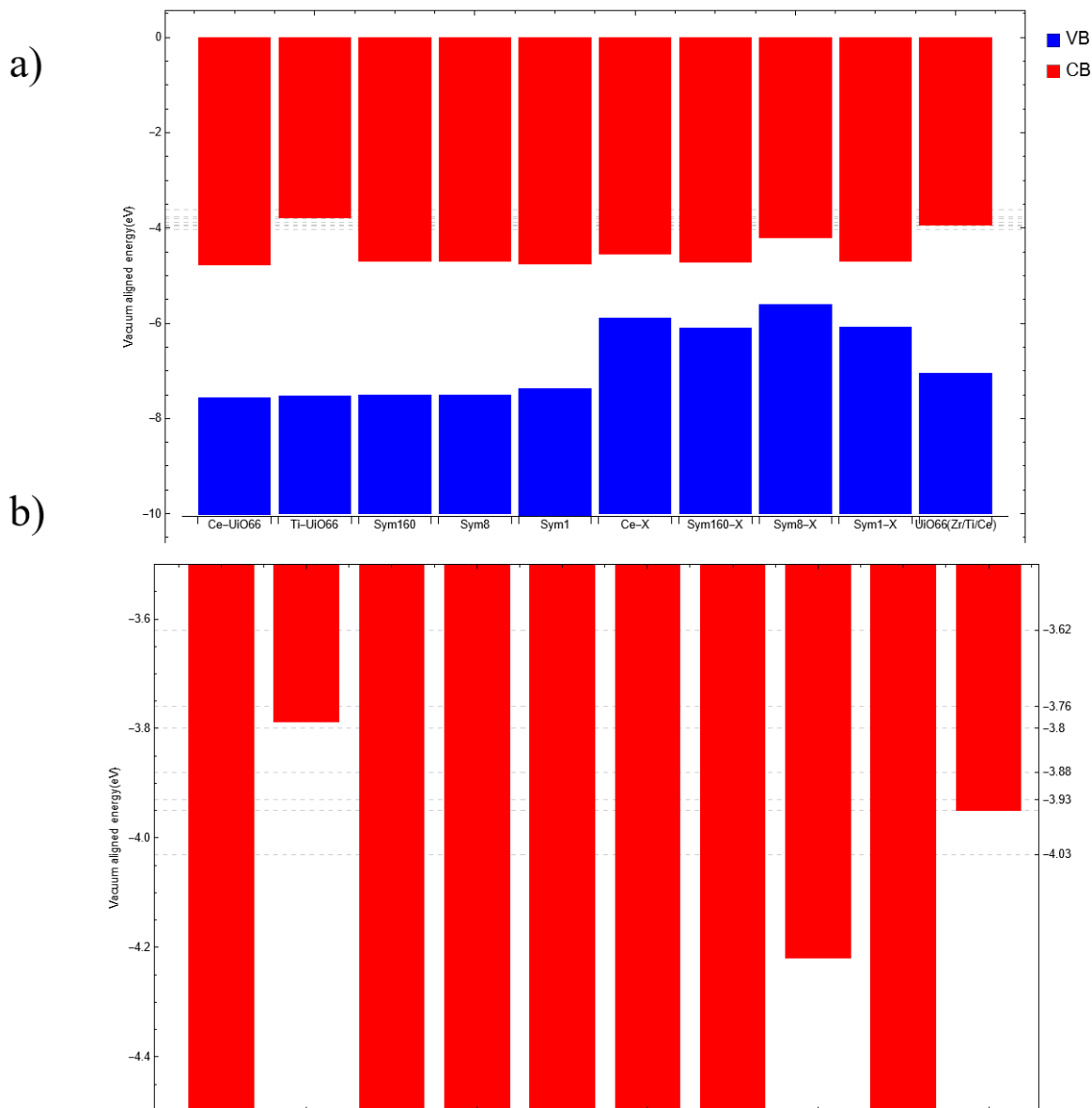


Figure 4.16: a) Absolute positions of the band edges for all computed structures and an experimental (Zr/Ti/Ce)Uio-66 reported structure by Melillo et al.² are presented. The X in the names of MOFs refers to an amine and dashed lines represent energy levels corresponding to redox potentials for various CO₂ reduction reactions. b) A zoomed-in view of the energy range relevant to CO₂ reduction reactions where is shown that (Zr/Ti/Ce)Uio-66 experimental structure that will allow CO₂/CH₄ reaction while the computed Ti-structure allowed different CO₂ reactions.

Chapter 5

Conclusions & Outlook

We focused our study on the UiO-66 MOF due to its reported ease of lab-scale synthesis, high surface area and porosity, chemical stability, and the flexibility offered by MOFs to modify material species while preserving their properties. Consequently, calculations were conducted on the UiO-66 organometallic framework, with variations introduced to the metal node and linker functionalization, resulting in nine distinct structures. Electronic properties were investigated using VASP, employing cutoff energies of 950 eV for Ti-MOF and 1050 eV for all other systems. A comparative analysis of different functionals was carried out to closely align electronic structures with experimental values. Despite accurately predicting crystallographic data, hybrid functional improved electronic structure predictions but demanded higher computational costs. Consequently, the r^2 SCAN+rVV10 functional was employed for structure optimization, followed by HSE06 for energy corrections.

By analyzing the partial density of states, initially, the Ce and Ti structures exhibited bandgaps and vacuum potentials of $E_g = 2.78$ eV, $E_g = 3.73$ eV, $\Phi = 7.60$ eV, and $\Phi = 7.50$ eV, respectively. When mixing metals, three distinct structures emerged with symmetries 160:R3m, 8:Cm, and 1:P1, featuring corresponding bandgaps of 2.70 eV, 2.70 eV, and 2.61 eV and reduced work functions ranging from $\Phi = 7.40$ eV to $\Phi = 7.50$ eV.

In our pursuit of developing long-lifetime photocatalytic materials, we have primarily focused on the ligand-to-metal charge transfer (LMCT) properties observed in Ce-MOF and mixed metal structures. These properties extend the lifetimes due to spatial separations between the highest occupied and lowest unoccupied states, preventing rapid recombination. Defects were introduced within these structures, resulting in reduced work functions of $\Phi = 5.90 - 6.10$ eV and bandgaps of $E_g = 1.34 - 1.38$ eV, falling within the visible range. Notable in the partial density of states, this amine functionalization of the linker results in shifting the valence band with the highest occupied crystal orbital corresponding to nitrogen. All structures supported the H_2O/O_2 reaction for water splitting by aligning band edge positions with vacuum energy levels and redox potentials. However, only the Ti-UiO-66 system allowed not only the H_2O/O_2 but also the H^+/H_2 reactions and various CO_2 reactions within an energy range of -3.80 eV to -4.03 eV (i.e. CO_2/CH_4 , CO_2/CH_3OH , $CO_2/HCHO$, CO_2/C_2CH_4 , CO_2/C_5H_5OH). Similar case for the (Zr/Ti/Ce) structure analyzed experimentally allowing only the H_2O/O_2 and CO_2/CH_4 reactions.

Finally, the Ce-UiO-66-NH₂ structure is a promising candidate for water-splitting photocatalysis due to its

visible-range bandgaps and lower energy requirements for charge transfer. On the other hand, Ti-Uio-66 MOF offers potential for both water splitting and CO₂ reduction, but their charge transfer capabilities are limited. Therefore, future the research will explore the possibility of shifting the conduction band by varying the metal proportions in the node and functionalizing the linker with I and Br halogens.

Appendix A

Initial Inputs

```
1 SYSTEM = ceuio66
2 ##### ELECTRONIC RX #####
3 #ISMear = -5 ! -5 insulators&final energy,1 rx in metals,0 if num kp less than 4
4 #SIGMA = 0.2 ! 0.2 when ismear=1 or 0.05 when ismear=0
5 ISMEAR=0 ; SIGMA=0.05 ! use this for accurate DOS insulators
6 LREAL = auto
7 PREC = Accurate
8 ENCUT = 1050
9 ALGO = F !N more accurate, F fast, VF fastest, D damped, A precondition (D,A for HF)
10 #LORBIT = 11 !use this for PDOS
11 AMIN = 0.01 !use when no electronic convergency
12 #----- FOR CONVERGENCY PROBLEMS IN SURFACES -----
13 #NELMDL=-8
14 #LMAXMIX=4
15 #KSPACING=0.2513275
16 ##### FUNCTIONAL #####
17 #GGA = PS ! AM for AM05, PS for PBEsol
18 METAGGA = R2SCAN
19 LUSE$_$VDW = .TRUE.
20 BPARAM = 15.7
21 CPARAM = 0.0093
22 LMIXTAU = T
23 LASPH = .TRUE.
24 LMAXMIX=6
25 ##### DIPOLE CORRECTIONS #####
26 #IDIPOL=3 ! 3 is for surfaces
27 #LDIPOL=.TRUE.
28 ##### CHARGE & WAVEFUNCTIONS #####
29 LCHARG= F
30 #LWAVE= F
31 #ICHARG = 12
```

```

32 #LAECHG= T ! use this for bader analysis
33 ##### FOR DOS #####
34 #ICHARG=11
35 #LWAVE = F
36 #LCHARG = F
37 #LMAXMIX = 4
38 #NEDOS=3001 !301 default
39 EMIN=-12.6 !min energy value
40 EMAX=7.5 ! max energy value
41 ##### FOR BAND STRUCTURE #####
42 #ICHARG=11
43 #LWAVE = F
44 #LCHARG = F
45 #NBANDS=?? ! how many bands?
46 ##### FOR bskan generate WAVCAR #####
47 #STM= zmin zamx 0.052918 -60 eval1 eval2 Ef ! eval1/2 with respect Ef
48 ##### FOR BAND DECOMPOSED CHARGE DENSITY #####
49 #LPARD= T
50 #EINT= emin? emax?
51 #NBMOD= -2
52 ##### FOR WORK FUNCTION #####
53 #LVTOT = T
54 #LVHAR = T
55 ##### RELAXATION #####
56 #NELMIN=4
57 #MAXMIX=30
58 #IBRION=2 !1 Newton, 2 CG
59 #ISIF=2 !2 ions only 3 ions+shape+lattice 4 ions+shape
60 ##POTIM=0.7
61 #NSW=120
62 #EDIFFG= -0.02
63 ##### PARALLELISATION STAMPEDE #####
64 #LPLANE=T !T if num nodes << NGX,NGY,NGZ
65 NCORE=24 ! this is total cores per node
66 NSIM=4 ! use 1 in supercomputers

```

Listing A.1: INCAR file with tags in capital letters. The # symbol is used for commented tags. Refer to VASPWiki for detailed explanation of each tag.

```

1 ceuio66      # System label
2 0           # Automatic generation
3 Gamma      # Generation scheme
4 1 1 1
5 0 0 0      # Shift

```

Listing A.2: KPOINTS file. The # symbol is used to indicate commented text.

```

1 H C 0 Ce : ceuio66 PC

```

```

2 1.02982442800439
3 14.7732999999990859 -0.0000000000000000 0.0000000000000000
4 7.3866499999995323 12.7940530977388924 0.0000000000000000
5 7.3866500000014836 4.2646843659423794 12.0623489390215326
6 H C O Ce
7 28 48 32 6
8 Selective dynamics
9 Direct
10 0.6282282565981987 0.9298061503940360 0.3480408906044943 T T T
11 0.9298061503940360 0.6282282565982058 0.0939247024032781 T T T
12 0.3480408906044943 0.0939247024032781 0.6282282565982058 T T T

```

Listing A.3: POSCAR file example from Ce-UiO-66 structure. Only first 13 lines are shown.

```

1 PAW_PBE H_GW 21Apr2008
2 1.0000000000000000
3 parameters from PSCTR are:
4 SHA256 = cecc88617a3d1ece9865646f5d462fc0f44fd1f68d6f2eb08f18a2e421902afb H_GW/POTCAR
5 COPYR = (c) Copyright 21Apr2008 Georg Kresse
6 COPYR = This file is part of the software VASP. Any use, copying, and all other rights are
7 regulated by the VASP license agreement.
8 COPYR = If you do not have a valid VASP license, you may not use, copy or distribute this
9 file.
10 VRHFIN =H: ultrasoft test
11 LEXCH = PE
12 EATOM = 12.4884 eV, 0.9179 Ry
13
14 TITEL = PAW_PBE H_GW 21Apr2008
15 LULTRA = F use ultrasoft PP ?
16 IUNSCR = 0 unscreen: 0-lin 1-nonlin 2-no
17 RPACOR = 0.000 partial core radius
18 POMASS = 1.000; ZVAL = 1.000 mass and valenz
19 RCORE = 1.100 outmost cutoff radius
20 RWIGS = 1.100; RWIGS = 0.582 wigner-seitz radius (au A)
21 ENMAX = 300.000; ENMIN = 250.000 eV
22 RCLOC = 0.701 cutoff for local pot
23 LCOR = T correct aug charges
24 LPAW = T paw PP
25 EAUG = 500.000
26 RMAX = 1.123 core radius for proj-oper
27 RAUG = 1.200 factor for augmentation sphere
28 RDEP = 1.112 radius for radial grids
29 RDEPT = 1.100 core radius for aug-charge

```

Listing A.4: POTCAR file example form Ce-UiO-66 structure. Only first 27 lines are shown.

Appendix B

Detailed Orbital-resolved Partial Density of States

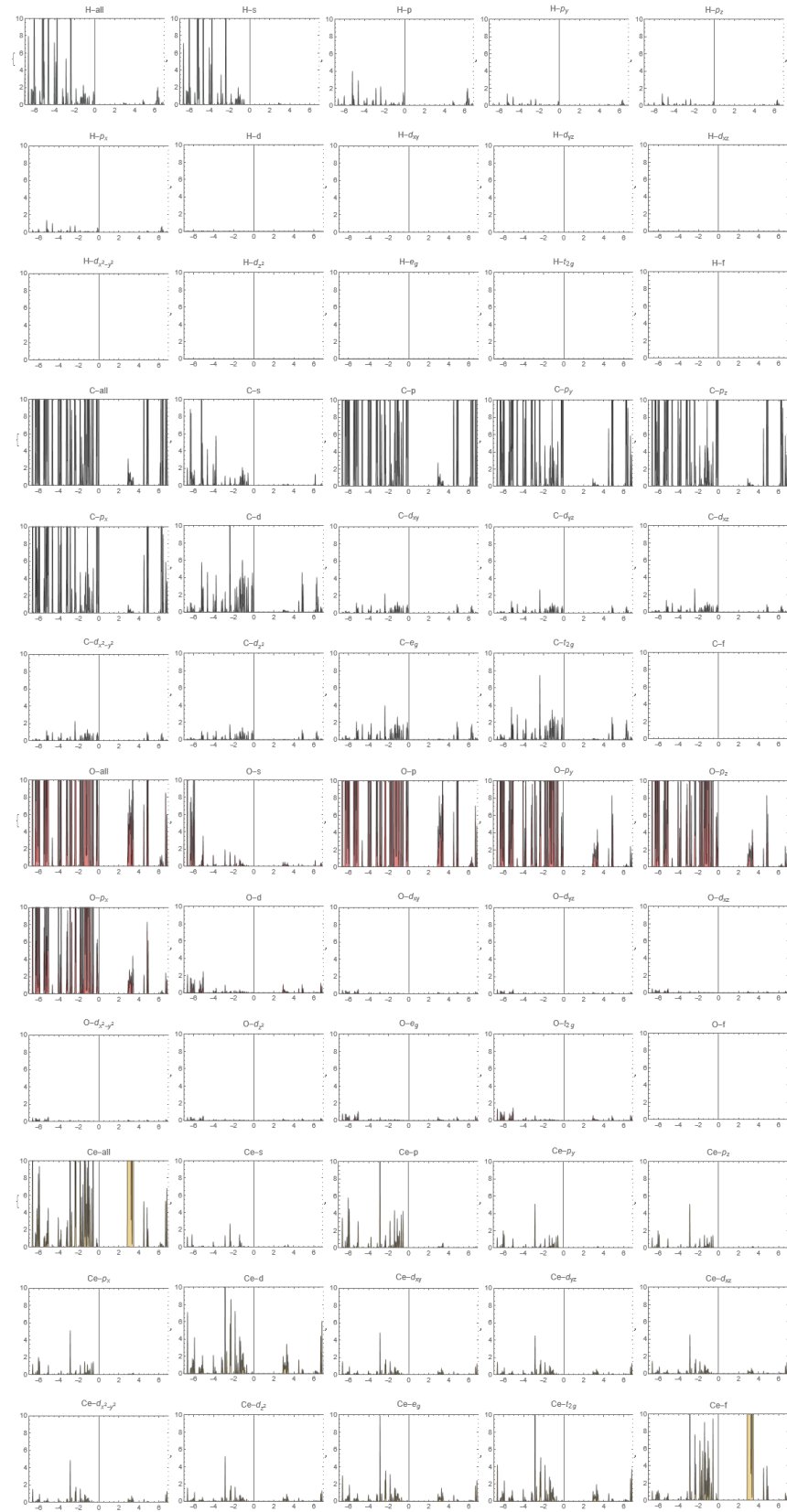


Figure B.1: Detailed orbital resolved PDOS for Ce-UiO-66 structure.

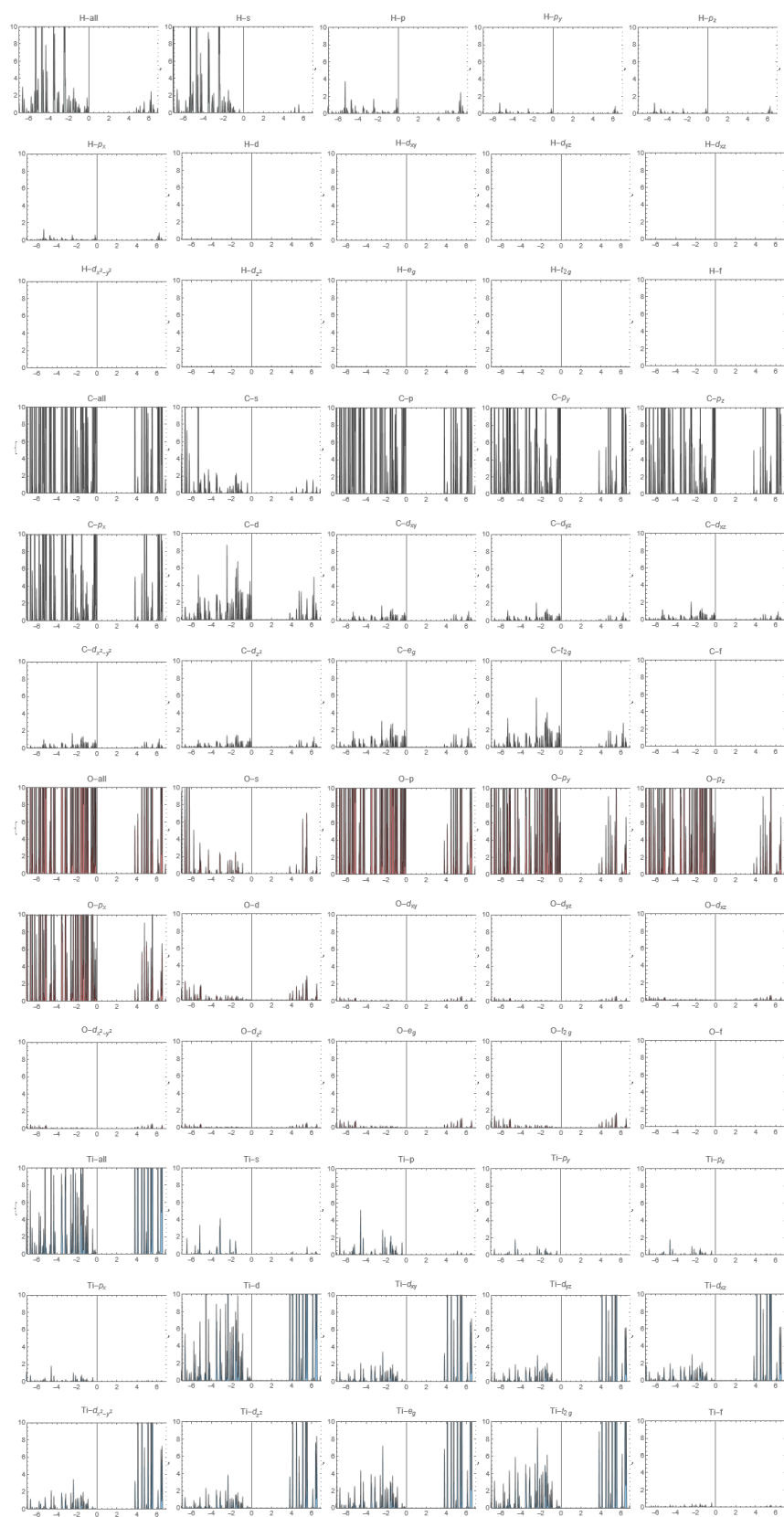


Figure B.2: Detailed orbital resolved PDOS for Ti-UiO-66 structure.

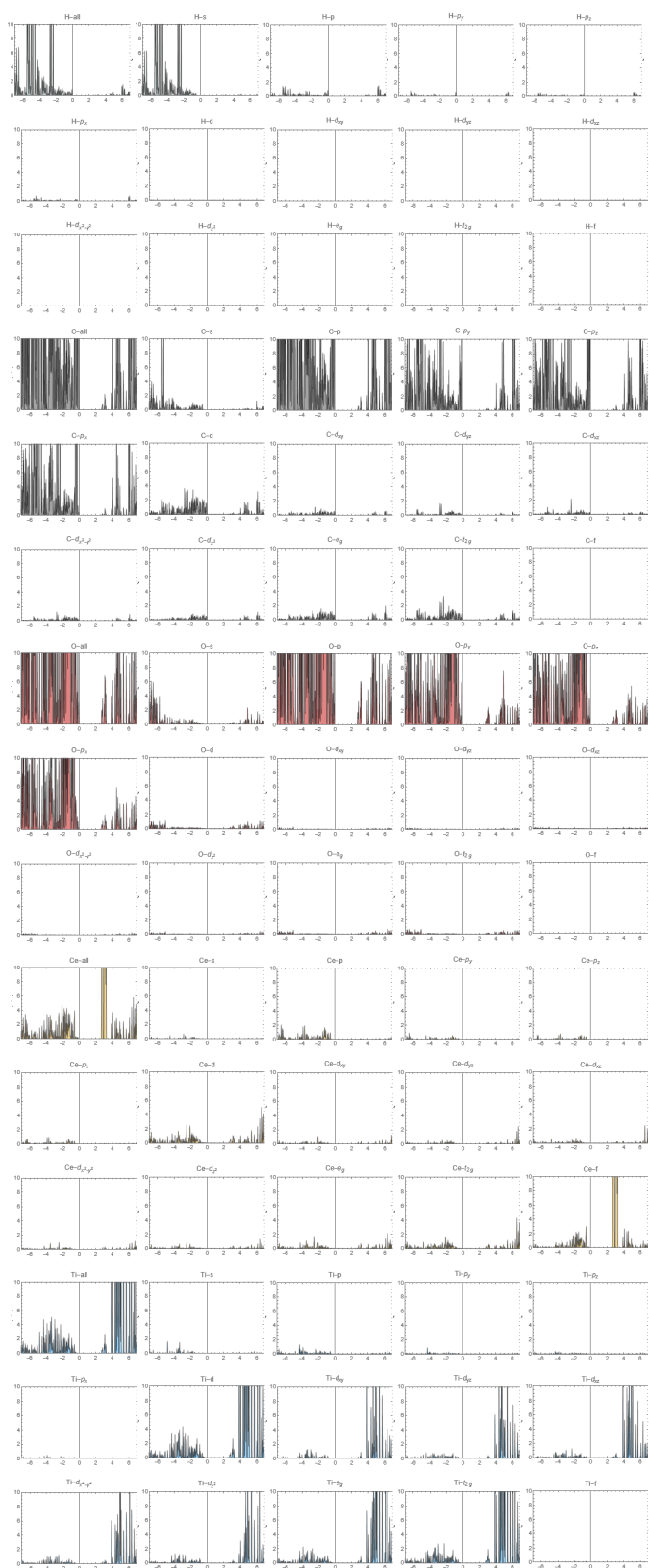
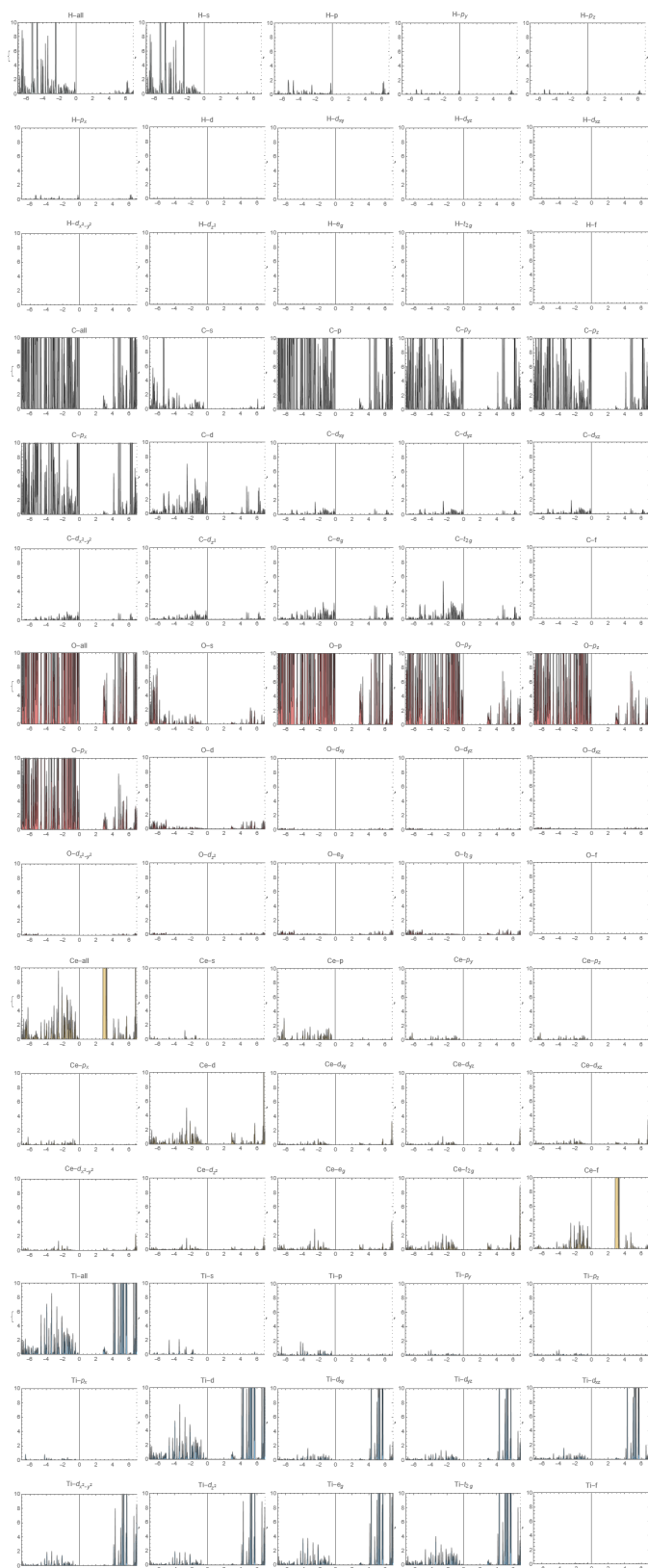
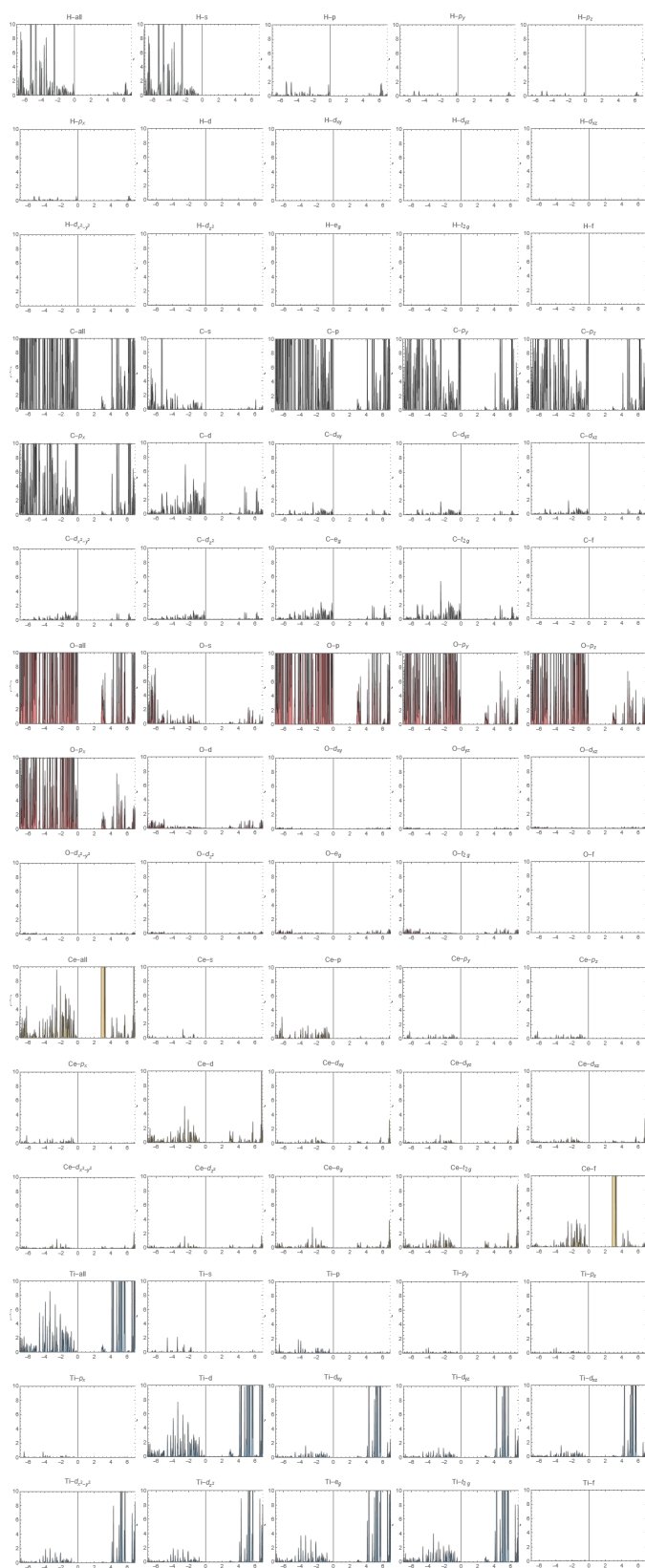


Figure B.3: Detailed orbital resolved PDOS for $\text{Ti}_3\text{Ce}_3(\text{Sym}1)\text{-UiO-66}$

Figure B.4: Detailed orbital resolved PDOS for $\text{Ti}_3\text{Ce}_3(\text{Sym}160)\text{-UiO-66}$

Figure B.5: Detailed orbital resolved PDOS for $\text{Ti}_3\text{Ce}_3(\text{Sym}8)\text{-UiO-66}$

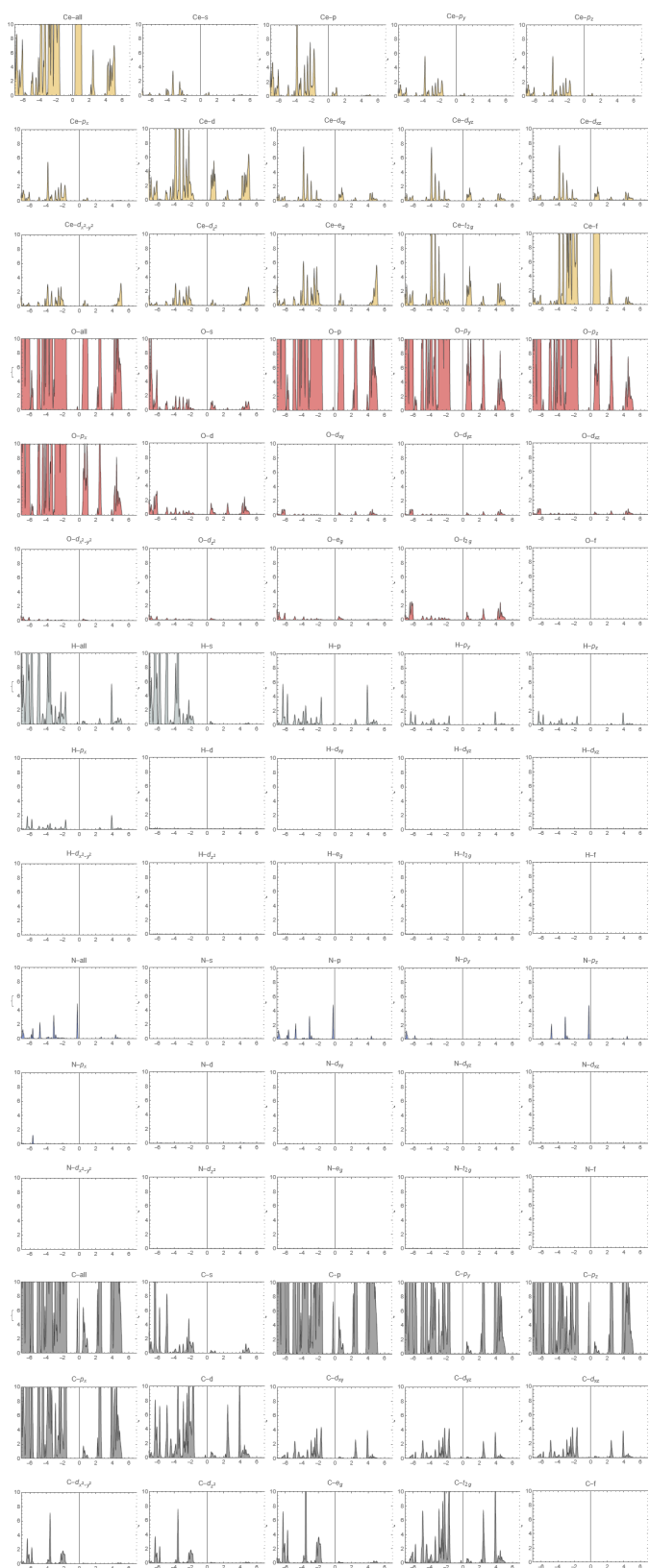
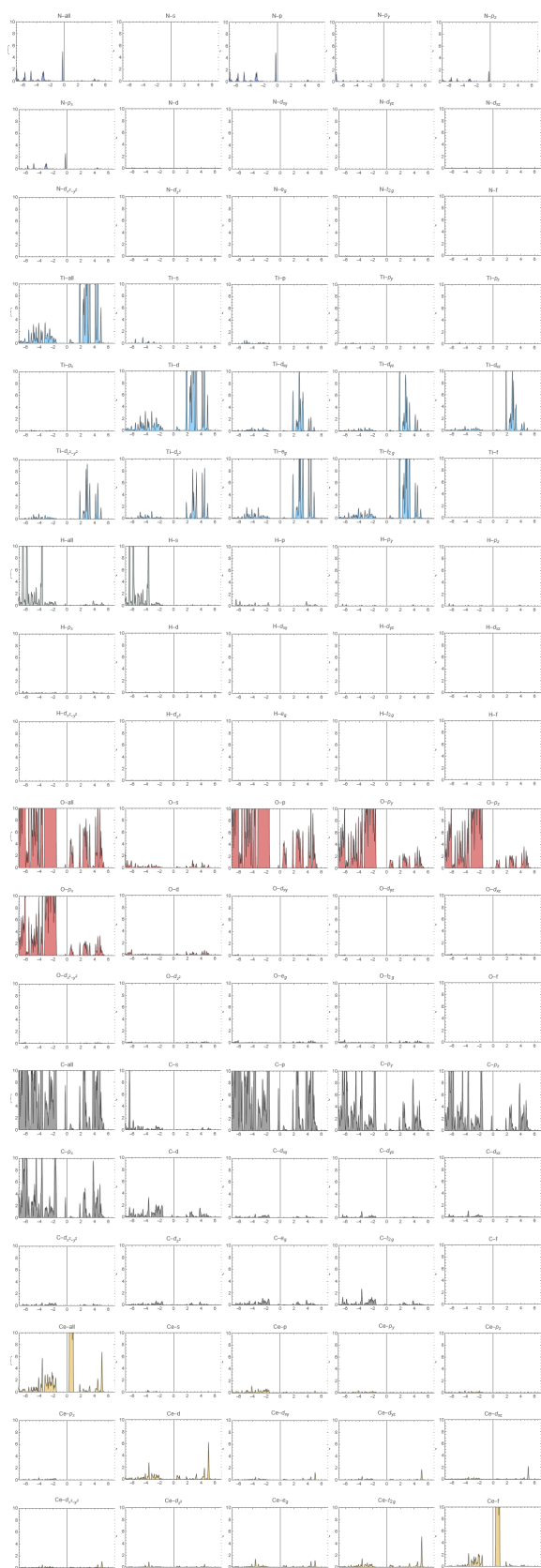
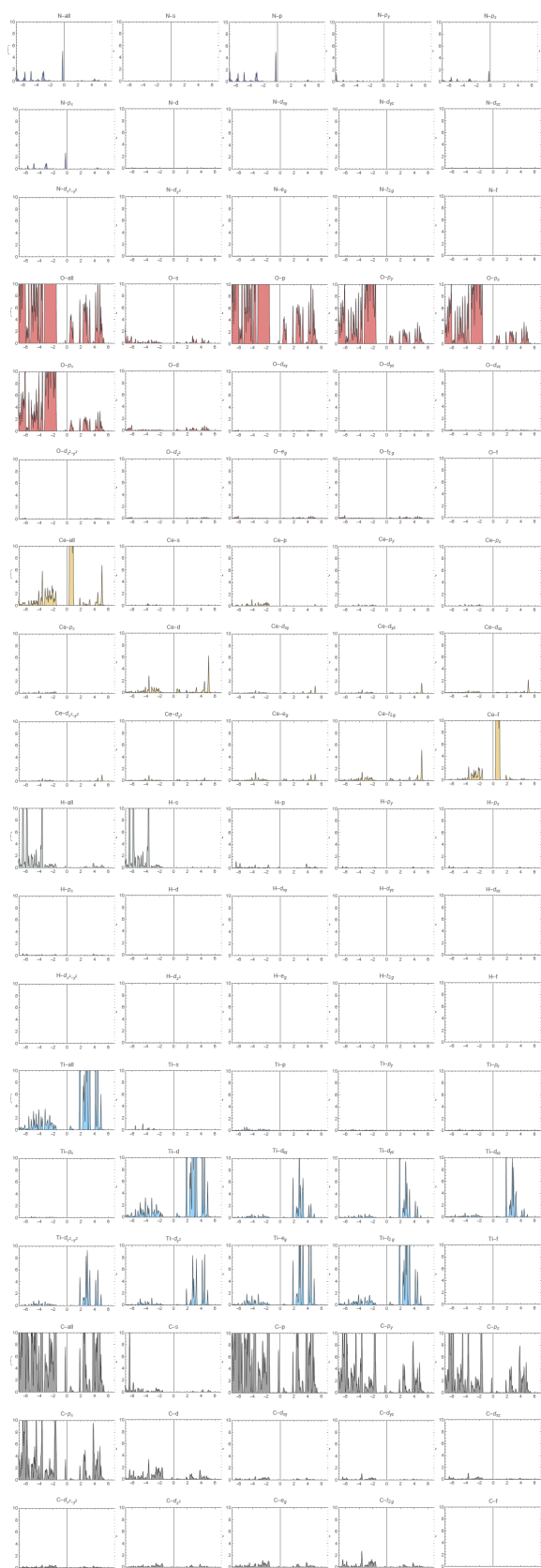
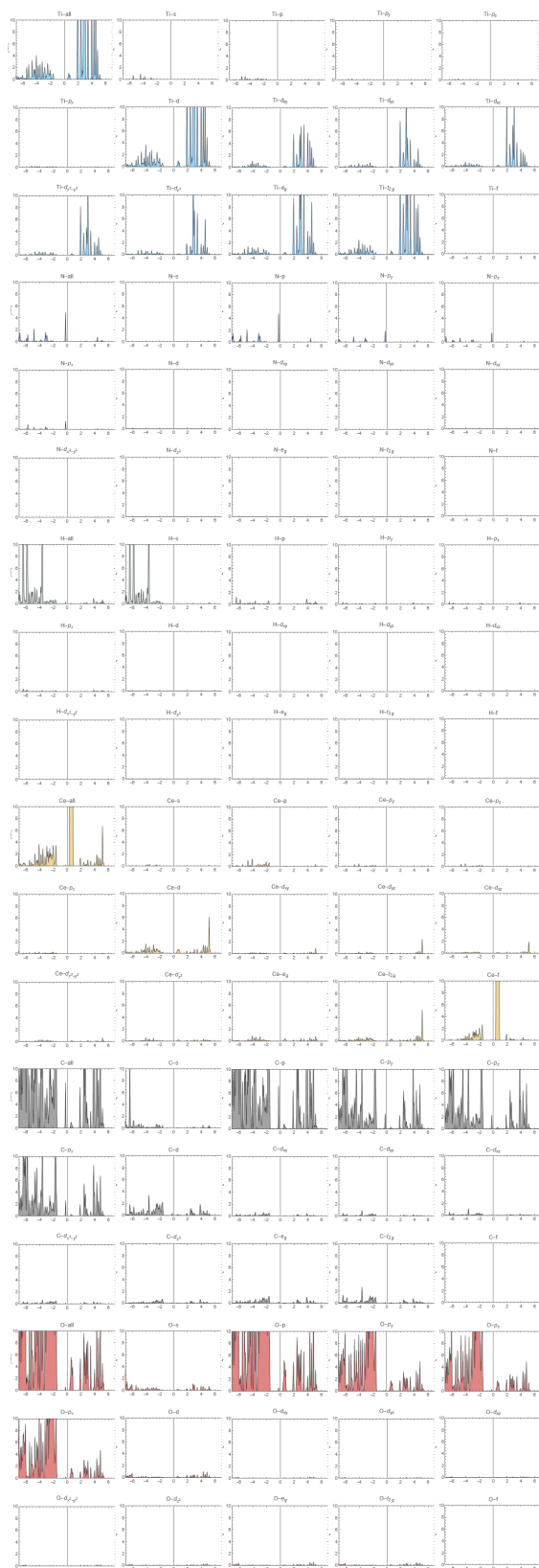


Figure B.6: Detailed orbital resolved PDOS for Ce-UiO-66-NH₂ structure.

Figure B.7: Detailed orbital resolved PDOS for $\text{Ti}_3\text{Ce}_3(\text{Sym}1)\text{-UiO-66-NH}_2$

Figure B.8: Detailed orbital resolved PDOS for $\text{Ti}_3\text{Ce}_3(\text{Sym}8)\text{-UiO-66-NH}_2$

Figure B.9: Detailed orbital resolved PDOS for $\text{Ti}_3\text{Ce}_3(\text{Sym}160)\text{-UiO-66-NH}_2$

Appendix C

Detailed Partial Density of States

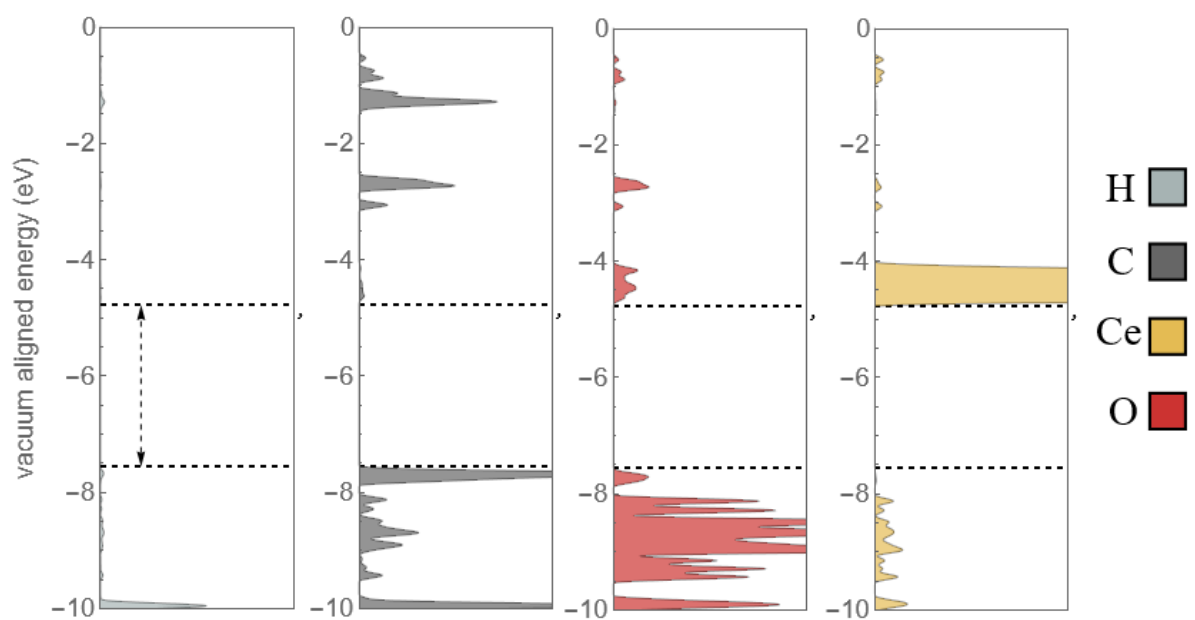


Figure C.1: Detailed PDOS for Ce-UiO-66

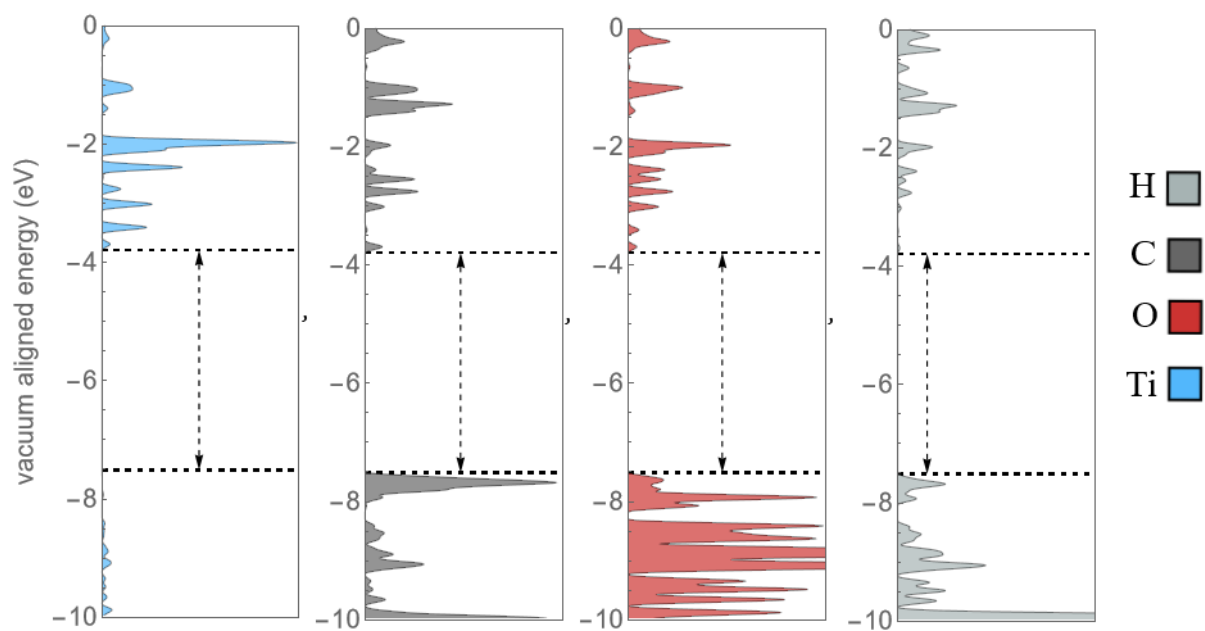
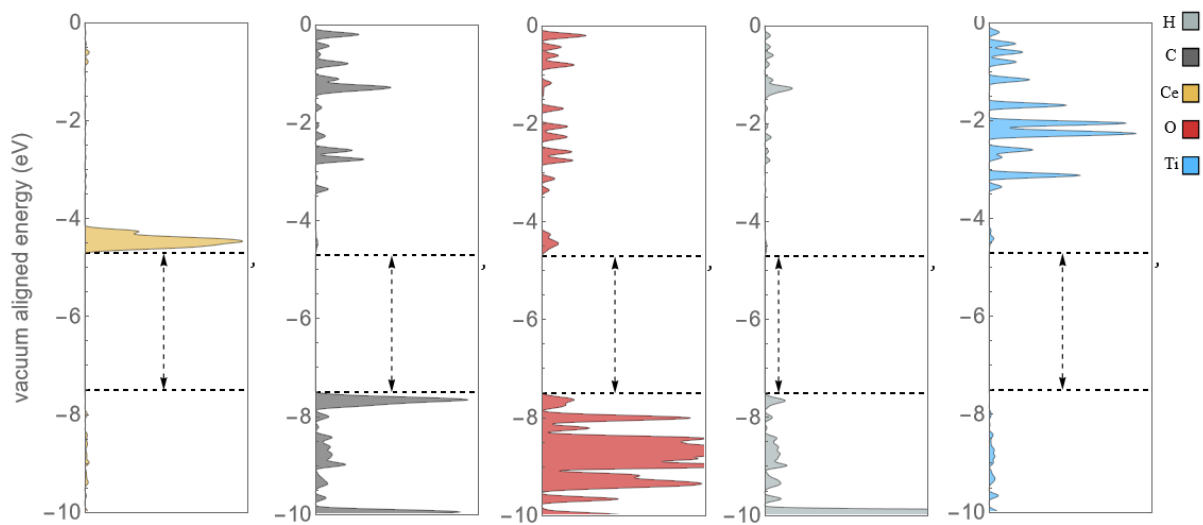
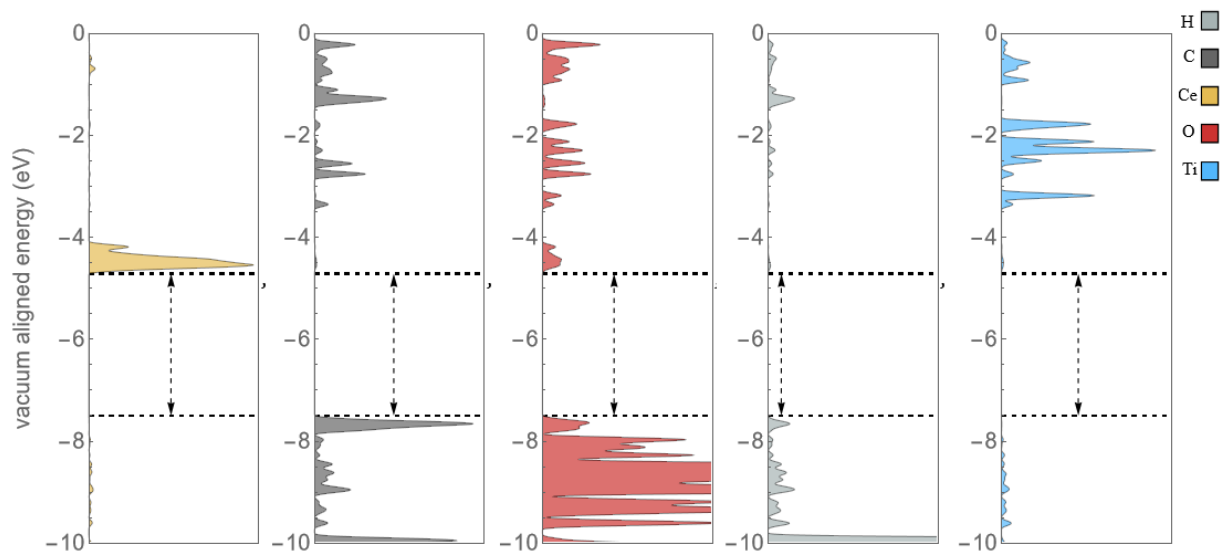
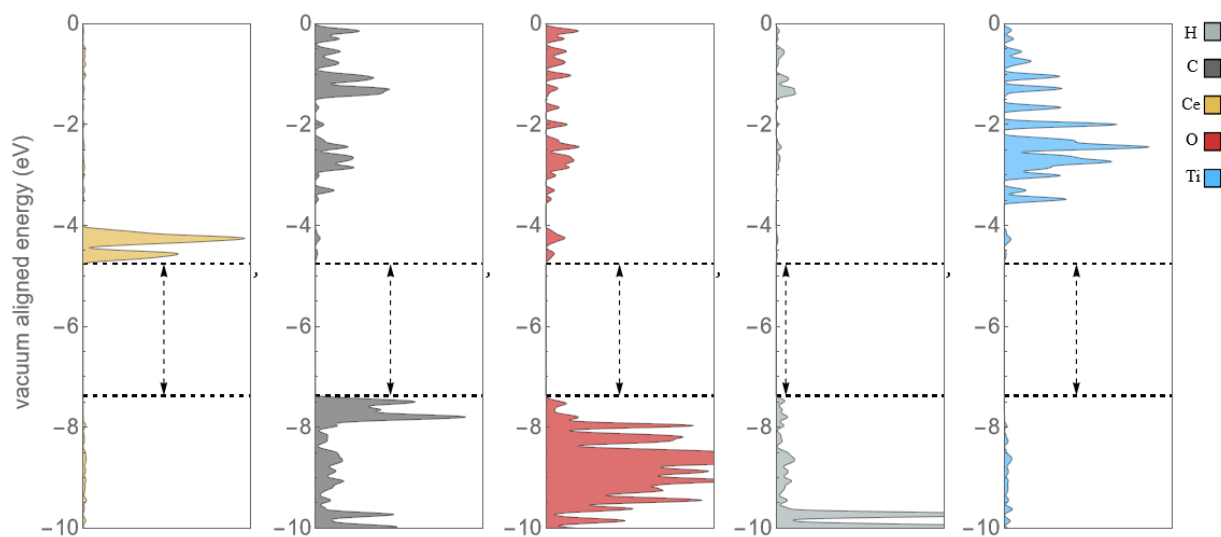
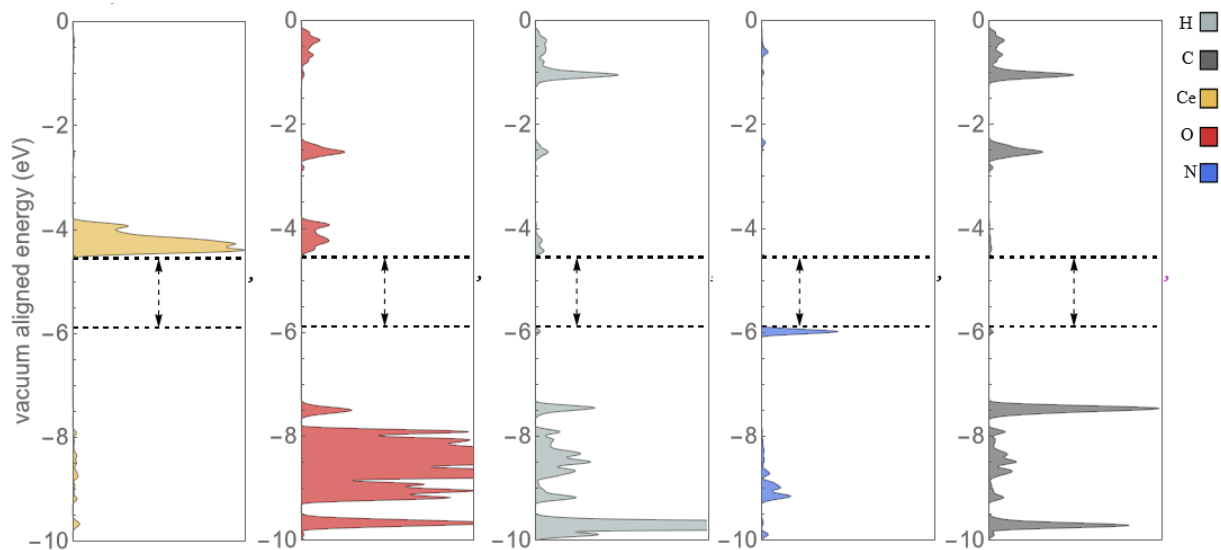
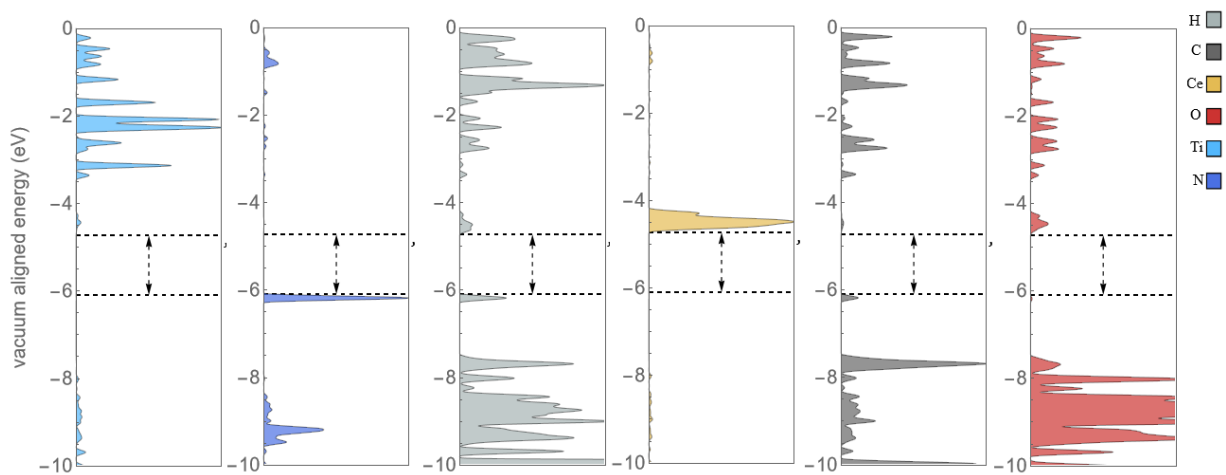
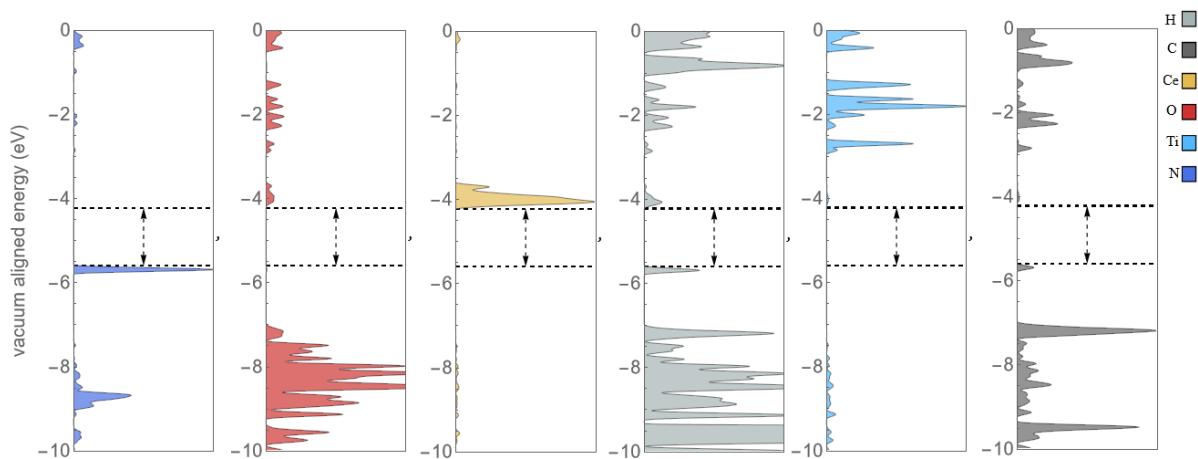
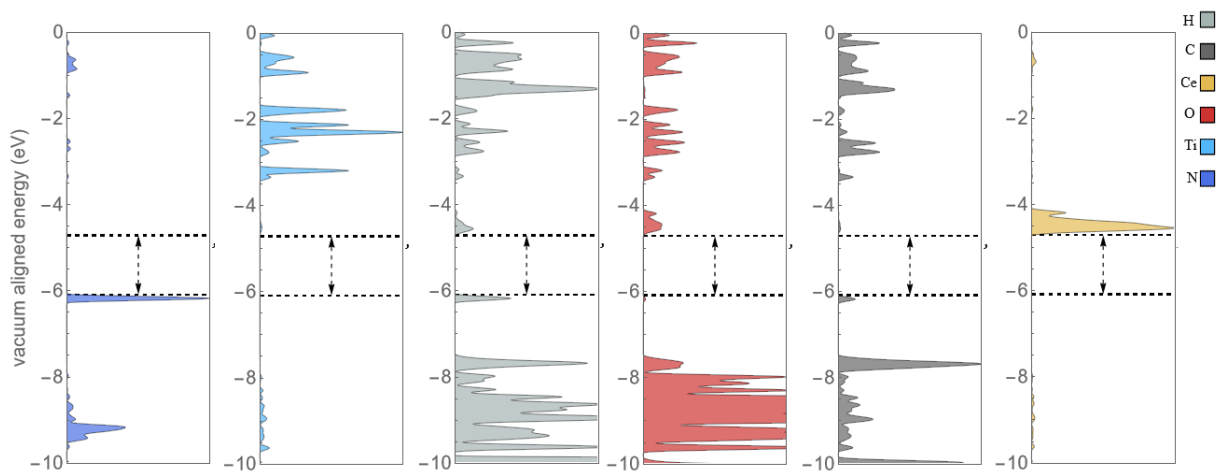


Figure C.2: Detailed PDOS for Ti-UiO-66

Figure C.3: Detailed PDOS for $\text{Ti}_3\text{Ce}_3(\text{Sym}160)\text{-UiO-66}$

Figure C.4: Detailed PDOS for $\text{Ti}_3\text{Ce}_3(\text{Sym}8)\text{-UiO-66}$ Figure C.5: Detailed PDOS for $\text{Ti}_3\text{Ce}_3(\text{Sym}1)\text{-UiO-66}$

Figure C.6: Detailed PDOS for Ce-UiO-66-NH₂Figure C.7: Detailed PDOS for Ti₃Ce₃(Sym160)-UiO-66-NH₂

Figure C.8: Detailed PDOS for $\text{Ti}_3\text{Ce}_3(\text{Sym}8)\text{-UiO-66-NH}_2$ Figure C.9: Detailed PDOS for $\text{Ti}_3\text{Ce}_3(\text{Sym}1)\text{-UiO-66-NH}_2$

Bibliography

- [1] Martin, R. M.; Reining, L.; Ceperley, D. M. *Interacting electrons*; Cambridge University Press, 2016.
- [2] Melillo, A.; Cabrero-Antonino, M.; Navalon, S.; Alvaro, M.; Ferrer, B.; Garcia, H. Enhancing visible-light photocatalytic activity for overall water splitting in UiO-66 by controlling metal node composition. *Applied Catalysis B: Environmental* **2020**, *278*, 119345.
- [3] Perdew, J. P.; Schmidt, K. Jacob's ladder of density functional approximations for the exchange-correlation energy. **2001**, *577*, 1–20.
- [4] Lammert, M.; Wharmby, M. T.; Smolders, S.; Bueken, B.; Lieb, A.; Lomachenko, K. A.; De Vos, D.; Stock, N. Cerium-based metal organic frameworks with UiO-66 architecture: synthesis, properties and redox catalytic activity. *Chemical Communications* **2015**, *51*, 12578–12581.
- [5] Wu, X.-P.; Gagliardi, L.; Truhlar, D. G. Cerium metal–organic framework for photocatalysis. *Journal of the American Chemical Society* **2018**, *140*, 7904–7912.
- [6] Khataee, A.; Kasiri, M. B. Photocatalytic degradation of organic dyes in the presence of nanostructured titanium dioxide: Influence of the chemical structure of dyes. *Journal of Molecular Catalysis A: Chemical* **2010**, *328*, 8–26.
- [7] Dhakshinamoorthy, A.; Asiri, A. M.; Garcia, H. Metal–organic framework (MOF) compounds: photocatalysts for redox reactions and solar fuel production. *Angewandte Chemie International Edition* **2016**, *55*, 5414–5445.
- [8] Yaghi, O. M.; Kalmutzki, M. J.; Diercks, C. S. *Introduction to reticular chemistry: metal-organic frameworks and covalent organic frameworks*; John Wiley & Sons, 2019.
- [9] Mancuso, J. L.; Mroz, A. M.; Le, K. N.; Hendon, C. H. Electronic structure modeling of metal–organic frameworks. *Chemical reviews* **2020**, *120*, 8641–8715.
- [10] Winarta, J.; Shan, B.; McIntyre, S. M.; Ye, L.; Wang, C.; Liu, J.; Mu, B. A decade of UiO-66 research: a historic review of dynamic structure, synthesis mechanisms, and characterization techniques of an archetypal metal–organic framework. *Crystal Growth & Design* **2019**, *20*, 1347–1362.

- [11] James, S. L. Metal-organic frameworks. *Chemical Society Reviews* **2003**, *32*, 276–288.
- [12] Zhang, X.; Chen, Z.; Liu, X.; Hanna, S. L.; Wang, X.; Taheri-Ledari, R.; Maleki, A.; Li, P.; Farha, O. K. A historical overview of the activation and porosity of metal–organic frameworks. *Chemical Society Reviews* **2020**, *49*, 7406–7427.
- [13] Dhakshinamoorthy, A.; Li, Z.; Garcia, H. Catalysis and photocatalysis by metal organic frameworks. *Chemical Society Reviews* **2018**, *47*, 8134–8172.
- [14] Smolders, S.; Lomachenko, K. A.; Bueken, B.; Struyf, A.; Bugaev, A. L.; Atzori, C.; Stock, N.; Lamberti, C.; Roeffaers, M. B.; De Vos, D. E. Unravelling the Redox-catalytic Behavior of Ce⁴⁺ Metal–Organic Frameworks by X-ray Absorption Spectroscopy. *ChemPhysChem* **2018**, *19*, 373–378.
- [15] Estes, S. L.; Antonio, M. R.; Soderholm, L. Tetravalent Ce in the nitrate-decorated hexanuclear cluster [Ce₆(μ_3 -O)₄(μ_3 -OH)₄]¹²⁺: a structural end point for ceria nanoparticles. *The Journal of Physical Chemistry C* **2016**, *120*, 5810–5818.
- [16] Smith, S. J.; Ladewig, B. P.; Hill, A. J.; Lau, C. H.; Hill, M. R. Post-synthetic Ti exchanged UiO-66 metal-organic frameworks that deliver exceptional gas permeability in mixed matrix membranes. *Scientific reports* **2015**, *5*, 7823.
- [17] Rego, R. M.; Sriram, G.; Ajeya, K. V.; Jung, H.-Y.; Kurkuri, M. D.; Kigga, M. Cerium based UiO-66 MOF as a multipollutant adsorbent for universal water purification. *Journal of Hazardous Materials* **2021**, *416*, 125941.
- [18] Giustino, F. *Materials modelling using density functional theory: properties and predictions*; Oxford University Press, 2014.
- [19] Hohenberg, P.; Kohn, W. Inhomogeneous electron gas. *Physical review* **1964**, *136*, B864.
- [20] Sholl, D. S.; Steckel, J. A. *Density functional theory: a practical introduction*; John Wiley & Sons, 2022.
- [21] Kohn, W.; Sham, L. J. Self-Consistent Equations Including Exchange and Correlation Effects. *Phys. Rev.* **1965**, *140*, A1133–A1138.
- [22] Sousa, S. F.; Fernandes, P. A.; Ramos, M. J. General performance of density functionals. *The Journal of Physical Chemistry A* **2007**, *111*, 10439–10452.
- [23] Perdew, J. P.; Ruzsinszky, A.; Csonka, G. I.; Vydrov, O. A.; Scuseria, G. E.; Constantin, L. A.; Zhou, X.; Burke, K. Restoring the density-gradient expansion for exchange in solids and surfaces. *Physical review letters* **2008**, *100*, 136406.
- [24] Perdew, J. P.; Ruzsinszky, A.; Csonka, G. I.; Vydrov, O. A.; Scuseria, G. E.; Constantin, L. A.; Zhou, X.; Burke, K. Erratum: Restoring the Density-Gradient Expansion for Exchange in Solids and Surfaces [Phys. Rev. Lett. 100, 136406 (2008)]. *Phys. Rev. Lett.* **2009**, *102*, 039902.

- [25] Bartók, A. P.; Yates, J. R. Regularized SCAN functional. *The Journal of chemical physics* **2019**, *150*, 161101.
- [26] Furness, J. W.; Kaplan, A. D.; Ning, J.; Perdew, J. P.; Sun, J. Accurate and numerically efficient r2SCAN meta-generalized gradient approximation. *The journal of physical chemistry letters* **2020**, *11*, 8208–8215.
- [27] Ning, J.; Kothakonda, M.; Furness, J. W.; Kaplan, A. D.; Ehlert, S.; Brandenburg, J. G.; Perdew, J. P.; Sun, J. Workhorse minimally empirical dispersion-corrected density functional with tests for weakly bound systems: r2SCAN+ rVV10. *Physical Review B* **2022**, *106*, 075422.
- [28] Furness, J. W.; Kaplan, A. D.; Ning, J.; Perdew, J. P.; Sun, J. Accurate and numerically efficient r2SCAN meta-generalized gradient approximation. *The journal of physical chemistry letters* **2020**, *11*, 8208–8215.
- [29] Peng, H.; Yang, Z.-H.; Perdew, J. P.; Sun, J. Versatile van der Waals density functional based on a meta-generalized gradient approximation. *Physical Review X* **2016**, *6*, 041005.
- [30] Vydrov, O. A.; Van Voorhis, T. Nonlocal van der Waals density functional: The simpler the better. *The Journal of chemical physics* **2010**, *133*.
- [31] Krukau, A. V.; Vydrov, O. A.; Izmaylov, A. F.; Scuseria, G. E. Influence of the exchange screening parameter on the performance of screened hybrid functionals. *The Journal of chemical physics* **2006**, *125*.
- [32] Heyd, J.; Scuseria, G. E.; Ernzerhof, M. Hybrid functionals based on a screened Coulomb potential. *The Journal of chemical physics* **2003**, *118*, 8207–8215.
- [33] Hafner, J. Ab-initio simulations of materials using VASP: Density-functional theory and beyond. *Journal of computational chemistry* **2008**, *29*, 2044–2078.
- [34] Kittel, C.; McEuen, P. *Introduction to solid state physics*; John Wiley & Sons, 2018.
- [35] Kantorovich, L. *Quantum theory of the solid state: an introduction*; Springer Science & Business Media, 2004; Vol. 136.
- [36] Snoke, D. W. *Solid state physics: Essential concepts*; Cambridge University Press, 2020.
- [37] Kubacka, A.; Fernandez-Garcia, M.; Colon, G. Advanced nanoarchitectures for solar photocatalytic applications. *Chemical reviews* **2012**, *112*, 1555–1614.
- [38] Wu, X.-P.; Gagliardi, L.; Truhlar, D. G. Metal doping in cerium metal-organic frameworks for visible-response water splitting photocatalysts. *The Journal of Chemical Physics* **2019**, *150*.
- [39] Butler, K. T.; Hendon, C. H.; Walsh, A. Electronic chemical potentials of porous metal-organic frameworks. *Journal of the American Chemical Society* **2014**, *136*, 2703–2706.
- [40] Zhu, J.; Li, P.-Z.; Guo, W.; Zhao, Y.; Zou, R. Titanium-based metal-organic frameworks for photocatalytic applications. *Coordination Chemistry Reviews* **2018**, *359*, 80–101.

- [41] Dhakshinamoorthy, A.; Li, Z.; Garcia, H. Catalysis and photocatalysis by metal organic frameworks. *Chemical Society Reviews* **2018**, *47*, 8134–8172.
- [42] Lee, J. G. *Computational materials science: an introduction*; CRC press, 2016.
- [43] Tyuterev, V.; Vast, N. Murnaghan's equation of state for the electronic ground state energy. *Computational materials science* **2006**, *38*, 350–353.
- [44] Katsura, T.; Tange, Y. A simple derivation of the Birch–Murnaghan equations of state (EOSs) and comparison with EOSs derived from other definitions of finite strain. *Minerals* **2019**, *9*, 745.
- [45] Birch, F. Finite elastic strain of cubic crystals. *Physical review* **1947**, *71*, 809.
- [46] VASP-INCAR. <https://www.vasp.at/wiki/index.php/INCAR>, Accessed: 2023-08-12.
- [47] VASP-KPOINTS. <https://www.vasp.at/wiki/index.php/KPOINTS>, Accessed: 2023-08-12.
- [48] VASP-POSCAR. <https://www.vasp.at/wiki/index.php/POSCAR>, Accessed: 2023-08-12.
- [49] VASP-POTCAR. <https://www.vasp.at/wiki/index.php/POTCAR>, Accessed: 2023-08-12.
- [50] VASP-OUTCAR. <https://www.vasp.at/wiki/index.php/OUTCAR>, Accessed: 2023-08-12.
- [51] VASP-CONTCAR. <https://www.vasp.at/wiki/index.php/CONTCAR>, Accessed: 2023-08-12.
- [52] VASP-WAVECAR. <https://www.vasp.at/wiki/index.php/WAVECAR>, Accessed: 2023-08-12.
- [53] VASP-DOSCAR. <https://www.vasp.at/wiki/index.php/DOSCAR>, Accessed: 2023-08-12.
- [54] Hu, Z.; Yang, Y.; Ye, B.; Hu, X.; Chen, L.; Yu, H.; Zhou, Y.; Xie, Z.; Zhou, Z. Enhanced Photoassisted Li-O₂ Battery with Ce-UiO-66 Metal-Organic Framework Based Photocathodes. *Advanced Materials Interfaces* **2023**, 2300074.